UNIVERSITÀ DEGLI STUDI DI PADOVA

Dipartimento di Ingegneria Industriale DII

Corso di Laurea Magistrale in Ingegneria dei Materiali

Effects of Hydrogen and Bifilm Concentrations on the Porosity and Mechanical Properties of an AlSi11(Fe) Foundry Alloy

Relatore: *Ch.mo Prof. Giulio Timelli*
Correlatori: *Prof. Anders Jarfors*
Dr. Qing Zhang
Prof. Murat Tyriakyoglu

Laureando: Ramon Zuccolo

Anno Accademico 2021/2022

Al Duca di Buttrio

ABSTRACT

The aim of this work is to investigate the relationship that exists between the hydrogen content of an aluminum casting alloy and the assessment of melt quality.

Defects, and most importantly porosity, affect the microstructure and the mechanical properties of cast alloys to such a degree that defects analysis, control and prevention has become one of the main fields of research in casting engineering.

Porosity can be divided into gas porosity, correlated to the Hydrogen dissolved into the melt, and shrinkage porosity. It has recently been demonstrated that hydrogen cannot nucleate homogeneously nor heterogeneously into liquid aluminum, a result that forces to abandon old beliefs that attributed the origin of gas porosity into cast aluminum alloys to the nucleation of hydrogen bubbles into the melt during the solidification phase.

This thesis tries to clarify the role of hydrogen in pore formation in reduced pressure test (RPT) samples, the analysis of which is often used to assess the quality of the melt. To do so, six different melts were prepeared, each one characterized by different quality of the raw material, type of damage induced during melt handling, and hydrogen content. RPT samples and tensile test bars were collected and analyzed in order to correlate the melt conditions to the development of porosity under reduced pressure and mechanical properties.

The first chapter of this thesis focuses on the study of the literature, scrutinizing the work of other authors.

The second chapter is dedicated to the discussion of the experiment’s purpose and experimental procedure.

The third and conclusive chapter has the objective of discussing the results of the experiment.

TABLE OF CONTENTS

INTRODUCTION

The quality of cast aluminum alloy components is determined both by the microstructure of the metal and the defects embedded into the metal matrix. As of today, there still does not exist a univocal and complete way to assess the melt quality, mostly because there is no satisfactory way to determine the overall quantity and quality of bifilms floating into the melt.

The role of light alloys in the future of the automotive and aerospace industries is now more obvious than ever, and between all the types of alloys, aluminum alloys are among the most interesting and promising.

The race to the optimization of the mass to mechanical properties ratio, which stands at the very base of the interest towards light alloys, has become an issue of utmost importance for these two industries. As a matter of fact, the great balance between density and strength/elongation that these alloys can provide, has the potential to bring a big advantage in terms of efficiency to both electric vehicles and aircrafts. It is a well-known fact that a main issue with e-vehicles is their considerable weight, an unavoidable outcome for which the heavy Lithium-Ion batteries are mostly accountable for.

Of course, this does not mean that the potential of these metals is limited to the field of electric and hybrid technologies: less weight means increasing the fuel efficiency, reducing fuel consumption and emissions.

Moreover, another important advantage of light alloys over other light and strong materials is that of the good castability, a quality that becomes very useful when the component that must be realized has a complex shape that would otherwise require a lot of machining.

The fact that the largest market for aluminum casting and cast product is the automotive industry, confirms all that has been said above.

When we talk about cast aluminum products, in most of the cases we are referring to Aluminum-Silicon alloys, which offer a good combination of mechanical properties and castability. Alas, as briefly described at the beginning of this introduction, the main issue with Al-Si cast products is that we lack a complete and satisfactory way to assess the melt quality, which results in a considerable variability in the mechanical properties of the cast component, preventing its use in safety-critical applications.

The result of a “dirty” melt is a “porous” cast, and a porous cast will be characterized by unpredictable mechanical properties, corrosion resistance, fatigue resistance and possibly low surface quality.

One of the biggest achievements of the last decades in terms of casting research has been the identification, definition and study of oxide bifilms, a revolutionary discovery that allowed to understand and explain porosity in castings under a new light. This worthy feat would not have been possible without the contribution of Jhon Campbell.

This thesis starts by going through the literature that documents these achievements, and develops by discussing the role that hydrogen gas plays in the formation of porosity in this new scenario by studying its effect on melts of different qualities.

CHAPTER 1

ALUMINUM ALLOYS AND ENTRAINMENT DEFECTS: A REVIEW OF THE LITERATURE

1.1 Aluminum and its Alloys

Aluminum is the most plentiful metallic element on earth [1] and has been an economic competitor for numerous applications in the field of engineering since the end of the 19th century. As an engineering material, it ranks in tonnage use only behind iron and steel, and its growth in production has been continually increasing year by year. For example, bauxite world production (the mineral from which aluminum is extracted) increased from 144 Mt in 2002 to 292 Mt in 2013 [2], more than double the amount in about 10 years.

One of the most striking characteristics of aluminum and its alloys, which contributed to their success in the industry, is their versatility: the range of physical and mechanical properties that can be derived from this pure or alloyed metal is remarkable.

The properties of aluminum that makes it so interesting and attractive are the following:

- *Low Density*: aluminum has a density of only 2.7 g/cm^3, which corresponds approximately to one-third of those of copper (8.93 g/cm^3) and steel (7.83 g/cm^3) [3].
- *Corrosion Resistance*: aluminum possesses a very high corrosion resistance, especially in its pure form (99,8-99,9%), in most environments [4].
- *High Surface Reflectivity*: The fact that polished aluminum can reflect over a wide range of wave lengths leads to its selection for a variety of decorative and functional uses.

- *Electrical Conductivity*: Aluminum finds wide applications thanks to its electrical conductivity, which is almost twice that of copper on an equivalent weight basis. In fact, aluminum´s conductivity is about 61% that of copper, but as already stated above, its density is 3.3 times lower [5,6]. For these reasons, an aluminum conductor has almost half the weight of an equivalent copper conductor. Considering combined factors of cost, conductivity, tensile strength, weight etc., aluminum seems to offer often a better solution for the same problem. Therefore, aluminum is being widely used for overhead conductors [7].
- *Thermal Conductivity*: The thermal conductivity of pure aluminum is about 62% that of copper at 20ºC (239 W/mK vs 386 W/mK) [8], an aspect that combined with its low density becomes advantageous in heat exchangers, evaporators, electrically heated utensils, and automotive cylinder heads [3]
- *Other Characteristics*: Aluminum is nonferromagnetic, nonpyrophoric, nontoxic and easily colored by different techniques.

Whenever solid aluminum is melted in a furnace and then poured into a mold, we talk about cast aluminum products, while whenever the metal is worked in the solid form with the help of specific tools such as mills, rolls and extruders, we talk about wrought aluminum products. What is important to remember, is that these two manufacturing processes produce components with different properties and qualities.

Another difference is that cast aluminum alloys usually contain larger quantities of alloying elements compared to wrought alloys.

For these reasons it seemed natural to divide Al alloys into these two major categories, and the division is clearly seen also in the different nomenclatures adopted for the two categories [9].

1.1.1 Wrought Al alloys

For wrought alloys, a four-digit system is used to divide the different alloys into 9 different families, as seen in Table 1. The first digit (Xxxx) indicates the principal alloying element which has been added to the alloy and is often used to describe the aluminum alloy “series”.

Wrought aluminum is produced by smelting of pure aluminum ingots with specific alloying elements required to make a specific alloy with the desired properties. The melt is then cast into blooms, billets and slabs, that are later processed with one or more of the various manufacturing processes (like flat-rolling, drawing, extrusion, cutting and forging).

The machinability of most aluminum alloys is excellent, even if this is not true for “all” the alloys, and the same goes with formability (specific tensile and yield strengths, ductility and respective rate of work hardening control differences in the amount of permissible deformation) [10].

Moreover, wrought aluminum tends to have better tensile strength when compared to cast alloys, as can be seen by comparing Table 1 with Table 2.

Aluminum alloys also benefit from good weldability and can be joined by means of a wide variety of methods.

GRADE	COMPOSITION	TENSILE STRENGTH* (MPa)	YIELD STRENGTH* (MPa @ 0.2%)
1000 Series	99.00% to 99.99% aluminum	82-166	28 – 152
2000 Series	2.2% to 6.8% copper	186-467	76 – 345
3000 Series	0.3% to 1.5% manganese	110 – 283	41 – 248
4000 Series	3.6% to 13.5% silicon 0.1% to 4.7% copper 0.05% to 1.3% magnesium	172 – 414	45 - 180
5000 Series	0.5% to 5.5% Magnesium	124 – 352	41 - 345
6000 Series	0.2% to 1.8% silicon 0.35% to 1.5% magnesium	124 – 310.3	55.2 – 276
7000 Series	0.8% to 8.2% zinc 0.1% to 3.4% magnesium 0.05% to 2.6% copper	228 – 572	103 - 503
8000 Series	Some Sn and Li in composition	/	/
9000 Series	Reserved for future use	/	/

Table 1: Grading, composition and static properties of wrought Al alloys. *Average values

1.1.2 Cast Al alloys

Casting alloys and pure aluminum are described by a three-digit system followed by a decimal value (Table 2). Again, the first digit indicates the principal alloying element, while the number following the decimal point indicates whether the alloy is a casting (.0) or an ingot (.1 or .2) [11].

As already mentioned, cast aluminum contains larger quantities of alloying elements when compared to wrought products, and generally have lower tensile strength due to the presence of casting defects (the most important of which is porosity). We will have time to understand how cast products could theoretically reach much higher mechanical properties for good melt qualities (i.e., low oxide content).

Due to this concern about the variability and poorness in mechanical properties, cast aluminum products have rarely been used in safety-critical applications.

Aluminum alloy castings are routinely produced by pressure-die, permanent-mold, green-sand, investment, and plaster casting, as well as some variations such as low pressure die casting, centrifugal and lost foam.

The main advantage of cast alloys is that the casting process allows us to obtain products with intricate contours and hollow or cored areas, products that would be far more costly to machine from a part made from a wrought product.

It seems relevant to mention that the automotive industry is the largest single market for aluminum castings, where castings account today for more than 50% of the aluminum used in cars. This aspect, paired with the fact that the total amount of aluminum in an average car has increased from 50 kg in 1990 to today´s 151 kg (and experts estimate that this value will increase to 196 kg by 2025) [12], gives us a good idea on what is the relevance of aluminum in the automotive industry and vice-versa.

A further promising truth is that more than 90% of the metal is recovered after the end of the vehicle´s life, making the use of aluminum in cars a great example of circular economy.

Other advantages of cast aluminum over wrought aluminum are briefly listed below:

- Lower price per kilogram
- Some low ductility alloys are only available as cast products
- Post-machining operations are minimized.

GRADE	COMPOSITION	TENSILE STRENGTH* (MPa)	YIELD STRENGTH* (MPa @ 0.2%)
1xx.x	99.00% to 99.99% aluminum	131-448	28 – 152
2xx.x	4% to 4.6% Copper	131-276	90 – 345
3xx.x	5% to 17% Silicon + Cu or Mg present	117-172	66-172
4xx.x	5% to 12% Silicon	117-172	41-48
5xx.x	5% to 12% Magnesium	131-448	62-152
6xx.x	Not Used	/	/
7xx.x	6.2% to 7.5% Zinc	207-379	117-310
8xx.x	Sn as principal alloying element	/	/
9xx.x	Not Used	/	/

*Table 2: Grading, composition and static properties of cast Al alloys. *Average values*

1.2 Al-Si Cast Alloys

Among the numerous aluminum casting alloys, Aluminum-Silicon cast alloys offer a good combination of mechanical properties and castability, a quality that allowed them to be widely used both in automotive and aerospace applications.

Cast Al alloys can contain Si in amounts from about 5 to 22 weight percent [13]. At this level, Si can provide several benefits:

- Increased fluidity of the melt: this happens because of the high latent heat of solidification of silicon, about 5 times greater than that of pure aluminum [14].
- Reduced contraction associated with solidification.
- Slight reduction in the density of the alloy: the density of silicon is about 87% that of pure aluminum [15].
- Increased ultimate tensile strength: while silicon addition may have some negative effects on elongation due to the lamellar shape of the eutectic, studies

confirm that on the other hand the UTS of the alloy can increase with increased Si content [16].

- Wear resistance: some hypereutectic Al-Si alloys (Si content over 12.6%, see Figure 1) show greater wear resistance due to the presence of primary Si particles [13,17].

Binary phase diagrams are "maps" that show the relationship between composition and phase occurrence as a function of temperature, but under equilibrium conditions. This is a limit of phase diagrams since equilibrium conditions involve very slow heating and cooling rates, while industrial metal production involves faster kinetics (non-equilibrium). Nevertheless, phase diagrams are the starting point in the understanding of an alloy system, and therefore the Al-Si phase diagram (Figure 1) deserves a brief explanation.

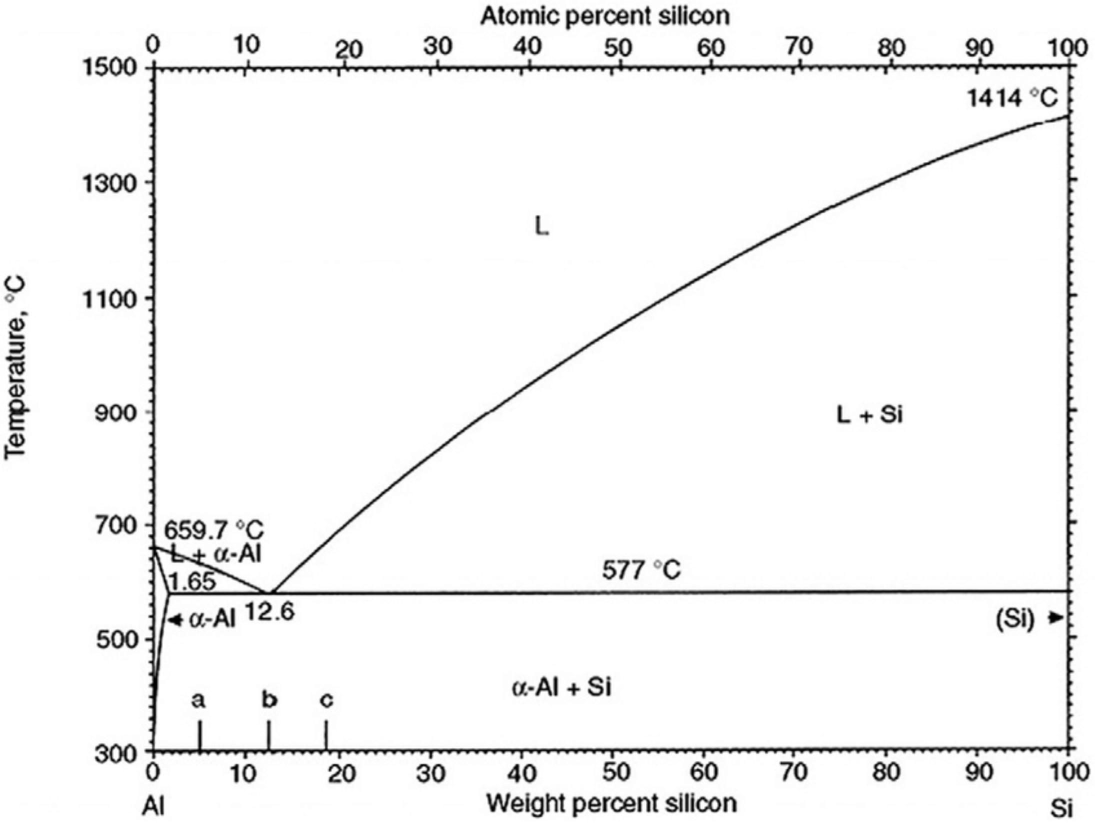

Figure 1: Al-Si phase diagram [18]

The Al-Si phase diagram is a relatively simple binary diagram where there is very little solubility at room temperature for Si in Al and vice-versa. This means that under equilibrium conditions, the terminal solid solutions are nearly pure Al and Si.

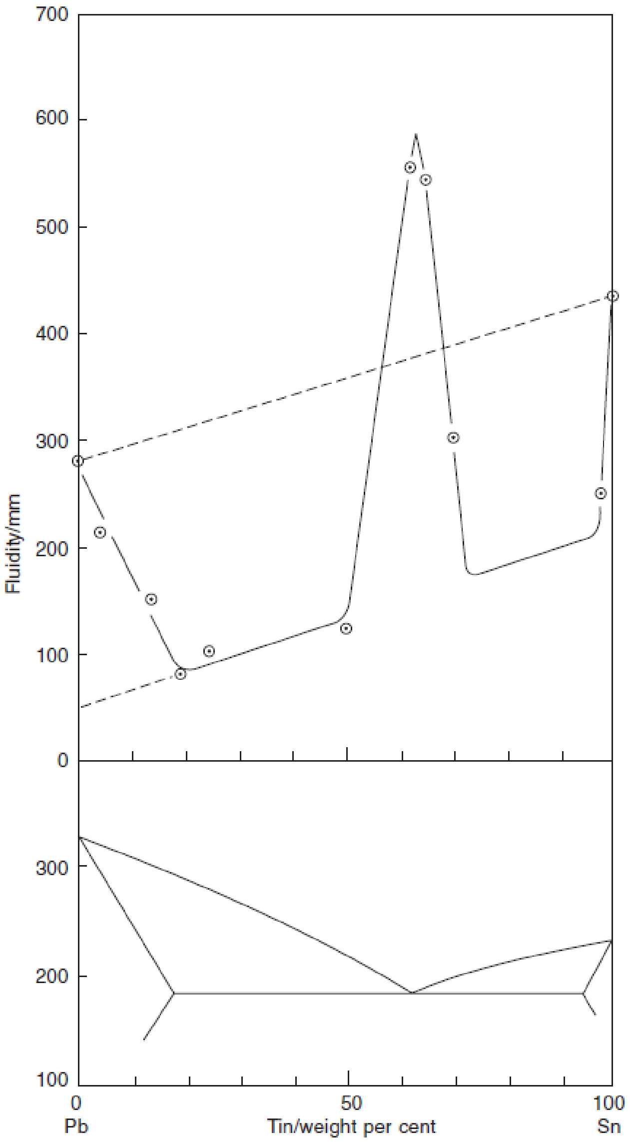

Figure 2: Fluidity of Pb-Sn binary system as a function of the composition. Notice the peaks in fluidity when the elements are in pure form and when the composition is eutectic. [19]

We can see that the maximum solubility of silicon in aluminum occurs at the eutectic temperature (577ºC) and is 1,65 wt. %, while the eutectic composition itself happens at 12,6 wt. %. Near-eutectic Al-Si alloys are popular casting alloys [13] that can be cast by means of different casting techniques, such as sand casting, die casting and permanent mold casting.

It is interesting to highlight that some influential authors such as Campbell [19] had shown some mild criticism about the fact that most of the Al-Si casting alloys contain Si amounts far from the eutectic composition. The main concern is that by staying too far from the eutectic composition, it is impossible to fully benefit from the boost in fluidity that Si can bring to the alloy. This theory emerges from the experimental evidence that in many binary metal systems the fluidity of the pure elements and of the eutectic appears to be superior to that of intermediate compositions (see Figure 2) [19-21].

Note that, in terms of casting alloys, the fluidity is defined as the *maximum* distance to which the metal will flow in a standard mold. Thus, fluidity is simply a length measured in millimeters, inches, or whatever length unit is desired.

1.3 Solidification Defects in Aluminum Alloys

When we talk about solidification defects in cast components, we are generally referring to three main "families" of defects:

1) Shrinkage porosity
2) Gas porosity
3) Hot tearing

During this introduction it will be shown that at least two of these classes of defects could be traced back to the same cause. But before this, it is useful to define in a more specific way the three types of defects.

1.3.1 Shrinkage Porosity

Shrinkage porosity may occur in a casting due to the volume contraction that follows the liquid-to-solid transition.

During the cooling of a liquid metal to the solid state, we will encounter three different types of contraction (see Figure 3):

- Liquid contraction: the atoms of metal in the liquid get closer and closer due to the cooling. This is the normal thermal contraction usually observed in old mercury thermometers. The volume of the liquid metal reduces almost exactly linearly with falling temperature.
- Solidification contraction: this contraction is sudden, so that it happens in a very small temperature range and may be of different magnitude from metal to metal. This happens because of the rapid and drastic crystallization of the atoms from the disordered structure of the liquid to the ordered crystal lattice that characterizes the

solid. In the case of aluminum, the contraction amounts to about 7% of the volume. Note that an addition of 12% of Si can bring down this contraction by 50%, so down to 3.5% [22]! This is greatly due to the fact that silicon is one of the few metals that increase their volume (by 2.9%) at the freezing point [19].

- Solid contraction: the metal, now solid, shrinks linearly and slowly with a further decrease in temperature.

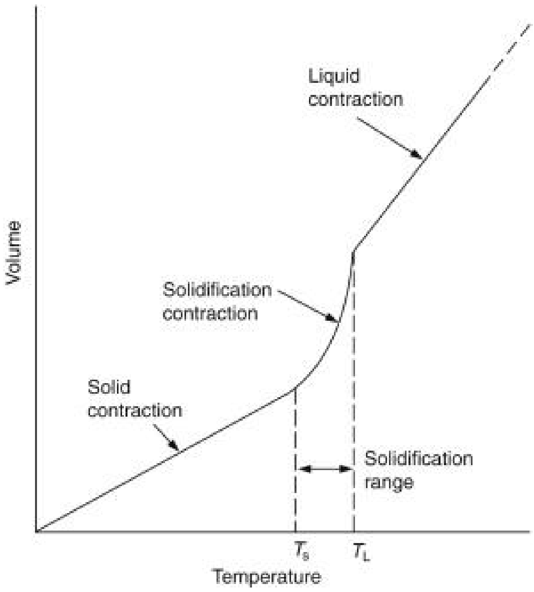

Figure 3: Volume contraction of metal as a function of temperature [19]

Shrinkage porosity can manifest itself in various forms, which range from macroporosity down to microporosity (intra-dendritic and micron-sized) and is greatly favored when the solidification process begins on the whole surface of the piece, as usually happens in cast components.

The solutions to shrinkage porosity come in different forms. One has already been suggested and consists in using alloying elements such as silicon in order to balance the volumetric contraction, while other approaches consist in the careful engineering of the mold, in order to avoid excessively thin sections, introduce chillers near troubling sections of the casting and add risers in order to store liquid metal that can be provided during the solidification process.

Moreover, small secondary dendrite arm spacing (SDAS) and short primary dendritic trunks (achievable by increasing the cooling rate and by inoculating the material respectively) are great ways to help reduce microporosity [22].

1.3.2 Gas Porosity

The gas pores are generally spherical and show a very shiny inner surface

A multitude of metals can dissolve great amounts of gas in the liquid state. In the case of molten aluminum, the only gas that is known to be soluble in it is Hydrogen [19,23,24]. Hydrogen adsorption into liquid aluminum is due to the decomposition of moisture in air as well as the oxidation of aluminum itself:

$$2H_2O \rightarrow 2H_2 + O_2 \tag{1.1}$$

$$3H_2O + 2Al \rightarrow Al_2O_3 + 3H_2 \tag{1.2}$$

This diatomic hydrogen gets then dissolved in aluminum as:

$$H_2 \rightarrow 2[H] \tag{1.3}$$

Anyways, as can be seen in Figure 4, the solubility of hydrogen in aluminum abruptly drops by a factor of about 22 when solidification occurs (from 24.0 appm at 660ºC before freezing to around 1.1 appm after solidification, where appm stands for "atomic parts per million").

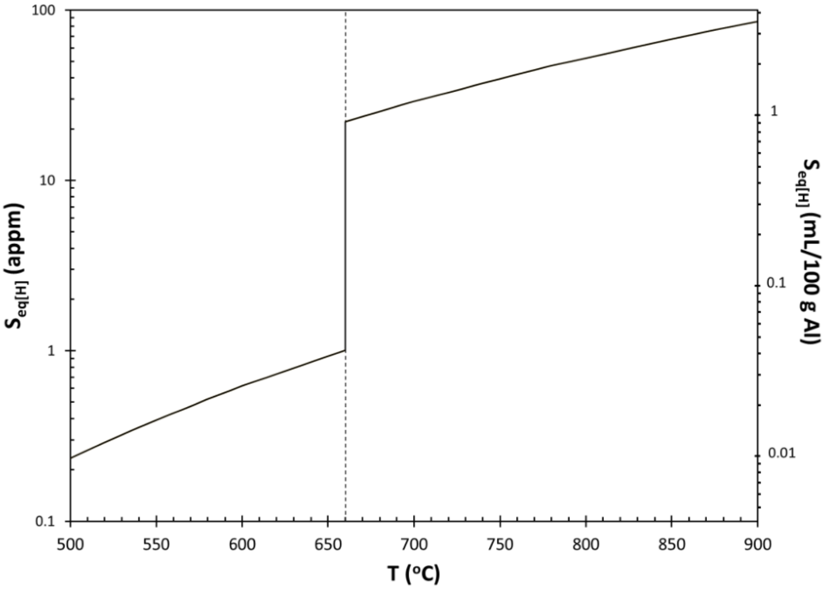

Figure 4: The equilibrium solubility of hydrogen in liquid and solid aluminum as a function of temperature [23]

This abrupt decrease in solubility has led to the speculation that hydrogen, expelled from the solidification front, accumulates in the liquid phase and continuously enriches the layer ahead of the advancing front in a snow-plough effect. At some point the concentration would be so high to reach the supersaturation of gas in the liquid and finally generate the gas porosity.

However, as straight forward as this explanation seems, the truth has been shown to be very different. It has been indeed recognized that hydrogen pores cannot nucleate neither homogeneously [19,25] nor heterogeneously [23] inside liquid aluminum, so that the previous theories surrounding gas porosity now seem to be wrong.

A new explanation for gas porosity in aluminum castings is therefore required and, as we will see, could probably be found by looking at the subject form the perspective of entrainment defects.

1.3.3 Hot Tearing

Hot tearing is the undesired formation of irregular cracks in metal castings that develop during solidification and cooling; typically, while the casting is still inside the mold or die cavity [26]. The driving forces behind hot tearing are the thermal induced stresses and strains developed during solidification on the surface of the casting, so that hot tearing often occurs at the inside corners or fillets of casting geometries, where casting shrinkage is restrained by the rigid mold cavity. In particular, in permanent mold castings the mold is generally made of steel, a metal that is characterized by higher rigidity than the aluminum that is cast inside.

Hot tears usually present some characteristic properties that could be listed as follows:

- Occur as messy and branched cracks.
- Main tearing and its extensions observed to be intergranular.
- Defect surface has a dendritic morphology.
- Defect surface is usually packed with heavy oxides.
- Generally located on hot spots where shrinkage deformation takes place.
- Not always seen under the same conditions.
- Specific to certain alloys; not seen in all alloys.

Main reasons that cause hot tearing are contraction in mushy zone, restricted shrinkage and lack of feeding [27].

1.4 Entrainment and Bifilms

In this section the most important concept of the thesis will be introduced, starting from the definition of *bifilm* and of entrainment process. To the definition of bifilm will follow a general review of several case studies published during the last decades that address these kinds of defects and show how they are strictly correlated to mechanical properties and overall quality of the casting.

1.4.1 The Entrainment Process

When common liquids, like water for example, are poured or are subject to a breaking wave, their surface is subjected to a certain degree of turbulence that may result in buckling and splashing. When the breaking wave or the droplets fall back into the bulk of the liquid, the two surfaces get mutually assimilated, and the liquid can reversibly go back to the starting condition.

However, this intuitive example does not apply to many other common liquids the surface of which is not a liquid, but a solid, even if it is an invisible film of extreme thinness. Most liquid metals belong in this category since their surface gets covered in a thin oxide film because of air exposure. For aluminum, this amorphous oxide film has a high impermeability to the diffusion of aluminum and oxygen ions, thus, the film cannot thicken rapidly, forming a protective layer over the molten metal.

In case a solid layer floats on the liquid, during turbulent flow the surface film could fold on itself and be submerged into the liquid, becoming entrained (Figure 5). This is also true for splashes of droplets that fall back into the melt.

This phenomenon gives an easy and immediate solution to an otherwise apparent paradox: the presence of oxide inclusions inside metals that have practically zero

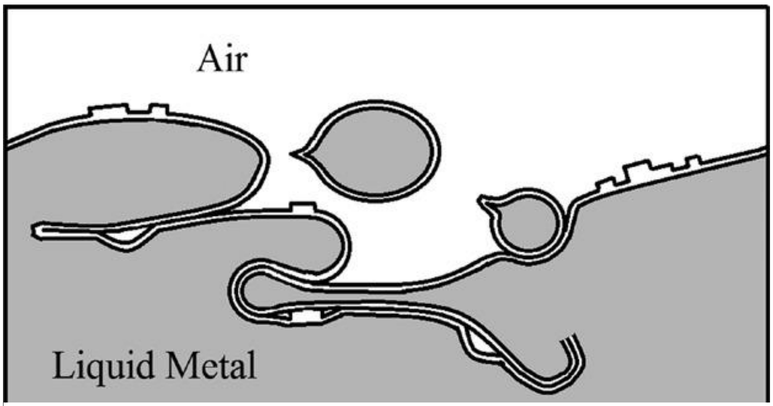

Figure 5: the entrainment process due to surface turbulence in liquid metal [29]

solubility for oxygen. For example, according to thermodynamic considerations, not a single atom of oxygen should dissolve in liquid aluminum [28].

Usually, the entrainment process is very fast and happens in a matter of milliseconds, so that the creation of new surface, and the time for the formation of new oxide film is so limited that the submerged film´s thickness could be of just a few nanometers.

Because of the high tendency of aluminum to oxidize [30] (as can be seen in the Ellingham diagram in Figure 6) whenever the surface film is broken or entrained, a new film is formed in such a brief time that the process can be considered instantaneous.

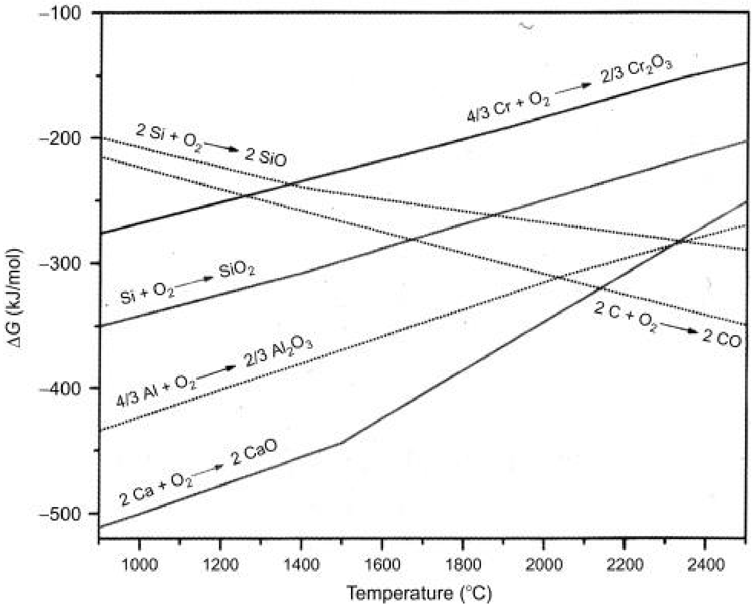

Figure 6: Ellingham diagram [31]

The oxide grows on the surface of the metal atom by atom, as each of the metal atoms encounters the surrounding gas. For this reason, the underside of the film will always be in perfect atomic contact with the melt, resting on it with a perfect fit.

The first thin layer of oxide is amorphous and forms in very short times, but as this layer reaches a certain thickness, it assumes a crystalline structure [32]. The crystalline structure and the composition of the oxide film strictly depends on the composition of the melt. For example, for commercially pure aluminum the oxide is expected to be composed of pure alumina, with structures that range from γ-Al_2O_3 platelets to α-Al_2O_3 particles [32], while for aluminum alloys containing different quantities of magnesium the oxides that form will include spinel ($MgAl_xO_y$) and magnesia (MgO) (see §1.6.1).

Entrainment defects are cumulative: aluminum surface oxides are marginally denser than the molten metal, but the entrained air in the bifilm means that many defects have near neutral buoyancy [28]. This means that the bifilms continue to float into the melt regardless of the holding time. Moreover, due to the dry nature of the oxide, whenever a bifilm gets entrained, the two surfaces will be unable to form any physical or chemical bonding, leaving a crack-like defect floating around in the melt.

As much as this is true, there is another aspect to consider. The same entrained air that makes them almost buoyancy-neutral could react with fresh metal to form oxides and nitrides. Some studies already investigated this possibility [33-35] and concluded that the oxygen and nitrogen of an air bubble trapped into commercially pure molten aluminum can be consumed by reaction with the surrounding metal to form Al_2O_3 and AlN (only once the oxygen was almost completely depleted). As proof of what previously stated, the oxide produced depends on the composition of the melt, but the only nitride ever observed to form was AlN. The fresh metal inside the bifilm was assumed to be provided by the cracks generated during the transition of the oxide from amorphous to α or γ type alumina, but the latest experiments [33,34] suggested that the cracks were rather formed during the movement of the oxide inside the melt.

These studies ultimately suggested that, theoretically, the internal atmosphere of a double oxide film defect should be consumed in a matter of seconds. The reason why this does not actually happen can be found in the diffusion of hydrogen into the cavity.

1.4.2 Furling and Unfurling

During the entrainment phase, the furling of the entrained bifilm into a compact mass is much probable. This would happen because if the energy provided to the melt is sufficient to create an entrainment event, then the internal turbulence beneath the surface would also experience bulk turbulence (i.e., $Re > 2000$, where Re is the Reynolds number). Considering that bifilms are generally thin, they do not have sufficient rigidity to resist this turbulence and are easily wrapped and furled by the turbulent eddies. In this convoluted form. a large bifilm, of the order of several millimeters, may be able to pass through a relatively fine filter [28], making such filter only partially effective. Moreover, while in this "furled-form" the effect of the bifilm on the final mechanical properties of the cast component are expected to be minimal, so that even a relatively "dirty" melt would yield a decent cast in the end. The problem arises once the pouring phase of a transfer is finished, or the casting operation is completed, at which point the internal turbulence ceases and the melt rests quiescently. In this static condition, the unfurling of the oxides may occur because of various influences and effects such as:

- The precipitation of hydrogen into the bifilm (see §1.4.3) (Figure 7).
- The local pressure drop caused by solidification shrinkage. The result is in fact remarkably similar to the hydrogen inflation, but if the opening effect takes place at a late stage of freezing the defect would attempt to open when surrounded by dendrites [19] (see §1.4.4) (Figure 7).
- The straightening effect of intermetallics. Bifilms (the varieties observed so far) are favored sites for the nucleation and growth of a wide number of intermetallics from the wetted side of the film [19,28,36]. A good example are the β-Fe particles (Al_5FeSi): when they first nucleate, the β-Fe crystals are only some nanometers thick, so that they can follow the curvature of the crumpled bifilm. However, as the crystals grow in thickness, they also increase their stiffness and so continuing their growth they exert a straightening effect on the bifilm.

  The straightening effect of growing dendrites. As the dendrites grow, they may have an unravelling effect on the bifilms, since they cannot grow “through” them. (Figure 7).

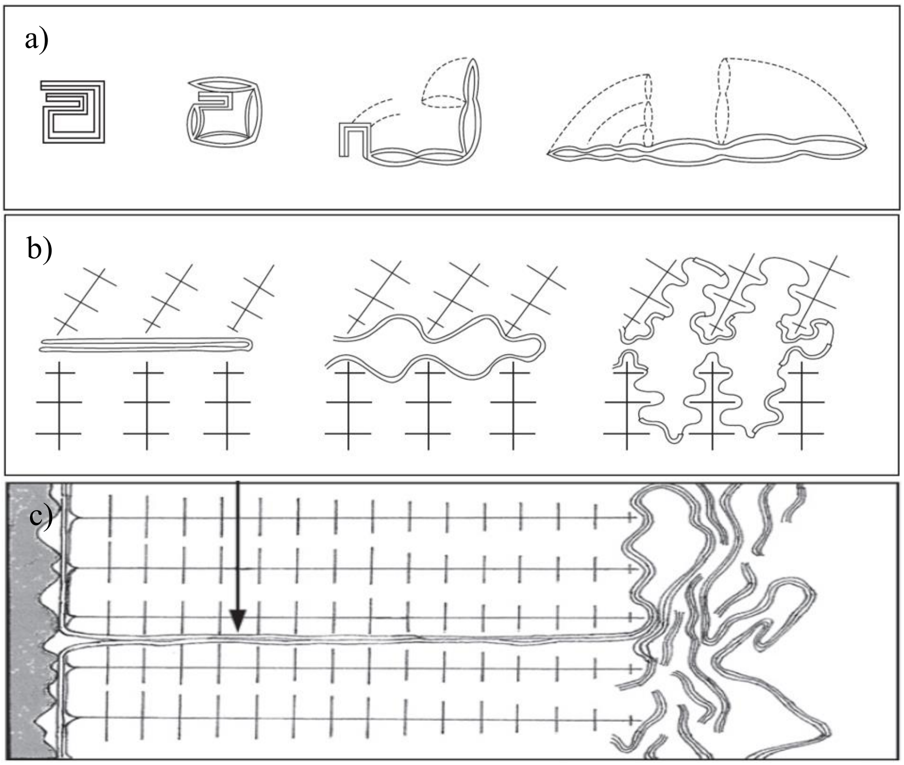

Figure 7: a) Unravelling by gas porosity, b) Unravelling by shrinkage pressure drop, c) Unravelling by dendrite straightening [19]

Whatever the driving force behind unfurling is, the common variable remains time: the unfurling process requires time, so that if the freezing of the casting is fast enough the bifilms may remain trapped between grains in a convoluted form, minimizing the degradation of mechanical properties. But if the freezing time gets longer the bifilm will have time to unfurl and assume its crack-like shape, resulting in a serious impairment of the mechanical integrity of the component.

1.4.3 Bifilms and Gas Porosity

Hydrogen cannot nucleate heterogeneously nor homogeneously into molten aluminum. Moreover, it has been demonstrated that the equilibrium vacancy concentration in aluminum at the melting temperature is sufficient to accommodate the excess hydrogen [37]. For these reasons, the so called "gas porosity" must be explained considering this new scientific evidence, and the presence of bifilms floating inside the melt can provide this new explanation.

The un-bonded dry surfaces of the oxide bifilm allow to drastically reduce the energy needed for the hydrogen bubble precipitation by removing the surface energy required. In other words, the bifilms act as pockets in which hydrogen can diffuse with little to no effort. As proof of this statement, Dispinar and Campbell showed that no hydrogen pores were formed in the reduced pressure test (see §1.5.3) samples taken from a very clean aluminum melt, even for levels of hydrogen in the melt as high as 0.4 mL / 100g of melt [84]. Moreover, Raiszadeh and Griffiths showed that when the concentration of dissolved hydrogen in the melt was higher than that in the equilibrium with the surrounding atmosphere, hydrogen could diffuse into the trapped atmosphere of an oxide film defect and expand it [33].

As hinted in the previous paragraph, hydrogen plays a role in the unravelling of bifilms by precipitating inside the cavity and inflating it like a balloon. If the bifilm is small enough and the hydrogen content of the melt is high enough, the bifilm could inflate so much that the porosity assumes a spherical shape. In some instances, the bifilm could inflate so much that the final bubble´s surface exceeds the initial bifilm surface even by a big amount. But as detrimental as the interaction between oxides and hydrogen may seem for the melt, it is interesting to highlight the protective effect that the surface oxide layer provides against hydrogen in the first place. Griffiths et al. [34] reported that when the surface oxide film on the melt was disturbed or removed, the rates of adsorption of hydrogen from the surrounding atmosphere were 10000 times higher than when the film was left undisturbed. This is clear evidence that the presence of an unbroken surface oxide film significantly reduces the flow of gas in and out of the metal.

1.4.4 Bifilms and Shrinkage Porosity

Shrinkage porosity is considered to be the result of a poor feeding of the casting combined with the volumetric shrinkage that comes with the solidification of the melt (see §1.3.2). In this sense, Campbell underlines that this kind of porosity should certainly be removed using an adequate gating and feeding system, provided with feeders and chillers around the hot spots [19]. Yet, in some well-engineered castings shrinkage porosity still appears to be an issue.

A possible explanation to this condition could again be found considering what we know about bifilms. The un-bonded dry surfaces of the bifilm may provide a similar advantage to that discussed in the previous paragraph, reducing the energy needed for shrinkage porosity to happen. The drop in pressure caused by the volumetric shrinkage may act as the driving force that “sucks” the bifilm open, creating the porosity. If this happens at an early stage of solidification, the shape of the pore may be spherical (much like that associated with gas porosity), but if happens at a later stage of solidification, then the final shape would be more complex and convoluted, and the surface constellated by dendrites (see Figure 7). This latter would be virtually indistinguishable from conventional shrinkage porosity.

Then how could we tell if what we observe in the final casting is shrinkage porosity or bifilm-related porosity? Campbell answers this question with an emblematic sentence: "it *appears* to be shrinkage, but most likely *not* shrinkage" [19,38].

Anyway, it is important to remember that other authors may disagree with this saying, reiterating that most of what "*appears*" to be shrinkage actually "*is*" shrinkage porosity. What seems to be undeniably true is that bifilms can explain at least a portion of this kind of porosity.

1.4.5 Bifilms and Hot Tears

As previously stated, the driving forces behind hot tearing are the thermal induced stresses and strains developed during solidification on the surface of the component. For this reason, it may appear that no correlation exists between bifilms and hot tearing. Nevertheless, a study conducted by Uludag et al. [27] found an interesting result: in the experiment, the sensibility of three different aluminum melts (A356, A380, A413) to hot tearing was to be assessed, so that every melt was cast in CRC and T shaped molds both before and after degassing treatment. The degassed melt was considered as mostly "clean" from bifilms. The results of the experiments showed that hot tearing occurred only in "clean" melt castings.

When the castings from the "dirty" melt were cut, it was found that there were more than 20 pores on the T junction of the sample. The logical conclusion was that a higher number of bifilms allowed for a greater amount of porosity (as confirmed by the bifilm index evaluation), thus, such porosity had compensated the negative effect of thermal stresses. On the other hand, hot tearing could be observed in most of the "clean" castings.

In conclusion, this study seems to show that for hot tear to occur, there must be very few numbers of bifilms in the melt. Moreover, these bifilms should end up at the hot spot and their orientation should align with the stress and strain rate generated by the hot spot for hot tearing to occur. These conclusions are in apparent contradiction with previous claims by Campbell [39], according to which hot tearing could not happen if the melt were clean from bifilms. He supports such claims in light of his and other studies’ findings [40,41] in which turbulence (the easiest way to entrain bifilms) was always associated with hot tearing, while quiescent and laminar flow yielded hot-tear-free castings. The explanation to this relationship was that bifilms function as a sort of nucleation site for hot tears, allowing the initiation of the stress-relieving cracks.

An explanation to this contradiction may lay in the fact that even the “clean” melts mentioned in Uludag´s work were not free from bifilms, they just had fewer of them (as demonstrated by their bifilm indexes).

In any case, the relationship between oxide films and hot tearing in aluminum castings is complex and depends on many factors, such as orientation, state (furled or unfurled), size, number, and position of the oxides, so that no easy answer may exists.

1.4.6 Bifilms and Fluidity

Fluidity as intended in the casting industry must not be confused with the physical property defined as the reciprocal of viscosity [42]. Here, fluidity is instead a complex characteristic related to the alloy´s behavior under specific conditions within a foundry mold [43]. The difference between fluidity as a physical property and fluidity in casting alloys is because failure to fill a mold in a casting process is hardly a matter of viscosity (as viscosity of molten metals is generally very low [43,44]) and easily a matter of premature solidification.

For casting alloys, fluidity is defined as the maximum distance to which the metal will flow in a standard mold before it is stopped by solidification [19] and is therefore a length (measured using length units, such as millimeters). To measure this length several types of tests exist, such as the spiral test and the vacuum fluidity test, each one with its advantages and disadvantages. Anyway, it was demonstrated by Campbell that despite their differences, if the mold material is kept the same, these tests can give consistent and equivalent results (if surface tension and casting geometry are considered) [39].

Among the different variables affecting fluidity [45] it has been shown that oxide inclusions are an important parameter. Melts with scrap additions (i.e., with higher oxide content) show lower fluidity than their purer counterparts [43], probably because the increasing number of bifilms hinders the melt flow, contributing to the amount of solid fraction needed to completely stop the flow, a parameter also known as *critical solid fraction* (f_{crit}). Therefore, bifilms reduce the value of f_{crit}, which is characteristic to worse fluidity melts.

In conclusion, oxide bifilms reduce fluidity [46].

1.4.7 Bifilms and Microstructure

Bifilms can also influence the microstructure of the casting in terms of grain size, secondary dendrite arm spacing (SDAS) and on the modification of Al-Si alloys by Na and Sr addition [47].

1.4.7.1 Control of Grain Size

As previously discussed, bifilms can be straightened and unfurled by the growth of dendrites. In this flat form, the bifilm acts as a sort of barrier through the casting section that can prevent convection, leading to the suppression of thermal or mechanical perturbations and, finally, to coarse grains.

In different sections of a same casting in which turbulence is known to be lower, it is possible to observe a finer microstructure and more ductile behavior at fracture [48].

Moreover, a potential inoculating effect of the bifilms has been investigated by Wang et al. [32], according to whom at least in terms of lattice misfit at the interface, oxides such as alumina (γ and α) and spinel are as potent as the commonly used grain refiner TiB_2. This inoculation is achievable by intensive melt shearing prior to solidification, an operation that leads to the dispersion of oxide particles from the bifilms in a sufficient number to act as heterogeneous nucleation points for the aluminum dendrites.

In this regard, let us briefly address the reason aluminum alloys should benefit from grain refinement: as the grain size d of a metal is reduced, its yield strength increases according to the formula proposed by Hall and Petch [49]:

$$\sigma_y = a + bd^{-\frac{1}{2}} \tag{1.4}$$

Where a and b are constants. The basic assumption behind this equation is that slip planes can operate with low resistance across a grain, allowing the two halves of the grain to shift and concentrating stress on the point where the slip plane impinges on the next grain. For this reason, the higher the number of grains, the higher the resistance to slipping. The mechanism is similar to the spreading of a crack that halts at each grain boundary.

This behavior can be observed in hexagonal close-packed latices, where there are few slip systems, so that slip is not easily activated in a randomly oriented neighbor. Unfortunately, it contrasts with the behavior of face-centered-cubic materials such as aluminum: because FCC lattices offer numerous slip systems, there will always be a slip system close to a favorable slip orientation in a neighboring grain [39]. For this reason, some aluminum alloys do not reveal the expected linear increase in yield strength with the square root of d [50-54]. On the other hand, other studies seem to confirm a correlation between the improvement of mechanical properties and the reduction of grain size [55,56]. This contradiction between conclusions may be related to different solidification history of the alloy [54], but what emerges from the literature is that, as of now, it is not possible to state with confidence that grain refinement in aluminum alloys improves their mechanical properties according to the Hall-Petch equation.

1.4.7.2 Control of Dendrite Arm Spacing

Contrary to the uncertainty surrounding the possible benefits of grain size on mechanical properties, there seems to be much more confidence around the benefits of a reduced SDAS. Reducing the SDAS improves both strength and toughness of the alloy [39,54,57], and is achieved whenever the cooling rate is high.

As similar as the reduction of SDAS appears to be to grain refinement, Campbell negates any correlation between their mechanism of action [39] because no grain boundary exists between the arms of a single dendrite to stop the slide of a slip plane. Since a single dendrite is distinguished by the same crystal lattice, a dislocation would be able to run across arm after arm of the dendrite without hindrance. Moreover, Hall-Petch strengthening should only affect the yield strength of the material but, in the literature, it is often found that reduced SDAS affects more the ultimate tensile strength and the elongation at fracture of the alloy rather than the actual yield strength [54,57,58]. This suggests that a different explanation for reduced-SDAS strengthening is needed.

A first explanation, that does not address the influence of oxide inclusions, comes from the work conducted by Ghassemali et al. [54], in which the improvement in mechanical properties correlated with reduced SDAS is linked to the finer grain size and the direction of slip planes inside single dendrite. SEM and IPF micrographs of the microstructure showed that, during plastic deformation, most of slip bands appeared inside the dendrite and each grain activated an identical slip system (Figure 8).

Finer grains lead to more dendrites, and therefore variety of active slip systems, which improves the strength of the alloy.

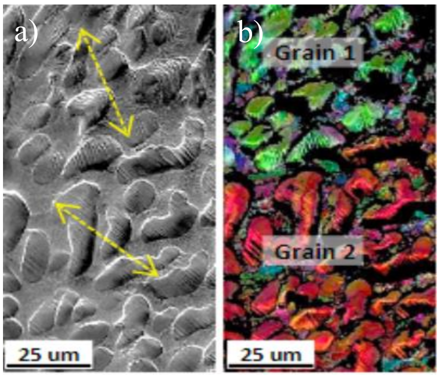

Figure 8: a) SEM micrograph and b) IBF map of two grains of an Al-Si-Sr casting. The yellow arrows show the slip band´s direction in each grain. [54]

This explanation considers again the grain size but explains its effect on the mechanical response in a different way from Hall and Petch.

A second answer is provided by Campbell, whom after having considered all the possible ways in which SDAS can benefit or degrade the mechanical properties, advances the conclusion that none of those could explain in full the actual improvements/worsening of mechanical properties observed in actual castings [39]. The main actors responsible for the variation in properties would be, in his opinion, just bifilms. As previously hinted, SDAS is a function of the freezing time: long freezing times lead to big SDAS, while short freezing times lead to small SDAS. At the same time, as seen in §1.4.2, long freezing times allow the unfurling of bifilms, while fast freezing results in convoluted and furled oxides. If there is little time, the defects will be frozen into the casting in a compact form, reducing their negative impact on mechanical properties. Following this logic, Campbell states that even if the fall of ductility with increasing dendrite arm spacing (DAS) becomes clear, it is not the DAS itself that is important. The DAS is "*merely the indicator of the time available for the opening of bifilms*", and it is the opening of the bifilms into planar crack that really affects the integrity of the casting. So, big SDAS *indicates* long freezing time and therefore unfurled oxides, while small SDAS *indicates* short freezing time and therefore furled oxides. This theory would be somewhat supported by the fact that, with the introduction of the Nemak Cosworth process, characterized by quiescent transfer and counter-gravity filling and lower overall oxide entrainment, the mechanical properties of the castings greatly improved. Interestingly, micrographs of the microstructure revealed no change in the SDAS with respect to the previous casting process.

Another persuasive proof of Campbell´s theory comes from a paper by Tiryakioglu et al. [59], in which a collection of mechanical data from the aerospace casting industry was plotted to extrapolate the maximum ductility curve. The castings that belong to this curve show the optimized compromise between strength and ductility, so one would expect their microstructure to be characterized by small SDAS. On the contrary, their SDAS range between 13 and 45 µm, a remarkably wide range.

Finally, it seems necessary to explain a possible way in which bifilms can actively influence the SDAS of a casting. Bifilms, when unfurled, can act as massive and effective barriers that separate regions of the casting. This barrier-action can be so efficient that if no nucleation site is present in one of the isolated regions, then solidification will not occur, despite freezing taking place in an immediately adjacent region of the casting [47]. In this case, the un-frozen region will solidify only when a sufficiently low level of undercooling is reached (even hundreds of degrees), at which point freezing would be extremely fast, giving a fine microstructure with small SDAS. In Figure 9 an oxide bifilm is seen in the middle of the micrography. On the right side the melt solidified in normal time, giving a coarse microstructure, while on the left side freezing happened only at a later stage, when sufficient undercooling was reached. This resulted in a much finer microstructure.

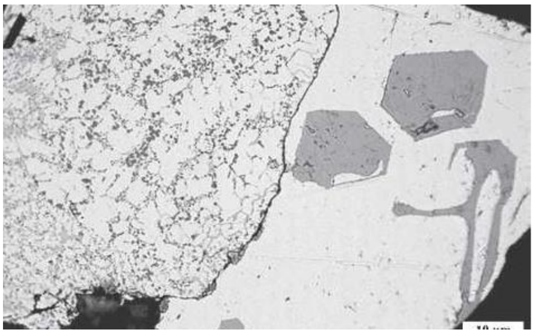

Figure 9: Regions of Al alloy separated by a bifilm show different microstructure [47]

1.4.7.3 Control of Modification of the Al-Si Eutectic

An unmodified alloy is characterized by large flakes of brittle silicon, whose morphology greatly impairs ductility. These unmodified alloys often present brittle fracture surfaces and elongations of just a few percent, because the load bearing primary Si phase assumes this shape. To both minimize excessive machine tool wear and meet the “ultra-strict wear regime”, the Si phase must be present as fine, well dispersed particles [60]. This can be achieved with a successful modification treatment, as can be clearly seen in Figure 10.

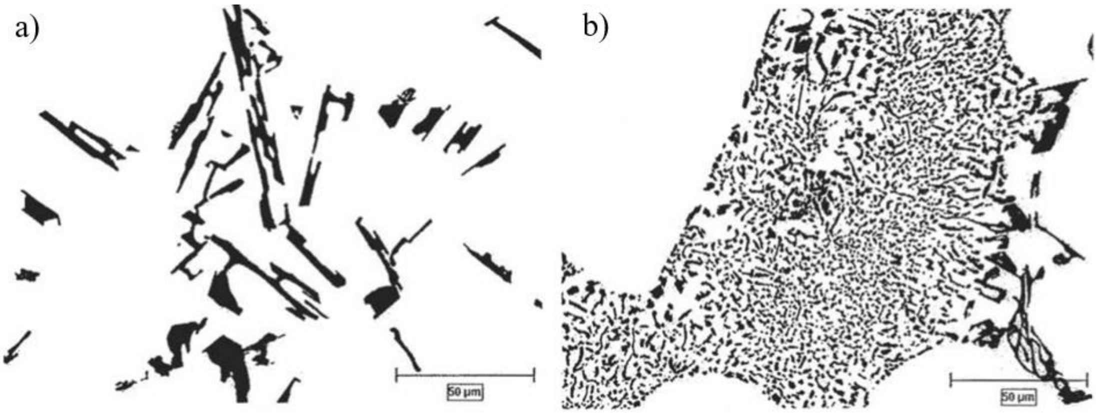

Figure 10: a) Unmodified vs b) Modified silicon structure in A356 aluminum alloy. Note the difference in the average size of silicon particles and eutectic grain [61]

Modification treatment usually consists in the addition to the melt of strontium, sodium or, in some cases, calcium [61]. Due to the low solubility of Na in molten aluminum and its high vapor pressure, and due to the increased gas pickup sensibility of the melt that follows Ca addition, to this day the most used eutectic modifier is Sr.

Modification of Al-Si eutectic is a complex and controversial subject and many conflicting theories have been proposed to explain the mechanism behind it. One of these theories considers bifilms as main actors in the nucleation and modification of the eutectic [36,62,63], claiming that at low concentrations of P (AlP nucleates Si in particulate morphology [64]) and in the absence of Sr the bifilms act as nucleating sites for Si in platelike form. Si precipitates onto the oxides and straightens them due to its planar growth, creating long cracks in association with the primary Si particles and degrading mechanical properties. This could explain the high number of cracks often observed in eutectic Si particles, that would otherwise be hard to explain: the Si particles may be pre-cracked by the presence of the oxide in the middle [65].

When Sr is introduced, it deactivates both AlP and bifilms as favored growth sites in favor of a "*coral-like*" growth of the eutectic. At this point bifilms are no longer sequestered for Si nucleation and are available for blocking interdendritic and intergranular flow. This, along with the increased reactivity of the melt resulting from the Sr addition [66], can lead to an overall increase in porosity with respect to an unmodified melt, as already observed by Uludag et al. [67,68].

This theory seems even more interesting when casting plants such as the Nemak Windsor facility, which adopt the Cosworth process mentioned before, do not need to modify their melts with Sr because it would lead to worse mechanical properties. If there are little to no bifilms and no P in the melt, the only way Si could nucleate would be through the "coral-like" morphology.

The biggest critique to this theory was advanced by Sigworth [69], who claimed that the enormous number of bifilms needed in the melt to nucleate all the eutectic grains observed in common castings (around 10^{12}-10^{16} per kg of melt according to Campbell) cannot be achieved by normal means and would be an unrealistic assumption.

1.5 Ways to Assess Melt Quality

As it has been shown in the previous paragraphs of this first chapter, the most deleterious defect of aluminum castings are oxides, since they directly influence porosity and fluidity, and could potentially influence hot tears and microstructure.

At the same time, the influence of oxides on the mechanical properties and final quality of the melt is somewhat correlated to the hydrogen content. If the hydrogen level in the melt was hypothetically zero, during solidification the bifilms could only open due to the pressure drop correlated with volume shrinkage.

In an opposite example, we could consider an exceptionally clean melt, without bifilms, with a high hydrogen content. In this condition, as explained in §1.3.2, no gas porosity would be able to nucleate, and the only source of porosity would again be shrinkage.

So, hydrogen and oxides are two different parameters that often concur in the same problem. Therefore, a good indicator of melt quality would be to measure both hydrogen and oxide content of the melt to evaluate the potential damage from their interaction.

As of today, instruments that can precisely assess the hydrogen content of the melt exist (like for example the HYCAL^{TM}, Alcan^{TM} and Hyscan^{TM} devices), but there is no easy-to-use and reliable method to measure the oxide content. Moreover, often the methods used in the industry provide results that are not easy to interpret [70].

It is important to have a way to measure *exclusively* the oxide content of the melt because, as it will be clearer later, removing the porosity by removing the hydrogen (or closing it by means of squeeze casting or hot isostatic pressing) does not necessarily increase the quality of the final casting. Even with low porosity, if the bifilm content is high, the ductility of the cast component will be far from the maximum ductility potential estimated in [59,71].

In this paragraph, a series of test methods developed for inclusion detection in molten aluminum are analyzed and discussed, along with their advantages and disadvantages.

1.5.1 Liquid Metal Cleanliness Analyzer (LiMCA)

The liquid metal cleanliness analyzer (LiMCA) is used for fast in-situ detection of inclusions in liquid metals and is based on the Coulter Counter principle [72]. Note that the term "inclusions" is not limited to oxide bifilms, but rather encompasses every kind of inclusion present in the melt. The apparatus, used in *running* systems, is shown in Figure 11 and consists in a probe head and the measuring/powering unit. The probe consists of an electrically insulating sampling tube and two electrodes connected to a battery with and electromotive force E, driving current through a small orifice in the

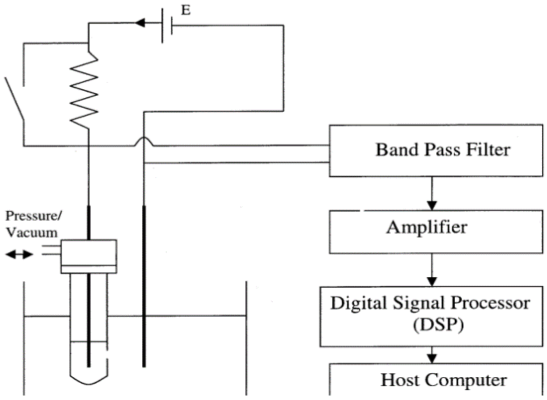

Figure 11: Schematic configuration of a LiMCA apparatus [72]

tube [73]. When suspended inclusions pass through this orifice, the electrical resistance across it increases in direct proportion to the volume of the particle.
When this technique is used to monitor actual particles such as borides and carbides, the results are unambiguous and valuable [70,74]. Nevertheless, when LiMCA is used with the intention of measuring the bifilm content, the main problems are two:

- The technique is limited to inclusions that can enter the hole.
- Oxide inclusions do not come in form of particles, but rather in form of films.

Since bifilms can often be longer than a few centimeters [19,39] and the diameter of the orifice of the tube is around 0.05 to 0.1 mm, the problem in the detection of bifilms via the LiCMA is evident. Moreover, inclusion measurements via LiMCA could be complicated by the fact that there are high concentrations of micro-bubbles after the degassing station, if degassing is used [75].

1.5.2 Porous Disk Filtration Analysis (PoDFA) and Pressurized Filtration Analysis (PREFIL)

Porous disk filtration analysis (PoDFA) and pressurized filtration analysis (PREFIL) both work with the same principle, with the only difference that the PoDFA operates by de-pressurizing the chamber where the melt is , while the PREFIL pressurizes the melt, forcing it to flow through a filter of known mesh size (see Figure 12). Two types of information can be collected by this test:

- The comparison of the filtrate mass vs filtration time graph, which can give an insight on the cleanness of the melt [76].
- The metallographic analysis of the filter, which can show the types of inclusions present in the melt. This is possible because the process concentrates the inclusions in the filter by 5000 to 10000 times [76,77].

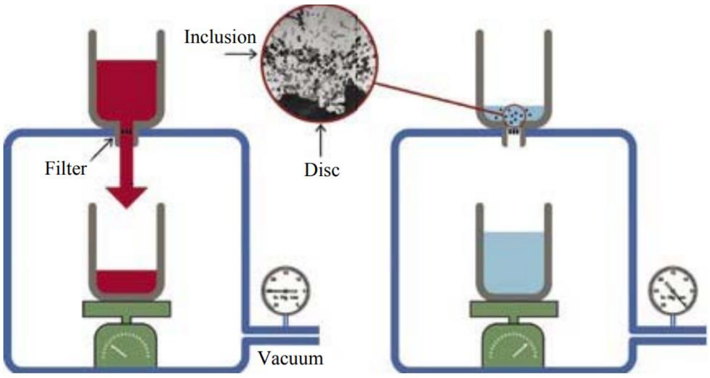

Figure 12: Schematization of a PoDFA and PREFIL apparatuses. The PoDFA applies a vacuum to the chamber, while the PREFIL increases its pressure [76]

Several studies used PoDFA and PREFIL as the method of choice to assess melt quality [75-79], and all have found oxide films among the inclusions during the metallography of the filter. The main concern is that, due to the big mesh size of the filter (above 30 microns) and the extreme thinness of new oxide films (few nanometers), a lot of these bifilms may either pass straight through the filter due to their furled form, or wrap tightly around the mesh, making them "invisible" during metallographic analysis [70].

1.5.3 Reduced Pressure Test

Reduced pressure test (RPT), also known as Straube-Pfeiffer test, vacuum density test (VDT) and vacuum solidification test (VST), is an inexpensive and efficient method to evaluate and monitor molten aluminum quality. It is used by thousands of aluminum foundries across the world [80 from 81]. The idea of the RPT test is to let the melt solidify at reduced pressure, so that pore nucleation and growth are favored (see Figure 13).

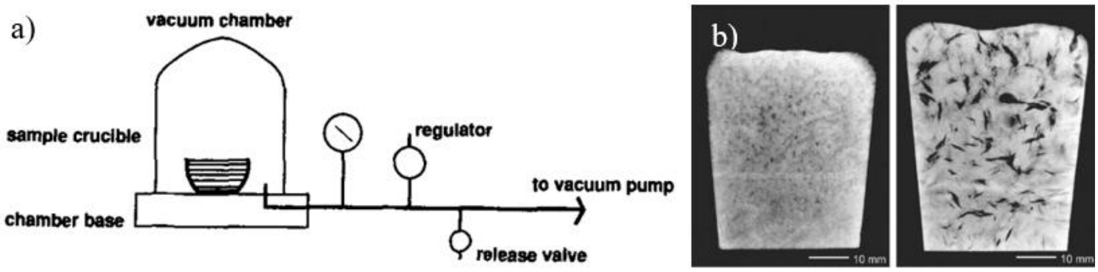

Figure 13: a) RPT equipment schematization [80] and b) typical RPT samples at 1 atm and 0.1 atm [38]

Several parameters can be collected from RPT samples:

- The Bifilm Index (BI).

- The Density Index (DI).
- Distribution, average length, average area, and area fraction of the pores.
- Chemical analysis through SEM and EDX imaging of the pores.

In the following sub-paragraphs, the definition of the BI and DI will be given:

1.5.3.1 The Bifilm Index (BI)

The bifilm index is defined as the total length of bifilms estimated from the sectioned surface of reduced pressure test samples, using the sum of the maximum feret diameter of the pores [82]:

$$BI = \sum (maximum\ feret) = L_B \tag{1.5}$$

The total sum is a length L_B, so it is measured in length units such as millimeters, micrometers and so on.

Uludag et al. have proposed a scale grade system that allows to use the bifilm index as a guide for higher quality melts [68]. The grading system is as follows:

- $0 \leq$ BI ≤ 10 mm: high quality melt
- $10 \leq$ BI ≤ 25 mm: good quality
- $25 \leq$ BI ≤ 50 mm: average quality
- $50 \leq$ BI ≤ 100 mm: unacceptable quality
- BI ≥ 100 mm: bad quality that should be avoided

Unfortunately, as will be discussed in paragraph §2.2.3, this scale system may not be as efficient as it seems.

1.5.3.2 The Density Index (DI)

The density index is defined as the ratio [83]:

$$DI = \frac{\rho_1 - \rho_2}{\rho_1} \times 100 \tag{1.6}$$

Where ρ_1 is the density of the sample cast at atmospheric pressure, and ρ_2 is the density of the sample cast at reduced pressure.

A brief comment should be spent on the choice of ρ_1 in the DI calculation. It might be argued that instead of using the density of a sample solidified at atmospheric pressure, it would be better to use the theoretical density of the alloy that can be calculated starting only from its chemical composition. This would in fact represent the density of the alloy if it really was free from any defects, something that the density of the atm-pressure solidified sample just could never be able to do, since even at atmospheric pressure some microporosity (that reduces the computed density) will still develop.

If the pressure is reduced by 1/100th of the original pressure, it is expected that the residual air layer between the films would be expanded by a factor of 100 [84], so the BI is a *function of the pressure*.

The idea behind the bifilm index, is that by measuring the maximum feret diameter of a pore, we are most likely measuring the length of the bifilm from which the pore nucleated. The errors that could arise from this measurement are of two kinds:

- The bifilm was not completely unfurled, so we are underestimating the length of the i-th pore.
- The bifilm was overinflated by hydrogen, so that it was opened beyond its original length, and we are overestimating the length of the i-th pore.

These two types of errors tend to cancel each other out [19], but at the same time they are the probable cause of the well-known scatter observed between RPT samples [84].

Nevertheless, the bifilm index (and so the RPT) is probably the most promising techniques that we can use today to assess the oxide content.

The combination RPT data (BI, DI…) with hydrogen measurement and tensile test data results in the best attempt to achieve a complete protocol for melt quality assessment.

1.6 Influences on Bifilm Population and Behavior

The population and evolution of bifilms in an aluminum melt is heavily influenced by several parameters that vary from alloy to alloy and foundry to foundry. In this paragraph, some of these variables are addressed and their effect on oxides and entrainment is explained according to the literature.

1.6.1 Influence of Alloy Composition on Bifilm Population

The type and amount of elements in the alloy can influence not only the number of bifilms, but also their shape and chemical composition.

1.6.1.1 Influence of Magnesium

The presence of Mg in the alloy has a great effect on the formation and transformation of the new oxide bifilms floating in the melt. It was shown by Impey et al. [85] that alloying with Mg enhances the rate of oxidation of the melt. Moreover, the mechanism of oxidation of Al-(1-5wt%)Mg also changes in the following manner: the first oxide layer to form on the surface of the melt at 750ºC is the γ-alumina described in §1.4.1, but after about 5 minutes, crystalline MgO develops beneath this layer towards the bulk of the melt. Considering that the diffusion coefficient of Mg in pure Al at 750ºC is 2.72×10^{-11} m^2s^{-1} [86] (i.e., an atom of Mg takes about 3 minutes to travel 100μm), it might happen that the local concentration of Mg in the melt is too low for MgO to form. In this case, the layer beneath the alumina will be of $MgAl_2O_4$ (spinel). In both cases, the growth of these crystalline oxides under the amorphous layer of Al_2O_3 results in significant stresses due to volume discrepancy and ends up in the breakage of the amorphous stratum.

This evolution of the oxides in the presence of Mg has been used to explain a peculiar phenomenon called "healing" of the bifilms [87,88]. Aryafar et al. [89] have demonstrated that an alumina bifilm in A356 aluminum (which contains 0.3%wt Mg) was able to "heal" almost completely after being held at 750ºC for 5 hours. This was deemed possible due to the transformation of the oxide film from alumina to spinel and then from spinel to magnesia.

1.6.1.2 Influence of Iron

Iron is usually an unwanted alloying element in aluminum melts. This is mostly because the presence of Fe in the alloy decreases its ductility almost linearly with the amount of wt% of Fe present [90]. The decrease in ductility is due to the needle-like shape of the iron-rich intermetallics that nucleate in iron containing alloys [22], but it has been shown that the morphology of the intermetallic can be modified by Mn-doping [90] to obtain a "chinese-script" shape.

On the other hand, the presence of some Fe in Die Casting alloys can be beneficial for several reasons, such as reducing the die soldering phenomena, increasing the die life, reducing the cycle times by increasing the high temperature resistance and, possibly, its “cleaning effect”. “Cleaning effect” here is intended to describe the mechanism according to which iron-rich intermetallics can nucleate on the “wetted” side of oxide bifilms and precipitate them to the bottom of the melt [19,91-93]. One of the aspects that tends to proof this theory is again the common observation of central cracks across intermetallics that can advance through the metal matrix (see Figure 14). This crack across the ductile matrix (where crack blunting should be observed) could be easily explained by the nucleation of the intermetallic on a bifilm, which constitutes a pre-crack.

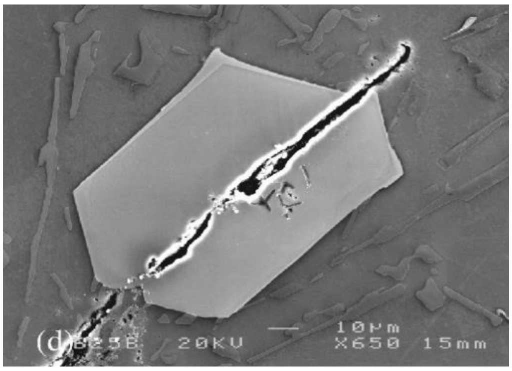

Figure 14: SEM image of Al casting showing a long crack that goes all the way through the intermetallic and into the ductile matrix

Of course, as previously discussed (§1.4.2), the nucleation of intermetallics on bifilms can result in the unfurling of the oxides, with deleterious effects on mechanical properties.

1.6.2 Influence of Melt Handling on Bifilm Population

The way the melt is handled during the different phases of the casting process is probably the biggest influence on the bifilm population.

1.6.2.1 Influence of Pouring

The critical velocity of the melt in casting is defined as the velocity of flow over which the melt has enough energy to rise above the general level of the liquid surface and subsequently fall back under gravity [19]. That is, the velocity at which surface entrainment can be experienced, and for aluminum melts it happens to be around 0.5 m/s. Following this definition, the critical height is the height at which the pouring of the melt results in turbulence and entrainment, because it allows the melt to reach such critical velocity. Equation (1.4) shows the relationship between critical velocity (V_{crit}) and critical height (h_{crit}):

$$h_{crit} = \frac{V_{crit}^2}{2g} \tag{1.7}$$

Where g is the gravitational acceleration.

By substituting 0.5 m/s to V_{crit} we obtain a critical height of about 1,2 cm. This quantity is very small, and even smaller if compared with the heights from which the melt is poured in everyday casting plants, that often exceed 100 cm! In Figure 15, a pouring operation at a BMW casting plant is shown.

Moreover, between the different steps of a casting process, the melt can be poured more than one time from ladle to ladle, increasing the overall damage.

Figure 15: Pouring operation at a casting plant. Note the height at which the metal is being poured from the furnace into the transfer ladle.

1.6.2.2 Influence of Stirring

It goes without saying that, for all the reasons seen until now, stirring the melt has generally been considered a damaging operation. Stirring can induce vortices and turbulence that entrain the surface oxide film, increasing the number of bifilms floating in the melt.

Nevertheless, this paragraph wants to highlight some curious findings that may correlate stirring to the healing of bifilms (see §1.6.1), with the reminder that, if the stirring operation is carried out without inducing any turbulence or surface-vortices, then entrainment can be greatly reduced. In one of these studies [94], it emerged that by stirring the melt at specific speeds with a graphite rotor, the percentage porosity, bifilm index and average pore size of RPT samples decreased with time. These results were first interpreted assuming that the stirring induced stresses on the bifilm defects, increasing the rate of formation of cracks on their oxide layers and the rate of diffusion of hydrogen gas into the bifilms, causing them to expand and become more buoyant. This would cause a rapid flotation towards the surface of the oxide defects, with a reduction of their concentration with respect to a stagnant melt.

Even if this explanation seems sufficient, a second study that repeated the experiment on melts with different contents of magnesium in the alloy proposed a different solution to the problem [95]. After stirring the melts at different speeds, it was shown that, again, the percentage porosity and the pore number density decreased clearly for the intermediate stirring speed (85 RPM), and that this reduction was slightly influenced by the amount of alloying magnesium. By analyzing SEM pictures of the pores, the authors concluded that the stirring improved the rate of diffusion of Mg in the melt (the diffusion coefficient of Mg in pure Al melt at 750ºC is relatively low: 2.72×10^{-11} m^2/s), providing enough Mg for the transformation of the alumina layers of the bifilms to spinel and increasing the entrained atmosphere's consumption. The increased crack formation combined with the icreased Mg diffusion are the two ingredients required for bifilm healing [122,123], that is the chemical bonding of the two oxide surfaces thanks to entrapped atmosphere's consumption and transformation of alumina to spinel or magnesia. However, at higher rotational speeds, the damaging effect of the stirring by oxide entrainment was higher than its beneficial effect.

1.6.2.3 Influence of Holding Time

The holding time refers to the amount of time at which the aluminum alloy is held at the liquid state before casting or sampling.

The effect of holding time on bifilms and melt properties has been investigated by many researchers on different alloys and often in conjunction with other variables (like degassing, refining and Sr modification), so that in the end is difficult to summarize form these different works a clear conclusion. What emerges in the end are two diametrically opposite theories:

1) An increased holding time (greater than 10 minutes) is beneficial to the melt since it increases the Weibull modulus of the tensile properties in commercially

pure Al, possibly due to the diffusion of hydrogen into the bifilms and their consequent expansion, leading to an increase in reproducibility of the casting properties [96]. Moreover, increased holding times for Al-7wt%Si-Mg casting alloys was linked to natural degassing of the melt due to bifilm flotation [67]. According to these results it would seem that an increased holding time has some beneficial effect on the melt quality.

2) A reduced holding time (around 10 minutes) has been observed to be the most beneficial to the melt quality [97,98], since it increases the tensile properties of the alloy with respect to 0 minutes and 20+ minutes holding times. It is true that the hydrogen tends to increase in the melt with increased holding time, but this increase at 10 minutes appears to have a beneficial effect due to the flotation of oxides.
   Other studies have found that a much higher holding time (between 20 and 240 minutes) decisively decreases tensile properties and bifilm index of the cast component [99,100], but interestingly this degradation is much less relevant (if not at all absent) in melts who have been degassed.

In conclusion, the effect of holding time on the quality and the mechanical properties of the casting has not yet been understood completely and more research is needed.

1.6.2.4 Influence of Mold Design

Melt damage comes from double film oxides, and double film oxides come from surface turbulence and entrainment. For this reason, a turbulent filling of the mold will result in oxide entrainment and lower quality of the casting.

It has been shown that even by starting from a clean melt and by keeping it clean all the way to the pouring step, if the filling of the mold involves turbulence, the end result will be poor [19,28,38,101]. On the other hand, a clean melt which is handled in the correct way all the way to the pouring operation will yield a high-quality casting, such in the case of the Cosworth process castings. As already mentioned, casting plants who apply this innovative casting technology have obtained promising results in terms of quality of the castings even with minimal melt treatment (i.e. Sr treatment and degassing).

Basic reccomendations for mould design include:

- Careful shaping of the pouring basin, with implementation of an offset blind end, weir (or step) and the provision of a generous radius over the top of the step.
- Tapering of the sprue and correct sizing in order to grant the least possible turbulence.
- Correct sizing and shaping (rectangular) of the runner in order to ensure lowest possible filling velocity.
- Correct sizing and shaping (rectangular, thin and wide) of the gating system in order to both ensure lowest possible filling velocity and avoid premature freezing.

Nevertheless, as long as the metal will be top-poured into the mould, there will always be entrainment.

1.6.3 Influence of Hydrogen on Bifilm Population

Hydrogen has a passive influence on bifilms. In the words of Dr. Tiryakioglu: “Hydrogen acts as a flashlight that casts light on bifilms. When there is no light, we cannot see bifilms, but this does not mean that they are not there.”

In other words, in the view of Tiryakioglu (and Campbell, Dispinar, Uludag etc...) hydrogen is little more than just an instrument with the ability to higlhlight the presence of bifilms in the melt. In these terms, the amount of hydrogen present in the melt would have little effect on the properties of the final casting, the only difference being the number of “opened oxides”. In the ideal case of a clean melt without bifilms, the amount of hydrogen dissolved in such melt would have no effect on the final (high) quality of the melt. In the opposite (less ideal) case of a very dirty melt, hydrogen would have a much clearer effect:

- For very low amounts of dissolved hydrogen, the cast component would appear almost defect-free at a first glance, because of the little amount of bifilms opened by the gas and shrinkage effect. Note that the expected mechanical properties would still be poor, because of the presence of crack-like unopened bifilms.
- For high amounts of dissolved hydrogen, the cast component would develop many elongated pores or spherical pores (depending on variables such as solidification pressure, mould design, cooling rate), namely bifilms opened by gas nucleation. Expected mechanical properties would be poor.

In reality the relationship between hydrogen and oxides is much more complex than this, and one of the main objectives of this thesis is to further investigate it.

1.6.4 Influence of Grain Refiners on Bifilm Population

Grain refinement is the process of reducing the grain size of the aluminum casting by the use of one of the following strategies [102]:

- Vibration and stirring
- Severe plastic deformation
- Addition of grain refiners

The addition of grain refiner to aluminum alloy has become a common industrial practice to achieve grain refinement of casting aluminum alloy. When the grain refiner is added, it introduces a incredibly large amount of heterogeneous nucleation sites for α-Al, and this ensures a reduced final grain size in the solidified product. Some examples of grain refiners are proposed in Table 3 [102].

GRAIN REFINER	Al ALLOY
Ti	High purity Al
Cu	High purity Al
Mg	High purity Al
Al–5Ti–0.3C–0.2B	Commercial pure Al
Al–5Ti–1B	Commercial pure Al
Al–Ti–C	Commercial pure Al
Al–3B–5Sr	A356
Al–1Nb–1B	Al-12Si
Al–5Ti–1B	6063

Table 3: Examples of grain refiners and alloys in which they are used

As can be seen in Table 3, a big portion of grain refiners contains titanium, which will be released from the master alloy at the time of addition to either form TiB_2 or TiA_3. These intermetallics will act as the heterogeneous nucleation sites, but as efficiently as they will nucleate α-Al, the discrepancy in density between them and the molten metal may result in a problem: the intermetallics tend to sink to the bottom of the crucible and to sediment there with time. Due to this aspect the efficiency of this kind of refines has been debated in the past [103,104]. But as deteriorating as this effect may be for the refining effect, some authors have speculated a much more favorable effect that could arise from the sedimentation of the heavy intermetallics [19,67,105]: these researches have all correlated a reduced bifilm index in the case of addition of grain refiners to the sedimentation of bifilm, that would be actively dragged to the bottom of the crucible by the heavy particles. Nevertheless, it is worthy to mention that the addition of grain refiners in the melt increases the number of bifilms due to the surface entrainment.

1.6.5 Influence of Scrap Additions on Bifilm Population

Scrap consists of recyclable materials left over from product manufacturing (internal scrap) and consumption (external scrap). Depending on the type of scrap and its origin, scrap could be more or less polluted with undesired elements and chemicals, but what characterizes all sorts of scraps is the high presence of oxides. In the specific case of internal scrap, which is recycled within the processing plant and is therefore much more controlled in composition, the high number of oxides will be present due to the previous casting operations (see §1.6.2) and the oxidized surface of the component. This high concentration of oxides at the time of melting will result in an increase in the bifilm population of the melt, with a consequent increase in bifilm index.

Some studies have addressed the effect of the addition of scrap to pure ingots [106-108], and what emerges is that the integration of recycled material into the melt defenetly increases the scattering of the results during quality assessment and almost always increases the bifilm index and reduces the ultimate tensile streght. Some authors speculate that the sometimes “not-so-evident” increase in the BI may be because of the flotation of the big old oxides introduced with the scrap due to their high bouyancy [107].

Anyway, as new green economies and politics increase the pressure on industries such as the automotive, with goals like the one proposed by the IEA (International Energy Agency) that aims at “cutting CO2 emissions levels in 2050 to 30% below 2005 levels for the transport sector” [109], the importance of aluminum scrap recycling is blatantly going to increase in the near future. Optimistic forecasts claim that already by 2050 a 25% reduction in primary aluminum could be expected in favor of scrap use [110]. Of course, this strongly depends on future scrap sorting technology and, as hinted in this paragraph, on the ability to control the negative effects linked to scrap addition.

1.6.6 Influence of Hot Isostatic Pressing on Bifilm Population

Hot isostatic pressing (HIP) involves the simultaneous application of a high pressure and elevated temperature to a cast component in order to supposedly increase its properties [111]. With the application of this pressure by means of a gas (therefore isostatic), internal pores or defects within a solid body collapse and, hopefully, diffusion bond.

Because of the involvement of high temperatures and pressure, the HIP equipment can be very expensive and most metal injection molding producers outsource this operation to an external vendor that specializes in HIP [112]. This results in hefty increases in costs and in longer manufacturing times.

At least at first glance, HIP seems to be a great counter-measure to oxide porosity in aluminum cast products, despite the evident cost-related drawbacks. Suggestions from Nyahumwa et al. that when a cast Al-7Si-0.3Mg alloy was subjected to HIP treatment (hipping) close to the eutectic temperature, the applied pressure closed the oxide porosity and induced chemical bonding between the two layers [88], only encourage further research into the benefits of HIP in aluminum cast components.

It is interesting to mention that some skepticism could result from the comparison between data collected from HIP treated components and the maximum ductility potential estimated by Tiryiakioglu et al. [59]. For example, Ran et al. demonstrated that HIP increased the elongation at fracture of A356-T6 cast samples as much as 45% (Figure 16) [113], but as soon as this result is compared to the theoretical maximum ductility potential proposed by Tiryakioglu, the increase in ductility seems almost negligible (Figure 17) [114].

Similar considerations can be drawn replacing data from Ran with the results from Yue & Chadwick [115]. In this case, instead of HIP, the components were produced via “squeeze casting”, a combination of casting and forging by which the melt solidifies under high pressures (100 MPa in this case). For a LM24 alloy, squeeze casting increased the elongation from 2% to 2.7%, against the 29% and 27.9% respectively estimated as “maximum” ductility potentials.

Of course, this considerations do not address the issue that questions if these estimated maximum ductility potentials are actually achievable.

In conclusion, HIP and squeeze casting defenetly provide an improvement in terms of mechanical properties to the cast aluminum component, but whether this increase is justifiable in terms of costs can be debated.

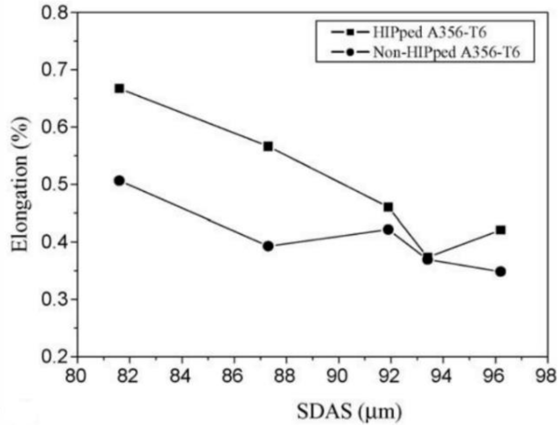

Figure 17: Increase in elongation due to HIP treatment as a function of SDAS [113]

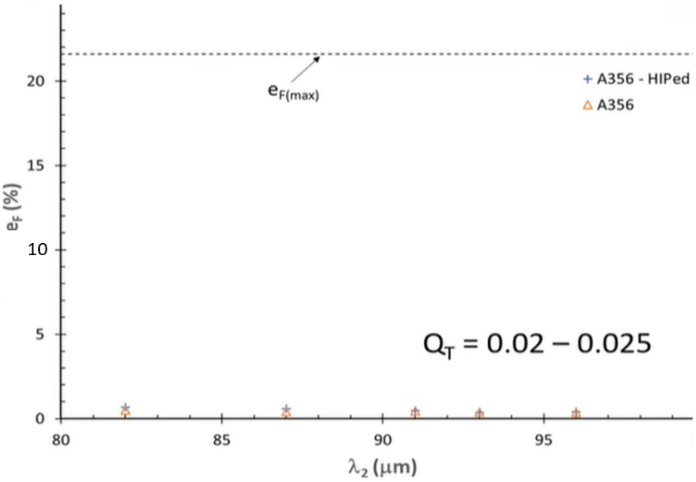

Figure 16: Increase in elongation due to HIP treatment as a function of SDAS, related to the maximum estimated ductility for A356-T6 [114]

CHAPTER 2

EXPERIMENTAL PROCEDURE

2.1 Experiment's Purpose

The processing variables that actively influence casting processes of aluminum alloys are many: the type of alloy, the melting temperature, the presence of scrap, the type of melting furnace, melt treatments, hydrogen, melt handling, casting technology, mould design etc…

Due to the high number of variables, whenever we are interested in evaluating the effect of only a few of them on the melt, it is important to keep all the others as constant as possible. The lack of control on other variables or, similarly, the controlled use of several variables at the same time, often results in scattered and hard-to-interpret data. As simple as this rule might seem, it is far from easy to observe. The issue is that some of the variables are very difficult to eliminate from the equation and their effect resonates through the results of the experiment, increasing the scatter.

In the case of the experiment on which this thesis is redacted, particular focus was oriented on this problem.

2.1.1 Experiment's Purpose

The purpose of this experiment was to investigate the peculiar relationship between hydrogen and oxide bifilms under the variation of the following parameters:

- 100% ingot vs 100% scrap melt
- "Clean" undisturbed melt vs "dirty" damaged melt

Moreover, the experiment intended to study the effect of this relationship on the development of porosity of RPT samples and, therefore, its effect on the results of a standard melt quality assessment operation.

As previously hinted in §1.6.3 and the rest of the first chapter, the role that hydrogen is believed to play in defect formation has recently changed drastically. If in the past hydrogen was believed to be an “active” generator of defects (nucleating bubbles in the casting), now its role is thought to be “passive”, first and foremost because it has been demonstrated that heterogeneous and homogeneous nucleation of this gas in molten aluminum is impossible to occur. Hydrogen nucleates only in the presence of oxide bifilms, between the oxide layers, bloating them into cracks and bubbles. Therefore, in the case of an ideally clean melt (i.e. without any bifilm) no gas porosity should be observed.

Keeping all this in mind, let us consider two different melts:

- Clean melt with reduced oxide content,
- Dirty melt with high oxide content.

We want to vary the hydrogen content of these two melts in order to obtain an “high” hydrogen version and “low” hydrogen version of each (total of 4 melts), and cast RPT samples from each melt in order to calculate the Bifilm Index. If we were to plot the calculated BI of each melt as a function of the hydrogen content, what would we expect to see?

If hydrogen really is just a “flashlight” that exposes the oxides already present in a melt, and we assume that we were careful enough to keep the sampling procedure as repeatable as possible, the plotted data should assume the form proposed in Figure 18.

To explain this plot we can discuss each individual melt separetly:

- Clean melt, low hydrogen: in this case we definetly expect a low bifilm index. The low amount of oxides is even less visible due to the low amount of hydrogen gas, that cannot open the bifilms efficiently. Therefore we find the points in the lower left side of the graph (Figure 18).
- Clean melt, high hydrogen: now the hydrogen is able to expand the oxides, but since they are present only in a very small number, we cannot expect to see a big increase in the BI. Therefore we find the points in the lower right side of the graph (Fig. 18).
- Dirty melt, low hydrogen: the high number of oxides cannot be opened by the low amount of hydrogen dissolved in the melt. Therefore, even if the melt is dirty, the observed BI in the RPT samples is expected to be low. If the hydrogen is low

enough, we can actually find the points in the lower left side of the graph, almost coinciding with the clean / low hydrogen melt.

- Dirty melt, high hydrogen: the high number of oxides can now be opened by the nucleation of hydrogen gas. The bifilms expand and increase the BI of the RPT sample. Therefore we find the points in the upper right side of the graph (Fig. 18).

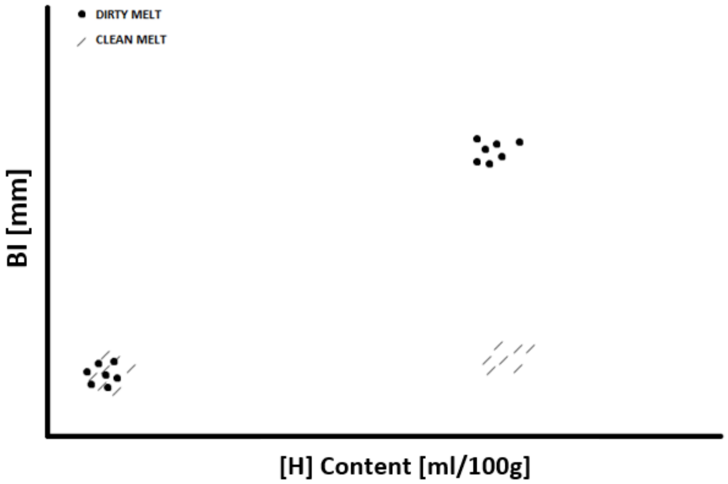

Figure 18: Example of expected correlation between hydrogen content ([H]) and bifilm index (BI) in both a clean and dirty melt. Note how the influence of hydrogen on the BI of the clean melt is expected to be inferior than in the dirty melt condition

This experiment tried to simulate a condition as close as possible to the one just described, in order to empirically verify the theoretical outcome discussed above. Moreover, the mechanical properties were investigated to correlate them to the hydrogen content and melt quality.

In order to do so, 6 melts were prepared according to specific conditions and studied:

- ILL (I = Ingot, L = Low Oxides, L = Low Hydrogen): prepared starting from 100% ingots and with low hydrogen content.
- ILH (I = Ingot, L = Low Oxides, H = High Hydrogen): prepared starting from 100% ingots and with high hydrogen content.
- SLL (S = Scrap, L = Low Oxides, L = Low Hydrogen): prepared starting from 100% scrap and with low hydrogen content.
- SLH (S = Scrap, L = Low Oxides, H = High Hydrogen): prepared starting from 100% scrap and with low hydrogen content.

- IHL (I = Ingot, H = High Oxides, L = Low Hydrogen): prepared starting from 100% ingots and with low hydrogen content. The melt was then subjected to several pouring operations in order to increase the amount of "new" oxides.
- IHH (I = Ingot, H = High Oxides, H = High Hydrogen): prepared starting from 100% ingots and with high hydrogen content. The melt was then subjected to several pouring operations in order to increase the amount of "new" oxides.

The "high hydrogen" level could be expressed as the condition [H] ≥ 0,3 ml/100g, while the "low hydrogen level as [H] ≤ 0,1 ml/100g.

Note that in Chapter 3 these melts may be addressed as follows:

- Melts IL: Include melts ILL and ILH and may also be referred to as the "clean ingot melts". IL melts allowed us to study the effect of low and high hydrogen levels on the 100% ingot melt.
- Melts SL: Include melts SLL and SLH and may also be referred to as the "scrap melts". SL melts allowed us to study the effect of low and high hydrogen levels on the 100% scrap melt.
- Melts IH: Include melts IHL and IHH and may also be referred to as the "poured ingot melts". IH melts allowed us to study the effect of low and high hydrogen levels on the 100% ingot "damaged" melt.

Therefore, the objective of this experiment was not only to verify the statement depicted in Figure 18, but also to investigate the effect that the nature of the oxides that make a melt "dirty" have on such statement. In fact, melts SL are characterized by "old oxides", while melts IH mostly by "new oxides".

Scheme 1 resumes the 6 different melt conditions of this experiment:

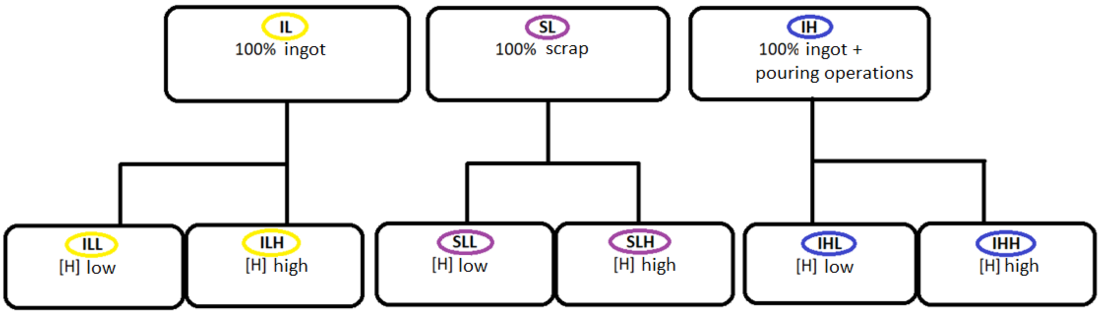

Scheme 1: block scheme of the 3 melt classes (IL: 100% ingot, SL: 100% scrap, IH: 100% ingot + pouring op.) and their low and high hydrogen conditions.

2.2 Development of a Reliable Image Analysis Protocol

A crucial point of this study lied in the data collected from the RPT samples. Therefore, before the main experiment could be carried out, it was necessary to develop a reliable and repeatable image analysis protocol that allowed us to collect such data.

2.2.1 Important Image Analysis Parameters

One main issue with RPT surface image analysis is that no officially accepted standard exists. For this reason, we first need to understand what parameters define a good image analysis protocol.

- SURFACE GRINDING GRIT: In order to efficiently analyze a surface, whether by scanning or optical microscopy, such surface should first be ground. Alas, when it comes to the grit of choice for RPT samples the literature is very ambiguous, and among the many that don't even mention this decision in the experimental procedure[68,82,84,101,107,116-118], the few that do are rarely in agreement. For example, sometimes a 600 grit seems to be enough [62,99], while in other cases the authors turn to 1200 [119] or even to polishing.
- IMAGE RESOLUTION: The lack of a standard in the grinding step exists because this operation is tightly intertwined to the resolution used during the image aquisition step. The resolution or dpi (dots per inch) of an image is a function of the instrument used to capture it. A common instrument used to capture images from the RPT sample sections is the scanner and its dpi depends on the specific machine and settings. Different studies opted for different resolutions, that go from 300 dpi [95], to 600 dpi [67,120] all the way to 1200 dpi [119,121]. Even if this might seem like a minor influence on the results, it should be reminded that bifilms are extremely heterogeneous entities that can range from the scale of the centimeter down to the microscopic scale. A resolution of 300 dpi corresponds to approximately to 11.8 pixels/mm (or 0.0118 pixels/µm), so that bifilms of the size of tens of microns could go undetected. This can be acceptable, as long as it is clear that the results achieved with such resolution will probably differ from results at higher resolutions.
- LOWER DETECTION LIMIT: The lower detection limit (LDL) refers to the smallest defect that should be counted by the image analysis software when

computing the porosity. It is usually set in the form of an area and is needed to reduce the error during BI calculation. To emphatize the importance of such limit we can linger on the following example: if we take a generic RPT section image from the experiment of this thesis (sample ILL2, Figure 19) and we perform the poroisity analysis without setting any LDL, the software will count a total of 11770 individual pores! This is an obviously misleading number, that has further negative effects on the BI calculation (it more than doubles in value with respect to the following LDL). On the other hand, setting 200000 μm^2 as the LDL, the software counts a total of 48 pores. Nevertheless, it should be underlined that this LDL is still very small with respect to some of the values proposed in the literature: Campbell suggests that BI calculation could be done by a human operator with naked eye and the aid of a ruler [19].

Figure 19: Surface of a generic RPT sample collected during the experiment

The 200000 μm^2 (i.e. 0,2 mm^2) LDL was chosen because it offered the best compromise between noise reduction and actual porosity detection. Of course, such a strict limit demands for very high image resolution and fine enough surface grinding, two requirements that were observed in this experiment (see §2.3). Note that a perfectly round pore whose area is 200000 μm^2 would present a diameter of around 250 μm, or 0,25 mm.

2.2.2 Trials To Develop The Image Analysis Protocol

The development of the image analysis protocol required some trials to adequately calibrate the parameters and study their effects on the final results. In order to do so, image analysis was conducted on two sets of RPT samples collected during two different experiment at Jonkoping University by a PhD student, Qing Zhang. The samples were the result of studies on aluminum melt treatments that were different in nature.

2.2.2.1 First trial

The objective of this first trial was to assess the effectiveness of a faster image acquisition process that will be called “Procedure A” with respect to a slower, more reliable process that will be called “Procedure B”.

The RPT samples collected from the first experiment were already cut along the axis, and they either came from melts of EN-AC46000 ingots or EN-AC46000 internal scrap. The image analysis was carried out according to the following steps:

- One of the two halves of the RPT sample was ground up to an 800 grit with sand paper, in order to remove the deep scratches caused by the cutting process.
- The surface was then left to dry and analyzed with an optical microscope (Olympus DSX 1000) with 3x zoom. Two different approaches (A and B) were followed to acquire the images from the surface:
    A. 10 images, each of size 6400x6400 μm, were collected from each sample from specific areas of the surface (4 along the axis and 3 from each side) (see Figure 20, left). The idea behind this procedure was that 10 images taken from specific spots could accurately represent surface porosity.
    B. Several images were taken (49 or 56 total in 7x7 or 7x8 grids respectively, depending on sample size), each of size 6400x6400 μm, and automatically stitched together by the microscope’ software to capture the whole surface of the sample (see Figure 20, right). This procedure allowed to analyze the whole surface, but was significantly slower.

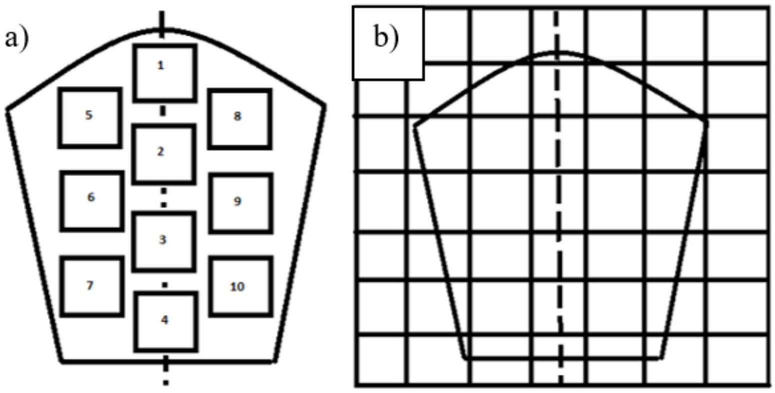

Figure 20: Image sampling example according to procedure A and B. a) The pattern followed on the RPT surface during the 10 image acquisition in procedure A. b) Grid of 7x7 images stitched together to obtain full RPT surface image in procedure B.

- The pictures (10 for procedure A and 1 single stitching for procedure B) were analyzed using ImageJ software according to the following recipe:
    i. Convert image to 16 bits;
    ii. Set threshold manually in order to highlight darkness of pores and lightness of surface;
    iii. Apply manual adjustments with brush and selection tool in order to reduce noise;
    iv. Use the "analyze particle" option to extract the following information: number of pores, area of pores, maximum Feret of pores, perimeter of pores.
    The software was instructed not to consider particles (i.e. pores) with surface area lower or equal to 5000 μm^2. This was the LDL.
    v. Manually trace and let the software compute the sample's surface (only needed for procedure B).
- The data, collected from ImageJ in form of excel tables that listed information regarding each single pore, were then elaborated to get the total, average and standard deviation of the feret, area, and perimeter of the pores. The bifilm index (BI) consists of the sum of the maximum ferets of pores:
    A. For procedure A, the bifilm index became the sum of the ferets from all 10 images.
    B. For procedure B, the bifilm index became the sum of the ferets of the 7x7 (or 7x8) stitching.
- The final results were then summarized and analyzed.

The comparison between procedure A and B showed evidence of discrepancies between them. As can be seen in Table 4, the final ranking of samples according to the BI was not the same for A and B. Therefore, assuming that procedure B is the most reliable since it considers the whole surface instead of 10 isolated sections, the fastest procedure (A) was abandoned in favor of procedure B.

PROCEDURE B (full surface)		**PROCEDURE A (single images)**	
SAMPLE	BIFILM INDEX [mm]	SAMPLE	BIFILM INDEX [mm]
A	72,6	A	26,9
B	155,1	C	66,5
C	163,2	D	72,4
D	166,6	B	90,2
E	210,6	E	102,1
F	257,6	G	113,6
G	264,4	F	129,1
H	341,2	H	150,2

Table 4: Comparison between results from procedure B and procedure A for bifilm calculation. NOTE: the high values of BI are due to the very low LDL.

2.2.2.2 Second Trial

The objective of this second trial was to determine both the sample collection's technique and a suitable LDL value during the image analysis protocol. The experiment at the base of this trial, from which the samples were borrowed, had the different objective of investigating the effects of holding time and flux addition on melt quality. Anyway, as for the first trial, these objectives were different and beyond the interests of this thesis, so they will not be discussed any further.

Samples were collected from 1.3 tons of EN-AC46000 scrap that was melted in an induction furnace and then poured in a resistance furnace, where the holding time started. The RPT sample collection method was repeated for two methods:

1) POURING: according to this method, the surface of the melt was first skimmed to remove dross and surface oxide, then a preheated metal spoon was immersed to collect a small quantity of melt that was rapidly poured into an RPT cup

immediatly before closing the glass bell of the RPT machine and applying the vacuum.

2) IMMERSING: as above, the surface of the melt was first skimmed, than the RPT cup was directly immersed into the melt. The cup was grabbed by its flattened rim using a pair of pliers and carefully lowered ”head-first” into the melt (see §2.3), then placed into the vacuum chamber. This procedure aimed to reduce the damaging effects of the “pouring” action (see §1.6.2).

The difference between pouring and immersing the RPT cup had already been investigated by Gyarmati et al. [124] and, according to their results and by extension of basic concepts of the bifilm theory, immersion of the cup should result in more reliable and accurate results, that should describe the quality of the melt rather than the quality of the sampling process. The reason why in this trial both methods were implemented was mostly to prove this difference to the specific foundry. To this day, many foundries (such as the one mentioned above) still collect samples by pouring during melt quality assessment operations.

As can be seen in Figure 21 and Figure 22, the superiority of immersion was clearly shown by the sample’s analysis. Since we can state that the ideal RPT sampling method would not damage the melt, but at the same time would defenetly not be able to improve its quality, when comparing two different sampling methods the best one can be identified as the one that yields the ”cleanest” sample.

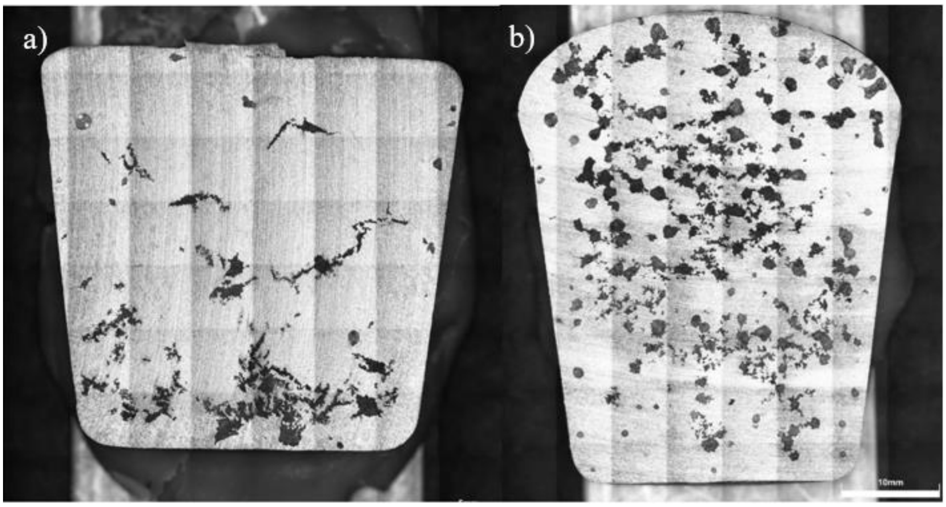

Figure 21: Two samples from the same melt and conditions. a) immersed, b) poured

Regarding the y-axis in Figure 22, the ”Specific Bifilm Index” (SpBI) of a sample is defined according to Equation 2.1:

$$SpBI^{m} = \frac{BI}{m_{sample}} \tag{2.1}$$

Where m_{sample} is the mass of the sample whose BI stands at the numerator. The apex ”m” denotes normalization with respect to the mass of the sample.

The specific BI is a version of the BI that has been normalized to the mass of the sample, increasing data comparability. The size of the sample directly influences the BI, and bigger samples will tend to have bigger BI than smaller samples.

What is important to notice in Figure 22 is the superiority of the immersion method that, on average, yields samples with lower specific BI than those by pouring method.

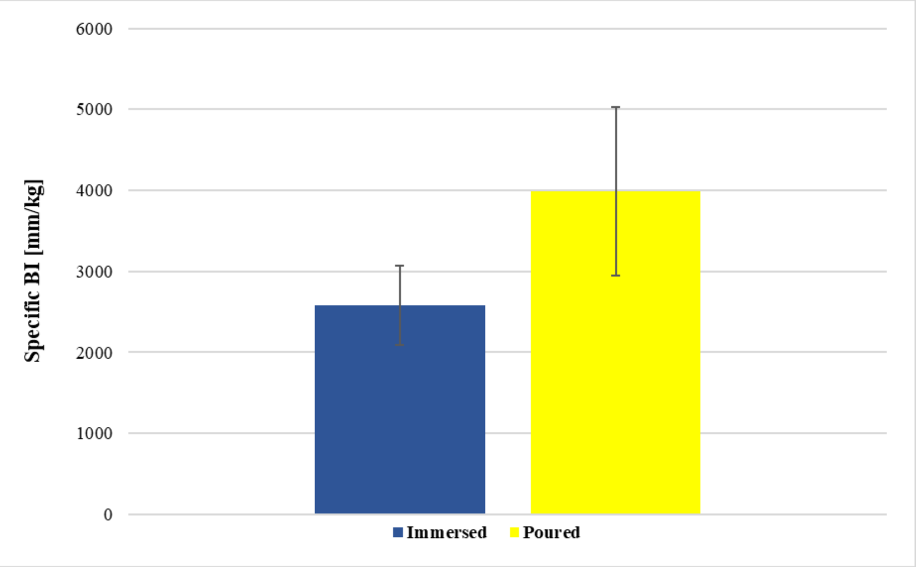

Figure 22: Average specific BI comparison between samples collected by immersion and by pouring methods. Notice that the "Immersion" condition results in lower specific BI

The second important conclusion drawn from this trial concerned the LDL (lower detection limit). In the first trial, the LDL used during the image analysis process was set to 5000 μm^2, a value that seemed to be too low during the analysis procedure. The main issue with a threshold this low is that the noise generated from surface scratches and other sources could easily survive the LDL application. For this reason, a new LDL (25000 μm^2) that removed every “perfectly round” pore with a diameter under 90 μm was tested. The results showed that this LDL reduced noise-porosity interactions with respect to the 5000 μm^2 limit, but was still too low. For this reason, a final LDL of 200000 μm^2 was chosen for the image analysis protocol of the experiment that concerns this thesis.

2.2.3 Specific BI Considerations

It is worth to further discuss the importance of a normalized bifilm index and the different types of normalizations that could be operated on such index. Mainly, one could think of two possible normalizations:

- With respect to the surface of the sample,
- With respect to the mass of the sample.

At first glance both options seem viable, since both allow to relate the BI to the “size” of the specific samples, so that smaller samples with small BI can be correctly compared to bigger samples with intrinsically bigger BI. The problem lies in the relationship that exists between porosity and surface area: greater porosity and/or bigger pores directly increase the surface area of the sample. On the other hand, the mass of the sample is indipendent from the amount of porosity and average pore dimension. Figure 23 shows this idea: the mass of sample SLH2 is just 0,8% greater than that of sample SLL6[N], but, at the same time, surface area of SLH2 is 22,8% greater than that of SLL6!

$$\frac{m_{SLH2}}{m_{SLL6}} = 1{,}008 \qquad \frac{A_{SLH2}}{A_{SLL6}} = 1{,}228 \tag{2.2}$$

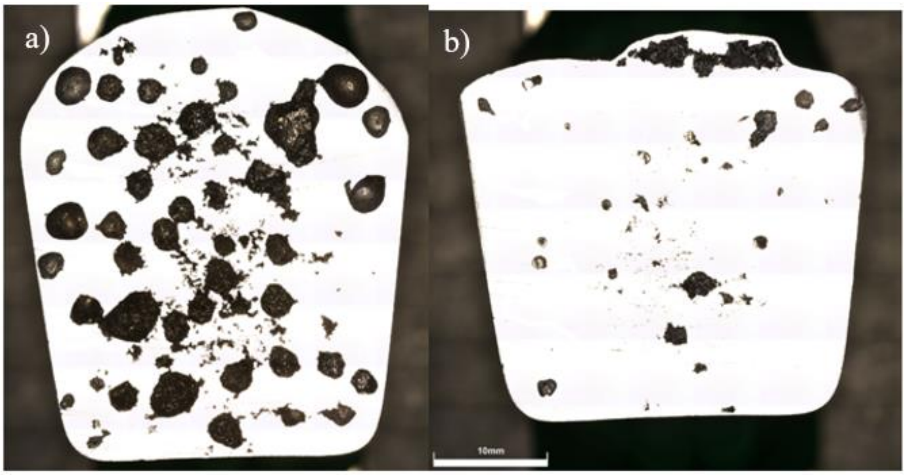

Figure 23: Comparison between two samples. a) SLH2, m = 66,87g, A = 1534 mm^2; b) SLL6, m = 66,31g, A = 1249 mm^2

The influence of porosity on surface area leads to an underastimation of the specific BI in the case of normalization by means of surface area for highly porous samples.

[N] **Melt codes: ILL** (100% ingot, low [H]), **ILH** (100% ingot, high [H]), **SLL** (100% scrap, low [H]), **SLH** (100% scrap, high [H]), **IHL** (100% ingot + pouring operations, low [H]), **IHH** (100% ingot + pouring operations, high [H])

For example, the ratio between the specific bifilm indices (SpBI) of SLH2 and SLL6 change as follows:

$$\frac{SpBI^{A}_{SLH2}}{SpBI^{A}_{SLL6}} = 4{,}007 \qquad \frac{SpBI^{m}_{SLH2}}{SpBI^{m}_{SLL6}} = 4{,}881 \tag{2.3}$$

Where $SpBI^{A}$ is the specific BI referred to surface area.

At last, it should be noted that in the literature it is very hard to come across studies that compare RPT samples by means of an SpBI. This is undesirable, since not normalizing the BI at all (not by means of area, nor by means of mass) can generate even greater confusion during the data analysis step. As a last example, we might take the samples SLL3 and SLL5, both from the same melt conditions (see §2.3). Sample SLL3 is smaller and presents lower BI compared to SLL5 (57,7g - 41,45mm and 91,1g – 66,79mm respectively), but by mass normalization it results that SLL3 actually has an higher SpBI compared to SLL5 (77,18 cm/kg vs 68,18 cm/kg).

The difference that results by using the un-normalized BI instead of the SpBI may be reduced between samples of the same melt if the operator is careful/experienced enough to always collect the same amount of melt during sampling.

2.3 Experimental Procedure: Sample Collection

The first part of the experiment consisted in crafting the gassing and degassing system, testing it and optimizing its effect on the melt. In a second phase, all the melts were prepared, upgassed or degassed, samples collected and gas level monitored. In the final phase of the experiment, samples were prepared and analyzed, and data collected.

2.3.1 Development of a Degassing/Upgassing System

The main objective of the experiment required for hydrogen gas to vary consistently between melts, in order to obtain a LOW hydrogen melt and a HIGH hydrogen one for each of the three starting conditions (100% ingot, 100% scrap, 100% ingot poured). To do so, a degassing/upgassing system had to be built from scratch and tested.

After considering different options, the best solution seemed to be the one schematized in Figure 24: a 5mm steel tube covered by 3 dense graphite cylinders (Ellor® +35 by Le Carbone – Lorraine) and ending in a porous graphite cylinder from which the gases could diffuse into the melt. All cylinders were drilled with the use of a lathe. The tip of the degasser was designed to float around 3 to 4 cm over the bottom of the crucible.

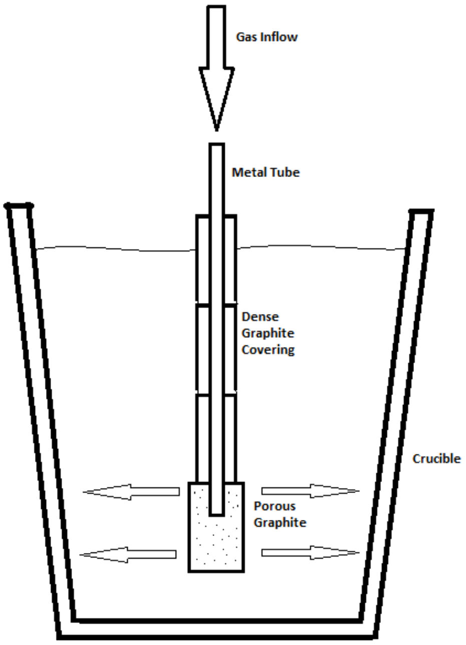

Figure 24: Schematization of the graphite-based degassing system

Previous experience had shown that the dense-graphite covering was fundamental, since the steel tube would be corroded by the molten aluminum if the two were to come in contact, due to the high solubility of iron in molten aluminum. Therefore, it was necessary not only to cover the tube, but also to ensure complete sealing of the gaps between the cylinders. In order to do so, a ceramic adhesive was applied over all the gaps (Resbond® 940LE Base mixed with Resbond® 940LE Activator by Final Materials) as shown in Figure 25.

Note that, between different melt preparations, sometimes it was necessary to re-apply such ceramic coating due to the appearance of cracks.

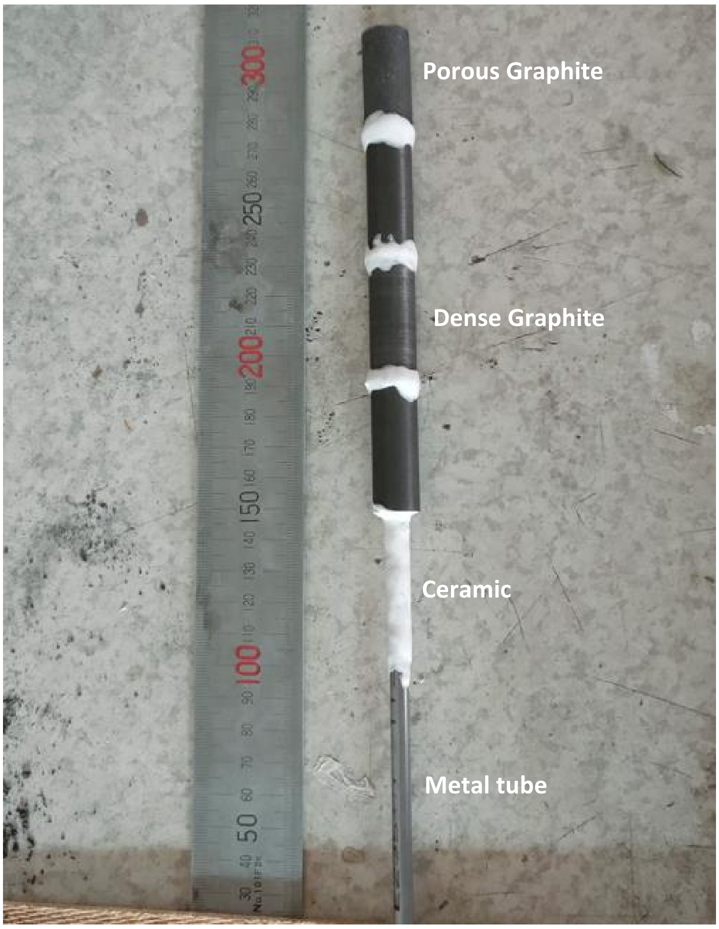

Figure 25: Graphite degassing lance after ceramic adhesive application (in white)

A test was run in order to determine the efficacy of the upgassassing system.

2.3.2 Upgassing Test and Melt Preparation

For the correct evaluation of the efficiency of the upgassing system, the melt was prepared according to the same procedure that was then used for the remainder of the experiment. It is therefore time to discuss the melt preparation procedure in detail, restating that it coincides with the one later used for all the melts discussed in this experiment (with the exception of the raw material employed).

2.3.2.1 Metal Melting and Hydrogen Measuring Setup

The raw material, approximately 6 kilograms of 100% ingot, was molten into a Nabertherm® crucible furnace set at 800°C. The clay crucible had a maximum Al capacity of 7 kg, height of 22 cm and OD_{upper} of 18 cm (i.e. upper outer diameter).

A sample was collected for the chemical analysis as soon the metal reached the liquid state and analyzied with a SPECTROMAXx® machine by Amtek, which detected the composition of Table 5.

ALLOY COMPOSITION							
Element	Si	Fe	Cu	Mn	Mg	Cr	Ni
Wt. %	10,97	0,797	0,0386	0,356	0,0087	0,0196	0,0035
	Zn	Ti	Bi	Ca	Sr	Al	
	0,0392	0,0207	0,0041	0,0005	~ 0	rest	

Table 5: The composition of the alloy used in the experiment (wt%)

To monitor the amount of hydrogen dissolved in the melt a mobile hydrogen analyzer by HYCAL® was employed. The probe of the machine was lowered into the melt as soon as the alloy reached the liquid state and the probe's tip reached a temperature of 600°C, and the top of the crucible was covered with a layer of high temperatrue ceramic fiber cloth to avoid heat losses. The setup for hydrogen measuring is depicted in Figure 26.

Figure 26: Hydrogen measuring setup. TOP: Hycal machine, BOTTOM: The probe is lowered into the melt and the measuring starts

At this point the hydrogen level could be monitored in real time. In the case of this "upgassing trial" the value registered before any upgassing operation started was 0,079 ml/100g.

2.3.2.2 Upgassing Procedure and Results

An hydrogen level between 0.300 and 0.400 ml/100g was set as the goal at which the upgassing process would be considered efficient.

The end of the graphite lance that terminated with the un-covered steel tube was connected to a double connector equipped with valves. This connector allowed to change the type of gas that flowed into the lance by opening and closing the valves, allowing for a fast and safe control over the inlet. The two extremities of the double connector were attached to an argon gas tank and an hydrogen gas tank respectively (Figure 27). Both gases passed through a floating ball flow meter (Figure 28) that monitored the amount of gas flowing through the tubes.

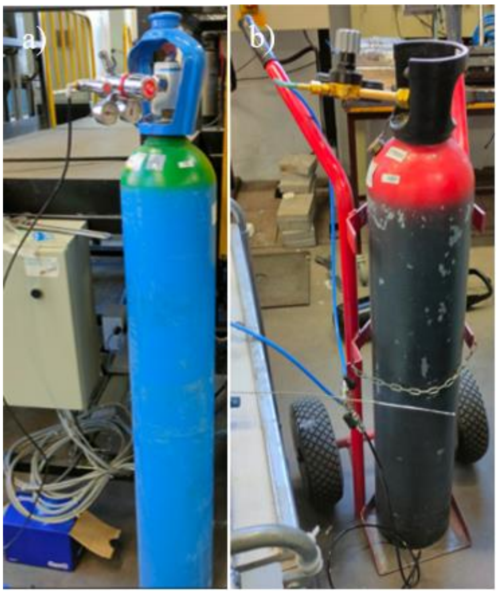

Figure 27: Gas tanks for degassing and upgassing operations. a) Argon tank, b) hydrogen tank

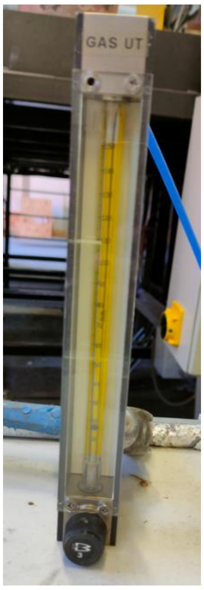

Figure 28: Flow meter

When upgassing was about to start, the argon valve was opened at a flow of 0,4 standard liters per minute (slpm) and the lance lowered between the crucible and the furnace's resistance heaters in order to preheat it for a total of 7 minutes. Then, with argon still flowing through the nozzle, the tip was carefully lowered into the melt and set around 4 cm from the bottom of the crucible. Only when this operation was completed the argon valve was closed and the hydrogen valve opened. The flow of hydrogen was set to 0,053 slpm and a timer for 90 minutes started. When the timer rang the process stopped, the lance was extracted and the level of hydrogen assessed through the HYCAL.

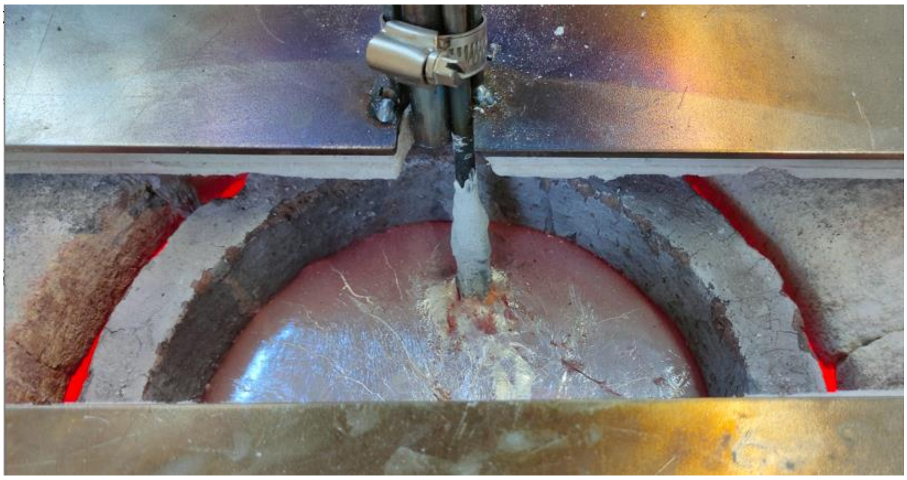

Figure 30: View of the lance lowered into the melt.

Figure 29: Graphite lance mounted on refractory cover and connected to gas inlet

Unfortunately, the amount of dissolved hydrogen measured at 0,160 ml/100g, around two times the starting value but still too low with respect to the objective. For this reason the upgassing technique had to be changed and, in the end, switched to the addition of FOSECO Dycastal 41 upgassing tablets. This option later revealed to be much more efficient in increasing the hydrogen level of the melt over 0.300 ml/100g. A possible reason why direct hydrogen insufflation did not work properly might be an inadequate size of the bubbles expelled by the graphite nozzle, a variable which is strictly correlated to the porosity of the material. Unfortunately, no other qualities of porous graphite were available at the time of the experiment.

2.3.3 First Melt: ILL

The first condition to be examined was the 100% ingot melt with low hydrogen level and no pouring operations. The nomenclature for this particular melt was therefore ILL (I = Ingot, L = Low Oxides, L = Low Hydrogen). Note that the "low oxide" lable refers to the pouring-indouced oxides in the case of poured melts. It does not mean that the melt is completely free from oxide impurities.

Melt ILL was prepared according to the steps described in §2.3.2.1, with the only difference that the ingots were preheated in another Nabotherm furnace at 500°C overnight. This was meant to fasten the process of melting the next day and to remove any surface moisture that could increase the hydrogen level of the melt.

When the alloy reached the liquid state, the hydrogen was measured at 0.101 ml/100g and the degassing process started (0,4 splm, 25 minutes). Degassing was in all similar to the upgassing procedure, but no switching of gases was operated: argon flowed through the nozzle from the preheating step all the way to the end of degassing (extraction of the lance from the melt), and the hydrogen valve was left closed all the time. In summary, degassing was operated by argon insufflation through the graphite lance.

Degassing has 2 different effects on the melt:

- Hydrogen reduction
- Cleaning action: this effect has been often observed in degassing operations that do not use nitrogen gas [67,117,125,126] and carefully tune the rotational speed of the impeller [127] (in case of rotary degassing). The mechanism behind it could be explaned as follows: when argon bubbles float from the bottom of the melt to the surface due to their bouyancy, they "catch" bifilms along the way, making them adhere to the surface of the bubble and floating them to the surface.

Because of the cleaning effect of degassing, whenever the melt was degassed it was assumed that the number of bifilms also decreased.

When the degassing process finished the level of hydrogen measured by the HYCAL was 0,090 ml/100g (around 10% lower than sthe stating amount). At this point the sampling process could start. Each RPT sample was collected at 702 ± 2°C following these steps:

1) When temperature was reached, the surface of the melt was skimmed to remove the oxide layer;
2) The RPT cup was slowly immersed “head first” into the melt, to avoid any turbulence and press the surface oxide on the walls of the cup. As soon as the cup was completely immersed, it was rotated and extracted;
3) The RPT cup was placed in the RPT machine (Vacuum Density Tester 3VT CT by GMBH) and a vacuum of 80 mbar was applied for 6 minutes while the melt solidified.

Figure 31: Immersion of the RPT cup "head first" in order to gently push the oxides to the walls of the cup and avoid turbulence

After 6 RPT samples were obtained, one more cup was filled with molten aluminum and left to solidify at atmospheric pressure. This sample was needed for the density index assesment.

Note that, for all the 6 melts conditions, hydrogen measuring with the HYCAL continued during all the RPT sampling process, in order to have the precise hydrogen level at every new sample.

At this point, a spoon was sprayed with a graphite coating spray and left to preheat inside the furnace while the temeperature of the melt raised to 720°C. In the meantime, the tensile test bar steel die was left to preheat at 250°C inside a Nabertherm® oven.

When the melt reached 720°C tensile test bars’ casting started, according to this procedure:

1) The melt's surface was skimmed;
2) Molten metal was collected using the graphite coated spoon and rapidly cast into the preheated die. While the melt solidified, the spoon was put back in the furnace in order to preheat it again.
3) The die was opened and the tensile test bar casting extracted, so that the process could start again.

The casting process continued until the crucible run out of around ¾ of the available melt, with the idea that for the sample's analysis step only the 12 best tensile test bars would be selected.

The mould used for tensile test bar casting was a standard Sthal Mold design, shown in Figure 32 on the left, while the right image shows an example of a tensile test bar casting obtained from such mold. The Stahl model consists of a rudimental straight pouring basin, straight sprue with square geometry, 4-gate system and a raiser for each tensile test bar. Each casting yielded 2 tensile test bars.

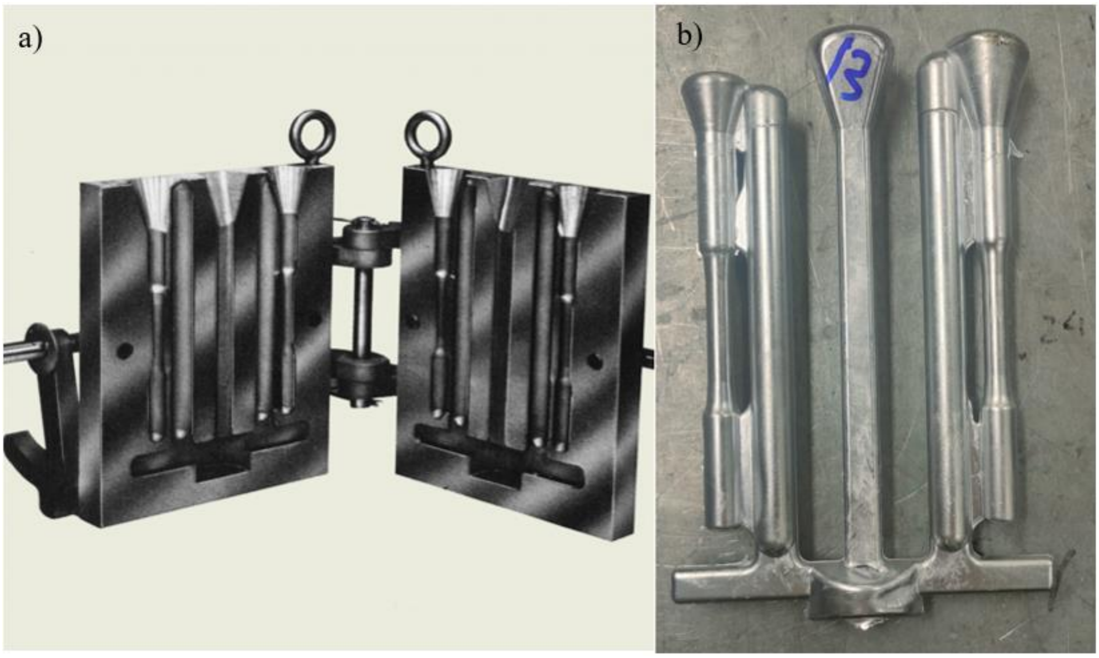

Figure 32: a) example of Sthal Mold design for tensile test bars casting, in all similar to the one used in the experiment. b) example of casting obtained from the Sthal Model once the melt solidified.

The dimensions of the tensile test bars were: L = 130 mm (overall length), L_S = 55 mm (distance between shoulders), L_0 = 35 mm (reduced section), D = 12 mm (width of the grip section), D_0 = 8,4 mm (width).

The first three castings were always discarded.

2.3.4 Second melt: ILH

The second condition to be examined was the 100% ingot melt with high hydrogen level and no pouring operations. The nomenclature for this particular melt was therefore ILH (I = Ingot, L = Low Oxides, H = High Hydrogen).

Melt ILH was prepared according to the steps described in §2.3.2.1, without any preheating of the ingots.

When the alloy reached the liquid state, the hydrogen was measured at 0.108 ml/100g. At this point, the melt's surface was skimmed and upgassing was carried out using $\frac{5}{12}$ of a tablet of FOSECO Dycastal 41. The tablet was manually kept at the bottom of the melt with the aid of a pair of metal tongs and added little-by-little in order to minimize the bubbling effect, which, if excessive, could have resulted in surface turbulence. The amount of tablet added each time was: $\frac{1}{8}, \frac{1}{8}, \frac{1}{6}$. When the upgassing process finished the level of hydrogen measured by the HYCAL was 0.323 ml/100g.

As hinted, the upgassing procedure induced some bubbling, a feature that could have led to the increase in the number of bifilms present in the melt. For this reason, after upgassing, the melt was subjected to a brief degassing treatment with the graphite lance (0,4 splm, 10 minutes) for it to benefit form its "cleaning" effect. This was aimed to reduce the difference in the number of oxides between degassed and upgassed melts. After degassing hydrogen was again measured at 0,305 ml/100g.

RPT samples were collected in the same way described in §2.3.3, as well as the tensile test bars.

2.3.5 Third melt: SLL

The third condition to be examined was the 100% scrap melt with low hydrogen level and no pouring operations. The nomenclature for this particular melt was therefore SLL (S = Scrap, L = Low Oxides, L = Low Hydrogen). Note that "low oxide" lable refers to the pouring-indouced oxides of "IH" melts. It does not mean that the melt is completely free from (old) oxides, which in melts SL should likely be present.

Melt SLL was prepared according to the steps described in §2.3.2.1, with the only difference that instead of ingots the raw material consisted in 100% scrap ingots coming from previously melted and re-solidified ingots. The scrap was preheated in another Nabotherm furnace at 500°C overnight.

When the scrap reached the liquid state, the hydrogen was measured at 0.113 ml/100g and the degassing process started (0,4 splm, 25 minutes). After degassing the hydrogen was measured to be at 0.065 ml/100g.

RPT samples were collected in the same way described in §2.3.3, as well as the tensile test bars.

2.3.6 Fourth melt: SLH

The fourth condition to be examined was the 100% scrap melt with high hydrogen level and no pouring operations. The nomenclature for this particular melt was therefore SLH (S = Scrap, L = Low Oxides, H = High Hydrogen).

Melt SLH was prepared according to the steps described in §2.3.2.1, with the only difference that instead of ingots the raw material consisted in 100% scrap ingots coming from previously melted and re-solidified ingots. The scrap was added in the crucible while at room temperature, without any preheating.

When the scrap reached the liquid state, the hydrogen was measured at 0.196 ml/100g. At this point, the melt's surface was skimmed and upgassing was carried out using $\frac{1}{4}$ of a tablet of FOSECO Dycastal 41 (in the same manner as for melt ILH), and the hydrogen level measured at 0,356 ml/100g.

Following upgassing, the "cleaning" degassing treatment was performed (0,4 splm, 10 minutes) and the final hydrogen level was measured to be 0,326 ml/100g

RPT samples were collected in the same way described in §2.3.3, as well as the tensile test bars.

2.3.7 Fifth melt: IHL

The fifth condition to be examined was the 100% ingot melt with low hydrogen level and pouring operations. The nomenclature for this particular melt was therefore IHL (I = Ingot, H = High Oxides, L = Low Hydrogen).

Melt IHL was prepared according to the steps described in §2.3.2.1, using 100% ingots preheated to 500°C.

When the alloy reached the liquid state, the hydrogen was measured at 0.120 ml/100g, and the degassing process started (0,4 splm, 25 minutes). After degassing the hydrogen was measured to be at 0.065 ml/100g.

As required by the conditions of melt IHL, “new” oxides had to be introduced into the melt by means of pouring operations. These pourings had to simulate the same kind of damage that is inflicted on foundry aluminum alloys during handling. The pouring height was chosen to be 20 times the critical height of aluminum (see §1.6.2), so 25 cm. A metal spoon was coated in graphite spray and preheated. Then, after the surface of the melt was skimmed, the spoon was filled with molten metal, brought at pouring height and emptied into the crucible. This operation was repeated a total of 10 times (Figure 33).

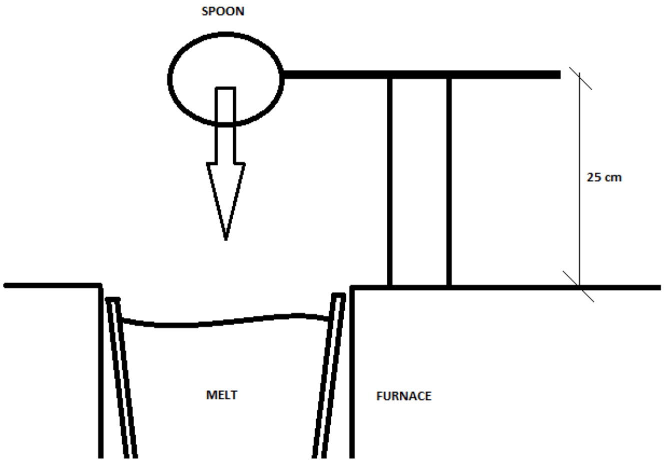

Figure 33: Introduction of "new" oxides in the melt by means of pouring operations. The spoon rests on a 25 cm high support.

The pouring step caused a drop in temperature of 38°C (from 705°C to 667°C), and an increase in hydrogen to 0,170 ml/100g. Because of this, after the sampling temperature was reached again, another degassing step (0,4 splm, 25 min) was necessary in order to reduce the H level to under 0,100 ml/100g. After this second degassing the hydrogen was measured at 0,056 ml/100g.

Note that degassing came with its cleaning effect, so it is possible that some of the newly introduced bifilms were removed, but was nonetheless a necessary measure. In order to avoid having a melt too close in quality to the clean ingot ones (IL) due to this cleaning effect, a new sampling method was adopted: after the surface of the melt was skimmed, instead of immersing the cup as described in §2.2.2, some melt was scooped out of the crucible with a gaphite-coated spoon (preheated) and directly poured into the RPT cup from an height of 12,5 cm (i.e. 10 times the critical height of aluminum). This was done with the intent of re-introducing as many pouring-induced oxides as possible, and at the cost of changing the sampling procedure.

2.3.8 Sixth melt: IHH

The sixth and last condition to be examined was the 100% ingot melt with high hydrogen level and pouring operations. The nomenclature for this particular melt was therefore IHH (I = Ingot, H = High Oxides, H = High Hydrogen).

Melt IHH was prepared according to the steps described in §2.3.2.1, using 100% ingots without any preheating.

When the alloy reached the liquid state, the hydrogen was measured at 0.048 ml/100g. At this point, the melt's surface was skimmed and upgassing was carried out using $\frac{1}{3}$ of a tablet of FOSECO Dycastal 41 (in the same manner as for melt ILH), and the hydrogen level measured at 0,457 ml/100g.

After upgassing, 10 pourings were performed in the same manner as described for melt IHL, followed by a degassing operation (0,4 splm, 25 min) that was performed in order to ensure the closest possible conditions between IHH and IHL (that had to be degassed due to the high H level). The final hydrogen level measured was 0,348 ml/100g.

To keep the "IH" melts (i.e. those derived from ingots and damaged by pouring operations) as similar as possible, the same RPT sampling procedure described for melt IHL was adopted.

At the end of the sampling step, a total of 36 RPT samples, 6 atm-pressure solidified samples and around 100 tensile test bars were collected (i.e. 50 castings)

2.4 Experimental Procedure: Sample Analysis

After the sampling process was finished and all samples were collected, the analysis phase followed. This step consisted in four different analysis procedures:

1) Density Index assessment
2) RPT samples preparation and image analysis
3) Tensile test bars preparation and analysis

4) SEM and EDS analysis of fracture surfaces

2.4.1 Density Index Assessment

The Density Index (DI) is a characteristic number for the melt quality of an aluminum sample. The DI gives and idea of how much the vacuum solidified sample is lighter than the one solidified at atmospheric pressure, so its an indirect indicator of the amount of porosity. The DI is calculated using the following equation:

$$DI = \left(\frac{\rho_{atm} - \rho_{80mbar}}{\rho_{atm}}\right) \times 100 \qquad (2.4)$$

Where ρ_{atm} is the density of a reference sample of melt solidified at atmospheric pressure and ρ_{80mbar} is the density of the sample solidified at 80 mbar of pressure.

The reference sample was chosen according to the following criterion: density for all six of the samples solidified at atm pressure was calculated → the sample that presented the highest density became the reference sample. According to this critera, sample IHH_{atm} (ρ_{atm} = 2,585 g/cm^3) became the reference sample for all 6 melt conditions.

The density of the samples was assessed using the Archimede's principle, according to equation 2.5:

$$\rho = \frac{m_{sample,air}}{m_{sample,water}} \times \rho_{water} \qquad (2.5)$$

Where $m_{sample,air}$ is the mass of the sample, $m_{RPT,water}$ is the mass of the sample weighted in water, and ρ_{water} is the density of distilled water at 20°C (i.e. 0,99823 g/cm^3).

As already hinted in §1.5.3, the DI could also be calculated using the nominal density of the alloy in place of ρ_{atm}. The nominal density can be computed starting from the chemical composition, and will always be higher than the density of the sample solidified at atmospehric pressure, due to the inevitable presence of porosity. The use of the nominal density in the DI assessment allows for a comparison of porosity oriented between the ideal case without any porosity and the real case solidified under vacuum, while the use of ρ_{atm} results in a comparison between two real cases that focuses on the effect of the solidification under vacuum with respect to the solidification at atmospheric pressure.

Figure 34 shows the setup used to weight the samples in water.

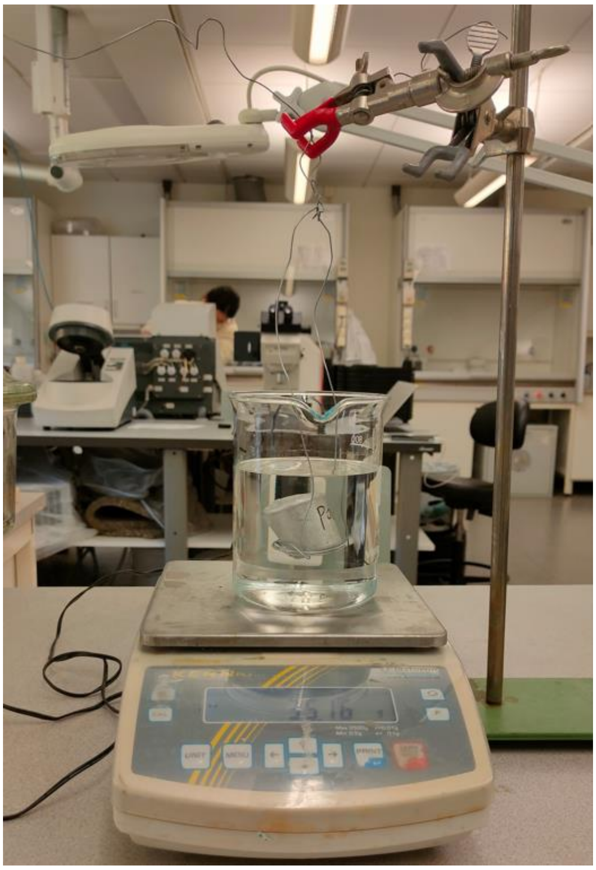

Figure 34: Setup to measure the weight of the samples in water. The sample is kept suspended in water with some steel wire.

2.4.2 Bifilm Index Assessment

First, samples were cut along their axis with a circular silicon carbide blade. One of the two halves was ground using sand papers that went up to 1000 grit (note that this grit was finer than the 800 grit used in the trials discussed in §2.2.2). Then, the surface of the ground half was scanned using the stitching option of an Olympus DSX 1000 optical microscope at 3x zoom. The microscope provided images at 4440 dpi resolution.

The images were then processed with the ImageJ software according to the procedure described in §2.2.2, in order to compute the number of pores, the area and perimeter of the pores and the maximum Feret diameter of the pores. The LDL was set at 200000 μm^2.

The maximum Feret diameter of a geometrical shape (pore in this case) is described as the longest distance between any two points along the selection boundary, and is also known as maximum caliper [128]. According to this definition, the bifilm index of a sample can be calculated by the software as the sum of the maximum Feret diameters of all the pores:

$$BI = \sum_{i=1}^{n} MaxFeret_i \quad (2.6)$$

By normalizing the BI of each sample with its mass, the SpBI can be calculated according to equation (2.1).

2.4.3 Static Mechanical Properties Assessment

The tensile test bars were separated from the filling system and raisers of the castings with the help of a band saw. After being machined, the bars were tested with a Zwick/Roell Z100 tensile test machine following this procedure:

1) The tensile test bar was carefully clamped in place by enabling the "zero load" option of the machine, in order to minimize any stress induced during this operation. The bars were always clamped with the same orientation, with their upper end (cut from the raisers) on top.
2) A clamp extensometer was set in place with the aid of a metallic plate to ensure the clamps' alignment.
3) The test started and the elastic modulus calculated before it automatically stopped to allow for the extensometer removal.
4) The test resumed and concluded with the sample's fracture.

After fracture, the sample was extracted with care (avoiding any contact with the fracture surface) and marked with the following criteria:

Melt condition (ex. IHH) + sample n° (ex. 6)

During the casting operations it was noticed that some of the tensile test bars presented a clear shrinkage-induced pore at the level of the clamping area (see Figure 36). This porosity was more evident in the earlier castings (when the steel die was supposedly still preheating), but persisted for several pouring cycles and could even reappear after a while in later castings. To further investigate this phenomenon, 6 tensile test bars with shrinkage and 6 without shrinkage were broken for each melt condition, for a total of 12 bars for each melt.

Figure 35: Example of two tensile test bars, one without shrinkage and one with shrinkage

2.4.4 SEM and EDS Analysis

Once the tensile test bars were broken, it was clear that a strong difference existed between the “shrunk” and the “un-shrunk” samples. In order to understand the causes of this difference, SEM (Scanning Electron Microscope) imaging and EDS (Energy Dispersive X-Ray Spectroscopy) chemical analysis were carried out on two different tensile test bars’ fracture surface. The two samples both came from the same melt condition (IHL) in order to assure that the difference observed between the two were directly linked to the “shrinkage” phenomenon and not to other variables.

The machine used in this analysis was provided by FEI, model Quanta FEG (Field Emission Gun) 250, and had two signals:

- SE (Secondary Electrons): more useful to extract information on the roughness and overall morphology of the surface
- BSE (Back Scattered Electrons): used to inspect chemical variations inside the microstructure

The fracture surface was first cut free from the tensile test bar with the use of a circular blade and then cleaned in alcohol for 1 minute, before rinsing it in water. This preparatory step was necessary to clean the surface.

The FEG-SEM beam was operated at 20 kV.

CHAPTER 3

RESULTS AND DISCUSSION

3.1 Density Index and Bifilm Index

3.1.1 Density Index Results

Figure 36 shows the relationship between the different melts' Density Index and their hydrogen level.

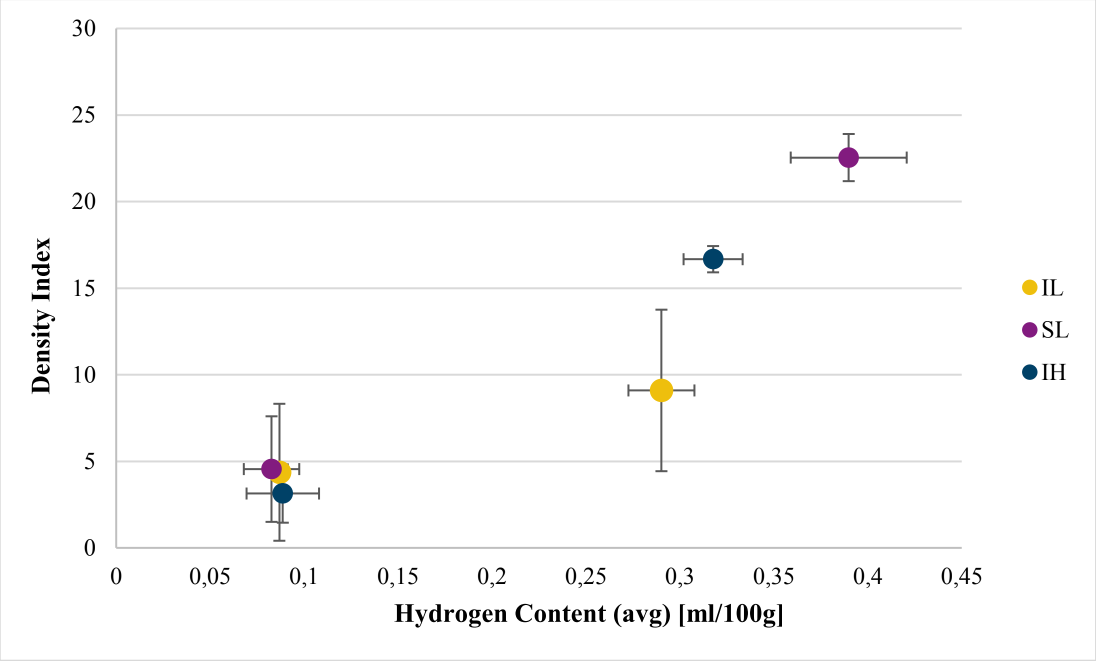

Figure 36: Relationship between melts DI and their hydrogen levels. Low H points refer to melts ILL, SLL and IHL, while high H points to melts ILH, SLH, IHH. See footnote[N] for melt codes.

The legend of this graph should be read as follows: points IL represent melts ILL (low H point) and ILH (high H point), points SL represent melts SLL (low H point) and SLH (high H point), and points IH represent melts IHL (low H point) and IHH (high H point). See footnote[N] for melt codes.

The coordinates of the points were calculated as the average values of the DI and H level of all the samples belonging to the same melt conditions (for example, average

---

[N] **Melt codes: ILL** (100% ingot, low [H]), **ILH** (100% ingot, high [H]), **SLL** (100% scrap, low [H]), **SLH** (100% scrap, high [H]), **IHL** (100% ingot + pouring operations, low [H]), **IHH** (100% ingot + pouring operations, high [H])

value of DI and H level for the 6 RPT samples of melt ILL). It was important to show the average hydrogen level of each melt instead of just reffering to "high" and "low" hydrogen conditions because this value changed considerably between the high-hydrogen melts (i.e. ILH, SLH, IHH). In fact, note that the average hydrogen level of melt ILH was 0,295 ml/100g while for melt SLH this value jumped to 0,389 ml/100g. Nonetheless, it can be clearly seen that the DI increased for all the "high hydrogen" melts (i.e. ILH, SLH, IHH), and that this increase was not the same for each condition. The increase in DI observed for the scrap and poured melts (SL and IH) was more or less comparable, while the one relative to the ingot melt was noticeably smaller. One can also notice the higher distribution of values for melt ILH.

Moreover, the DI of melts ILL, SLL and IHL was essentially the same, which shows how a low hydrogen level in the melt makes it impossible to distinguish between the different conditions (ingot, scrap or poured ingot).

In light of these results, it seems that the hydrogen level has a clear effect on the DI of a melt, and that this effect is correlated to the amount of scrap and damage inflicted to such melt. Additionally, it seems that this effect is comparable in the case of scrap melt and damaged melt, but not for clean ingot melt.

3.1.2 Bifilm Index Results

During the analysis of the specific bifilm index a question arose: are the maximum Ferets of the pores normally distributed? If not, what other pore descriptors are not normally distributed, and what distribution better describes them?

The use of the Minitab® statistical analysis softaware was essential to answer this questions. By providing Minitab with all the data that concerned Ferets, areas and perimeter of pores coming from the RPTs of a same melt condition, it was possible to ask the software to correlate these values to the best-fitting probability distribution, and calculate the parameters of such distribution.

Figure 37 shows the results of this investigation, and demonstrates that the distribution that better fits the maximum ferets of the pores (from which the BI is then calculated) is lognormal.

A set of data is considered to be lognormally distributed if the natural logarithm of such data follows a normal distribution. Thus, if the random variable X is log-normally distributed, then Y = ln(X) has a normal distribution. Lognormal distribution is typical of data whose distribution presents a skewed peek curve with a long tail on one side.

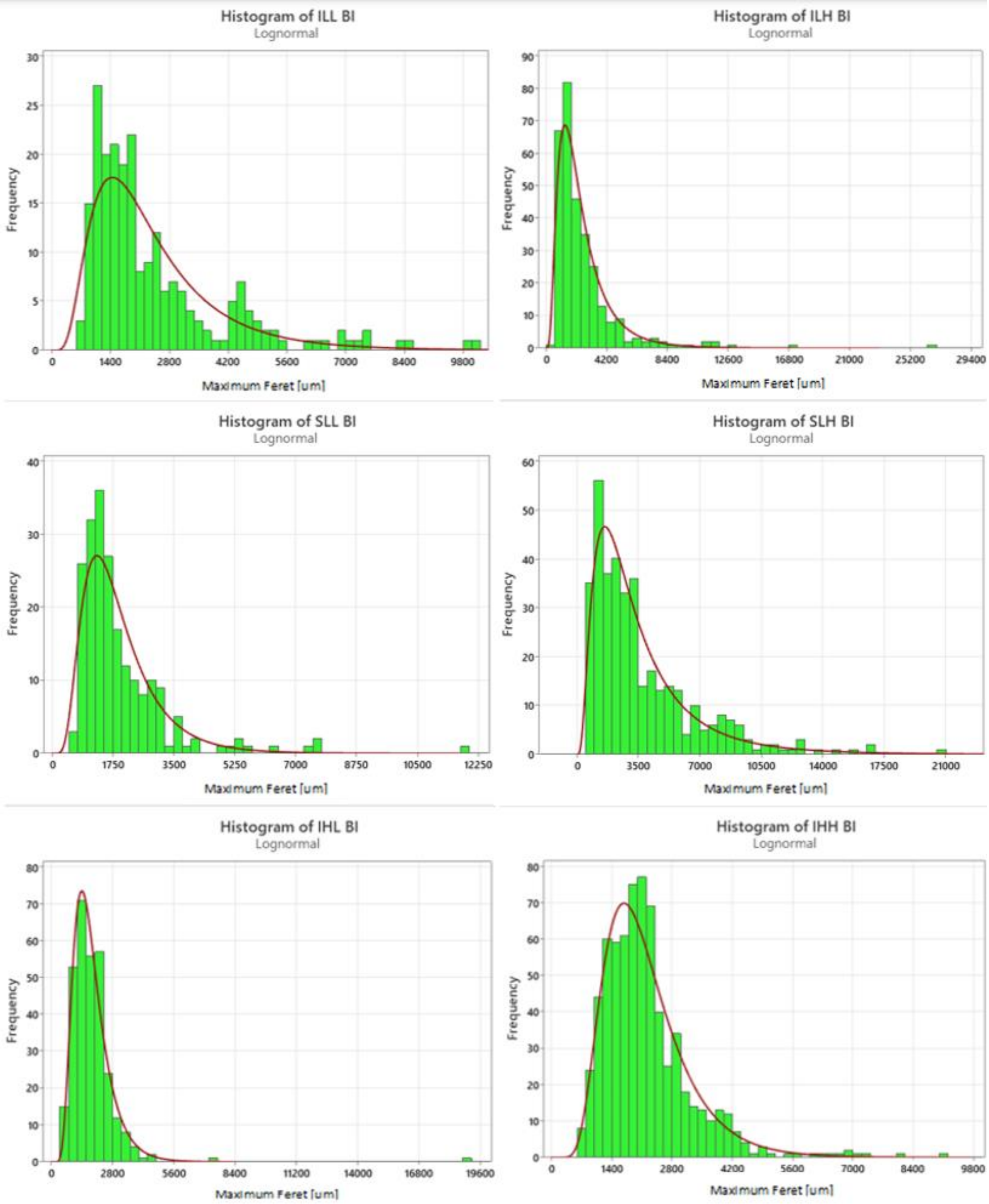

Figure 37: Distribution of the maximum Ferets of the six different melt conditions. The red curve represents the best fitting distribution, in all cases lognormal.

The histograms under the fitting curves are the real distributions of the maximum Ferets of single pores for all the RPT samples belonging to the same melt condition. For example, the bottom right histogram shows the distribution of data collected form the 6 RPT samples of melt IHH.

Lognormal distributions are described by two parameters:

- Location μ: this is the mean of the variable's natural logarithm
- Scale σ: this is the standard deviations of the variable's natural logarithm

Table 6 lists the parameters for each fitting curve (in red) of Figure 37.

A fundamental difference between a normal and a lognormal distribtuion is that, for the latter, the mode, median and mean values do not coincide. These descriptors can be calculated from the location and scale values according to these equations[1]:

$$Mode = \exp(\mu - \sigma^2) \tag{3.1}$$

$$Median = \exp(\mu) \tag{3.2}$$

$$Mean = \exp\left(\mu + \frac{\sigma^2}{2}\right) \tag{3.3}$$

Table 6 lists the parameters for each fitting curve (in red) of Figure 37, and their mode, median and mean values:

LOGNORMAL CURVE PARAMETERS FOR THE MAXIMUM FERET OF PORES					
MELT CONDITION	LOCATION	SCALE	MODE [mm]	MEDIAN [mm]	MEAN [mm]
ILL	7,622	0,5865	1,4	2,0	2,4
ILH	7,617	0,6527	1,3	2,0	2,5
SLL	7,436	0,5191	1,3	1,7	1,9
SLH	7,943	0,7524	1,6	2,8	3,7
IHL	7,430	0,4307	1,4	1,7	1,8
IHH	7,610	0,4236	1,7	2,0	2,2

Table 6: Parameters for the lognormal distribtuion fitting curves and mode, median and mean values

With all this information, we can compare the different fitted distribution curves in order to better understand the changes in the pores' maximum Ferets. Figure 38 superimposes all the distribution curves in one single normalized graph. On the y-axis there is the percent of pores with maximum Feret of x-coordinate size.

---

[1] in all the equations, in case of a 3-parameter lognormal with threshold T, we have to add such value to the results (with appropriate sign).

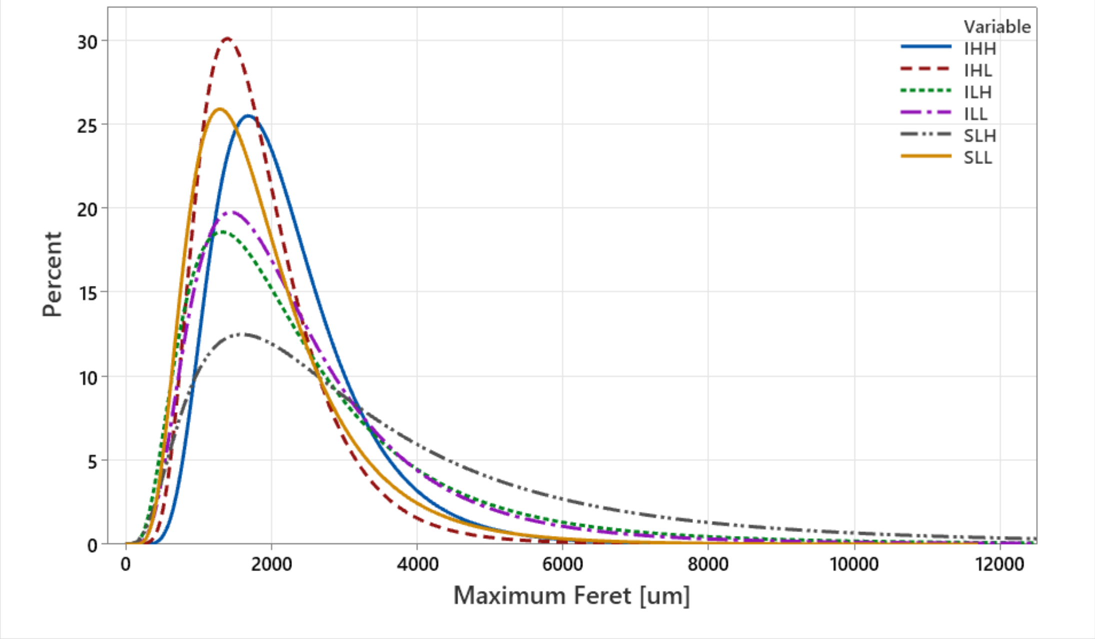

Figure 38: Superimposed distributions of the maximum Ferets of pores for all melt conditions.

One can clearly see that melt SLH is the one that presents the flattest distribution, meaning that the maximum Ferets values were more scattered and shifted towards higher values. Melts ILL and ILH both behave in a very similar manner, while the other melts present higher and more pronounced peaks towards small values (remember that the x-coordinate of the peak corresponds to the mathematical mode of the distribution).

The SpBI was then calculated. The SpBI of each melt became the average of the BI of the six RPT samples collected from that melt, each normalized to the specific sample's weight. Figure 39 shows the relationship between the hydrogen level in the different melt conditions and the resulting SpBI.

The legend of Figure 39 should be read in the same way as described for the density index graph, that is, each pair of points rapresents the low and high hydrogen conditions of a melt type (IL, SL or IH). Note that the specific bifilm indices of the scrap and "poured" melts (lines SL and IH respectively) increased similarly as the hydrogen level increases. On the other hand, the 100% ingot undisturbed melt (points IL) behaves in a very different way, showing only a modest increase in the SpBI at increasing hydrogen level.

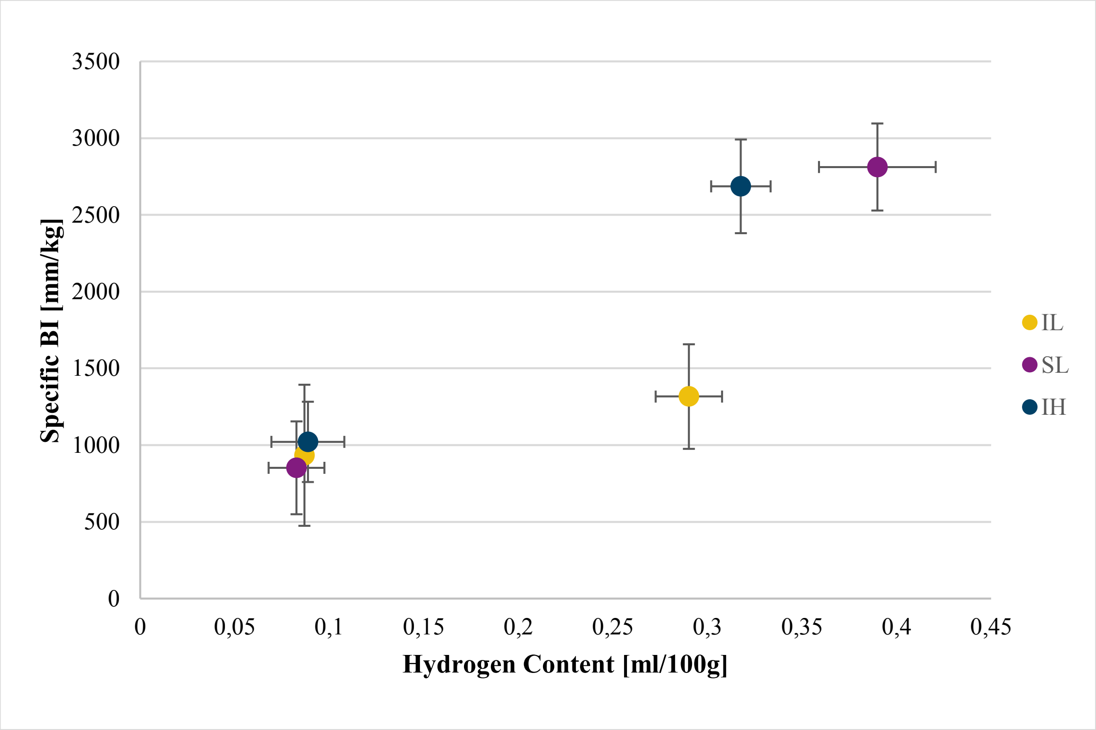

Figure 39: Specific BI vs H for the different melt conditions. Low H points refer to melts ILL, SLL and IHL, while high H points to melts ILH, SLH, IHH. See footnote[N] for melt codes.

Note that Figure 39 resembles the scenario depicted in Figure 18. We could in fact state that melts ILL and ILH correspond to the "clean" melt condition, free from both old and newly indroduced oxides. This is, of course, an abstarction, since we know that a perfectly clean melt free from bifilms would be much harder to obtain (if even possible). On the other hand, melts SLL and SLH correspond to the "dirty" melt condition in which the melt is contaminated by old oxides, while melts IHL and IHH correspond to the "dirty" melt condition in which the melt has been damaged during handling and new oxides are introduced. Much similarly to what was described in §2.1.1, the clean melt's bifilm index was hardly influenced by the amount of hydrogen, and the slight increase registered might aswell be the result of:

- The upgassing procedure that, as previously said, was somewhat turbulent in nature.
- The small amount of oxides inevitably present in this melt.

[N] **Melt codes: ILL** (100% ingot, low [H]), **ILH** (100% ingot, high [H]), **SLL** (100% scrap, low [H]), **SLH** (100% scrap, high [H]), **IHL** (100% ingot + pouring operations, low [H]), **IHH** (100% ingot + pouring operations, high [H])

On the contrary, the dirty melts' bifilm indices visibly increased for higher hydrogen contents.

It can be therefore concluded that at low hydrogen levels (below 0,1 ml/100g) the SpBI of the melts was virtually indistinguishable between conditions, while at high hydrogen levels (over 0,3 ml/100g) the difference between "clean" and "dirty" melts becomes evident by SpBI analysis.

At last, we should adress the effect of the distribution on data interpretation. The BI is unaffected from the lognormal distribution, since it is simply the result of the sum of the maximum Ferets, but by acknowledging the lognormal nature of the distribution we gain acces to two more information: the mode and the median of the maximum Ferets. The mode is defined as the value that appears most often in a set of data values, while the median as the value separating the higher half from the lower half of a data sample [129]. While in a normal distribution these two values coincide with the mean, this is not true for lognormal distributions.

3.1.3 Other Pore Descriptors Results

Apart from the maximum Feret, other pore descriptors are:

- Average pore equivalent diameter(also correlated to percentage of surface porosity);
- Number of pores;
- Average roundess of the pores.

3.1.3.1 Pore Area and % of Surface Porosity

Each pore counted on the sample's surface is characterized by an area, which gives us information on the bidimensional size of the pore. The issue is that the area of pores carries behind a square that tends to also square the error, and therefore, increase the difficulty of data interpretation. For this reason, it is common to refer to the "equivalent diameter" of a pore rather than its area, where the equivalent diameter is computed from the area of the pore through equation 3.4:

$$D_{eq} = \sqrt{\frac{4A_{pore}}{\pi}} \quad (3.4)$$

Therefore, the D_{eq} of the pores was calculated and its distribution studied with the same procedure used for the maximum Feret, which was described in §3.1.2. Results are summarised in Figure 40, and show that much like the maximum Ferets, the equivalent diameters of the pores are lognormally distributed according to a 3-parameter lognormal distribution (with threshold $d_{threshold} = \sqrt{\frac{4LDL}{\pi}} \cong 500\ \mu m$).

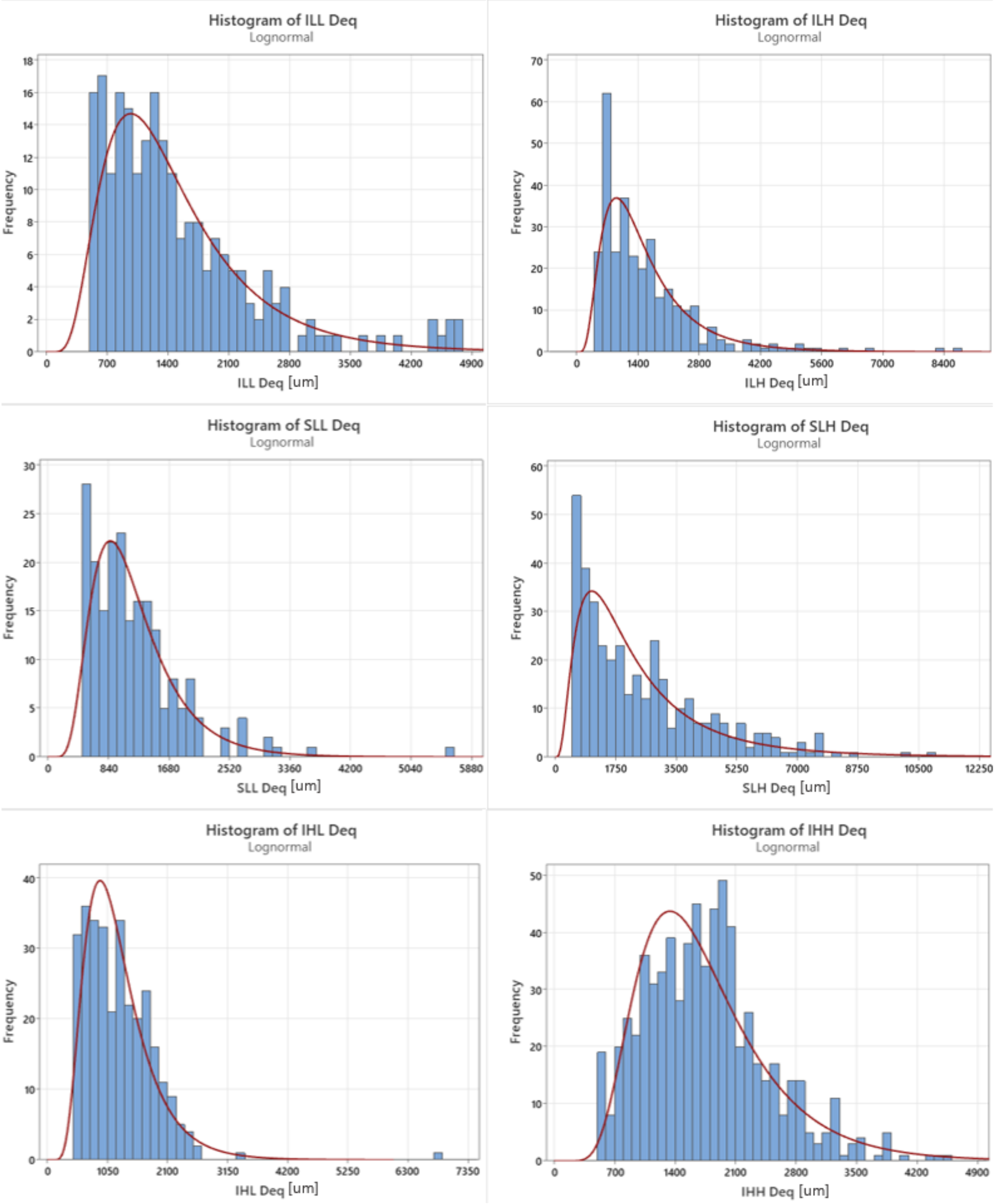

Figure 40: Distribution of the pores' equivalent diameter of the six different melt conditions. The red curve represents the best fitting distribution, in all cases lognormal, defenetly not normal.

In a similar fashion to what done for the maximum Ferets, we can study the parameters of the distribution to compare them. Table 7 shows the mode, median and mean values for the various pore area distributions.

LOGNORMAL CURVE PARAMETERS FOR PORE EQUIVALENT DIAMETER					
MELT CONDITION	**LOCATION**	**SCALE**	**MODE [mm]**	**MEDIAN [mm]**	**MEAN [mm]**
ILL	7,173	0,5374	1,0	1,3	1,5
ILH	7,183	0,606	0,9	1,3	1,6
SLL	6,986	0,4654	0,9	1,1	1,2
SLH	7,552	0,7621	1,1	1,9	2,5
IHL	7,031	0,4509	0,9	1,1	1,2
IHH	7,382	0,4257	1,3	1,6	1,8

Table 7: Parameters for the lognormal distribtuion fitting curves and mode, median and mean values

In a similar fashion to what done for the maximum Ferets, we can now superimpose the distribution curves to compare them. Figure 41 superimposes all the distribution curves in one single normalized graph. On the y-axis there is the percent of pores with equivalent diameter of x-coordinate size.

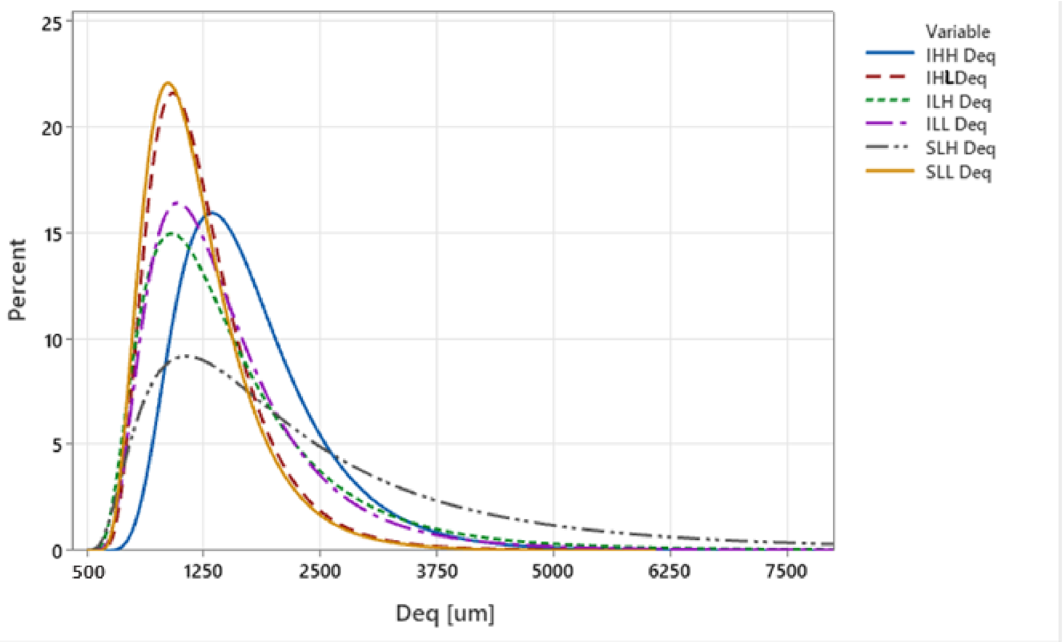

Figure 41: Superimposed distributions of the equivalent diameters of pores for all melt conditions

From Figure 41 we see that melts IHL and SLL behaved in a very similar manner, while melt ILL showed a slightly broader distribution, characterized by an higher mean and median values. On the other hand, melt's ILL distribution is almost indistinguishible from the one of melt ILH, meaning that there was hardly any change in the pores equivalent diameter of melts IL at different hydrogen levels. A slight change can be seen for melts IH, where the mean pore equivalent diameter increases from 1,25 mm to 1,71 mm, but the greatest change is registered in melts SL: at high hydrogen levels, the curve drastically lowers its peak and widens towards higher values. The mean D_{eq} jumps from 1,20 mm (SLL) to 2,54 mm (SLH)

Lastly, the sum of the pore areas gives us the total surface porosity, an information that can be compared to the sample's surface to get the percentage of surface porosity. Figure 42 shows the relationship between hydrogen content and % of surface porosity. Each point's "Pore %" value was calculated as the average percentage of surface porosity of the 6 RPT samples belonging to such hydrogen level. For example, the IL point on the bottom right represents the average % surface porosity of the 6 RPT samples coming from melt condition ILL (ILL1, ILL2, … , ILL6)

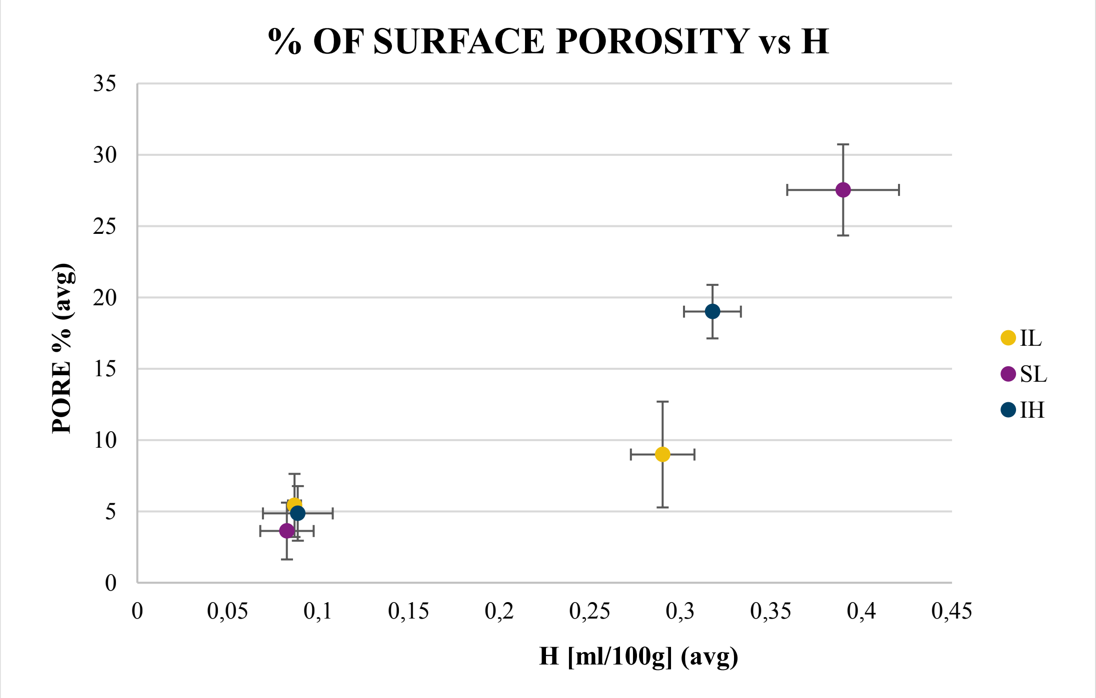

Figure 42: Pore Percentage Average vs H for the different melt conditions. Low H points refer to melts ILL, SLL and IHL, while high H points to melts ILH, SLH, IHH. See footnote[N] for melt codes.

We can clearly see that the biggest increase in percent of surface porosity appeared for the scrap melts (SL), while only a modest increase can be traced back to the clean ingot melts (IL).

[N] **Melt codes: ILL** (100% ingot, low [H]), **ILH** (100% ingot, high [H]), **SLL** (100% scrap, low [H]), **SLH** (100% scrap, high [H]), **IHL** (100% ingot + pouring operations, low [H]), **IHH** (100% ingot + pouring operations, high [H])

3.1.3.2 Number of Pores

The number of pores is an important parameter that allows us to correlate the mean equivalent diameter to the percentage of surface porosity. In fact, if we imagine a situation in which the pore number remains the same between low and high hydrogen levels, a modest increase in the mean pore D_{eq} would result in a modest increase in the % of surface porosity. But, if the number of pores increases for higher hydrogen levels, then modest increase in D_{eq} would result in a greater increase in the % of surface porosity, due to the presence of new additional pores.

According to what stated above, Figure 43 shows that the number of pores doubled at higher H levels for the poured melts (IH), but stayed more or less constant for the clean (IL) and scrap (SL) melts. This also explains why the increase in the SpBI of melts IH was similar to that of melts SL, even if the increase in the D_{eq} for melts IH was defenetly smaller than that of melts SL: a larger number of pores contributed to the SpBI.

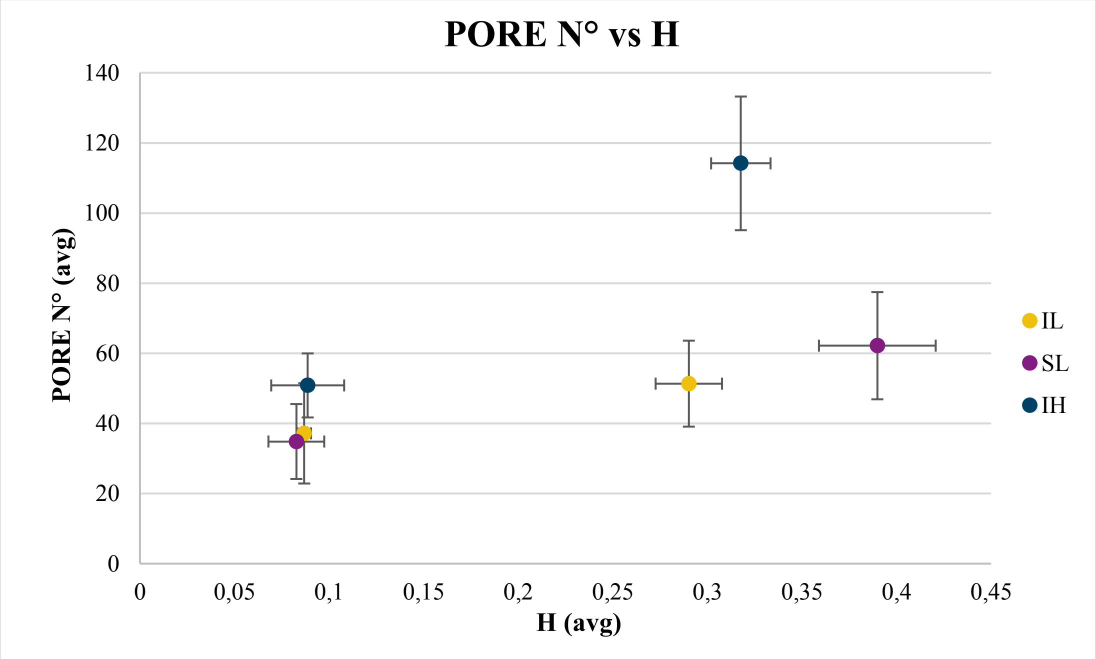

Figure 43: Number of Pores vs H for the different melt conditions. Low H points refer to melts ILL, SLL and IHL, while high H points to melts ILH, SLH, IHH.

Each Pore N° (avg) value was calculated as the average number of pores found on the 6 RPTs of a same melt condition. For example, the IL point on the bottom right represents the average number of pores of the 6 RPT samples coming from melt condition ILL (ILL1, ILL2, … , ILL6).

3.1.3.3 Pore Roundness

Roundness is the measure of how closely the shape of an object approaches that of a mathematically perfect circle [130]. Applied to porosity, roundness gives us information on the shape of the pore.

The roundness of a pore can be mathematically defined as:

$$Round = \frac{P^2}{4\pi A} \quad (3.5)$$

Where P is the perimeter of the pore and A its area.

The closer the roundness is to 1, the closer the shape of the pore is to a prefrect circle, and the higher its value, the lesser the pore resembles a perfect circle, which could be both caused by a jagged profile and/or a skewed shape.

Roundness distribuition was analyzed with the aid of Minitab®, and resulted to be lognormally distributed (see Appendix B for separate distribution charts), so we can compare the distribution curves:

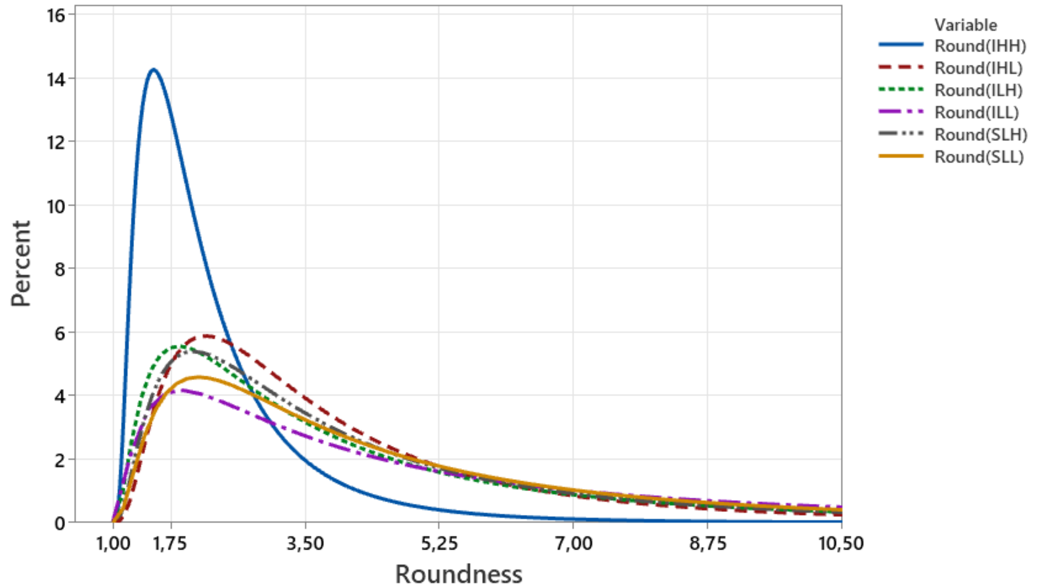

Figure 44: Superimposed distributions of the roundness of pores for all melt conditions. See footnote[N] for melt codes.

Note that the threshold was set to 0,999 in order to include eventual pores with roundness equal to 1 (the minimum possible value).

Table 8 shows the lognormal distribution parameters for all the melts' curves:

[N] **Melt codes: ILL** (100% ingot, low [H]), **ILH** (100% ingot, high [H]), **SLL** (100% scrap, low [H]), **SLH** (100% scrap, high [H]), **IHL** (100% ingot + pouring operations, low [H]), **IHH** (100% ingot + pouring operations, high [H])

LOGNORMAL CURVE PARAMETERS FOR PORES' ROUNDNESS					
MELT CONDITION	LOCATION	SCALE	MODE	MEDIAN	MEAN
ILL	1,172	1,143	1,9	4,2	7,2
ILH	0,864	1,007	1,8	3,4	4,9
SLL	1,056	0,974	2,1	3,9	5,6
SLH	0,900	0,924	2,0	3,5	4,8
IHL	0,846	0,81	2,2	3,3	4,2
IHH	-0,0261	0,778	1,5	2,0	2,3

Table 8: Parameters for the lognormal distribtuion fitting curves plus mode, median and mean values

From comparing Table 8 with Figure 44, one can see that mode, median and mean values of all melt conditions decreased in value for higher hydrogen concentrations. The greatest change in distribution occurred for melt IHH, whose peak appears sharper and taller than in any other case. This also suggests a lower scatter in data.

The decrease in roundness towards 1 for each melt at increased hydrogen levels happens due to the higher amount of gas flowing into the bifilms, inflating them open and reducing their skewness like described in §1.4.2. Anyway, it should be underlined that, if we consider the scatter, the change in roundness for melts SL and IL was so small that it is difficult to address its relevance during data interpretation.

3.2 Static Mechanical Properties

To evaluate and study the static mechanical properties of the melts, the yield strength, ultimate tensile strength and elongation at fracture of the tensile test bars were studied. Anyways, before discussing the results of the mechanical tests an introductory note is imperative: during the tensile tests it clearly resulted that the samples characterized by the shrinkage porosity (see §2.4.3) behaved in a different way than those without it. In particular, this difference strongly emerged in the UTS and e_f (elongation percentage at fracture). For this reason the following paragraph may refer to "s" and "n" class samples, where the "s" class includes all those samples that presented a visible surface shrinkage, while the "n" class all the others (i.e. those without any visible shrinkage).

3.2.1 Yield Strength

The yield strengths measured from the tensile test bars of each melt is shown in Figure 45.

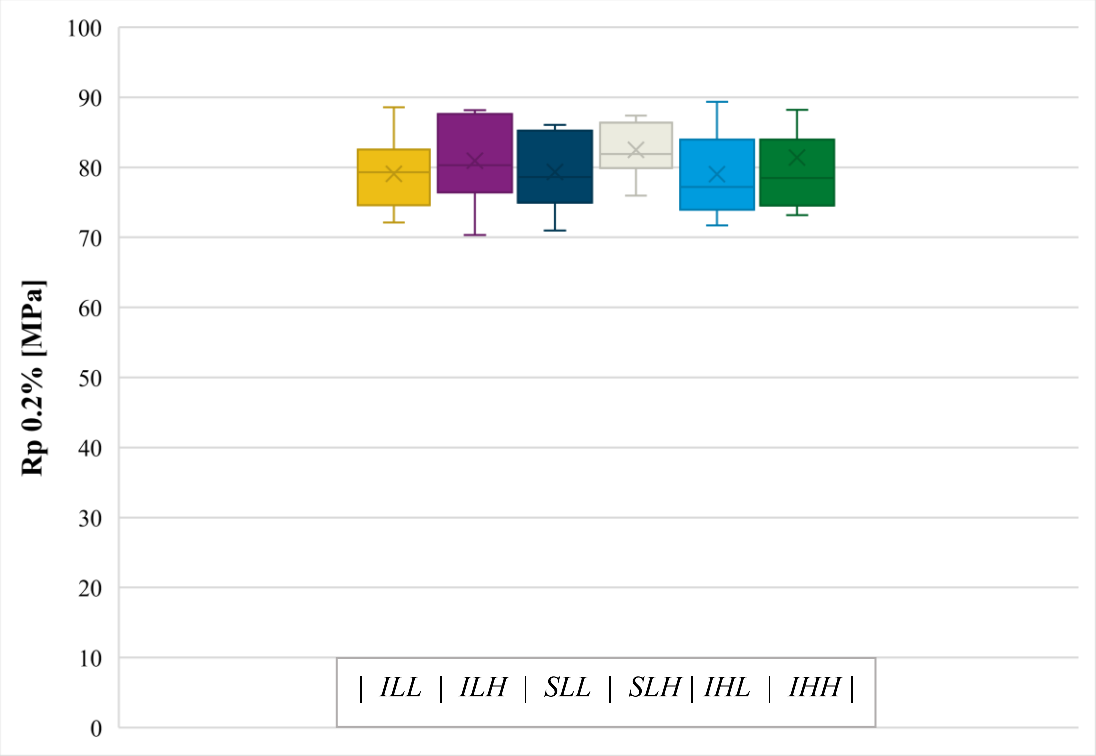

Figure 45: Yield strength of the various melt conditions. See footnote[N] for melt codes.

As one would expect, there was no change in the yield strength between melt conditions, and no appreciable change was observed between shrinked and normal tensile test bars.

The average yield strength between all melt conditions is 80 MPa.

3.2.2 Ultimate Tensile Strength

As previously hinted, the Ultimate Tensile Strenght (UTS) changed remarkably between the samples that presented visible shrinkage on their surface and those who did not. Perhaps more interestingly, this change in the UTS seemed to be a function of this difference only, and indipendent from the change in melt condition. This means that all the samples with surface shrinkage behaved in a similar way, while all the

---

[N] **Melt codes: ILL** (100% ingot, low [H]), **ILH** (100% ingot, high [H]), **SLL** (100% scrap, low [H]), **SLH** (100% scrap, high [H]), **IHL** (100% ingot + pouring operations, low [H]), **IHH** (100% ingot + pouring operations, high [H])

others in a different one (but similar between each other), indipendently from the type of melt (Figure 46).

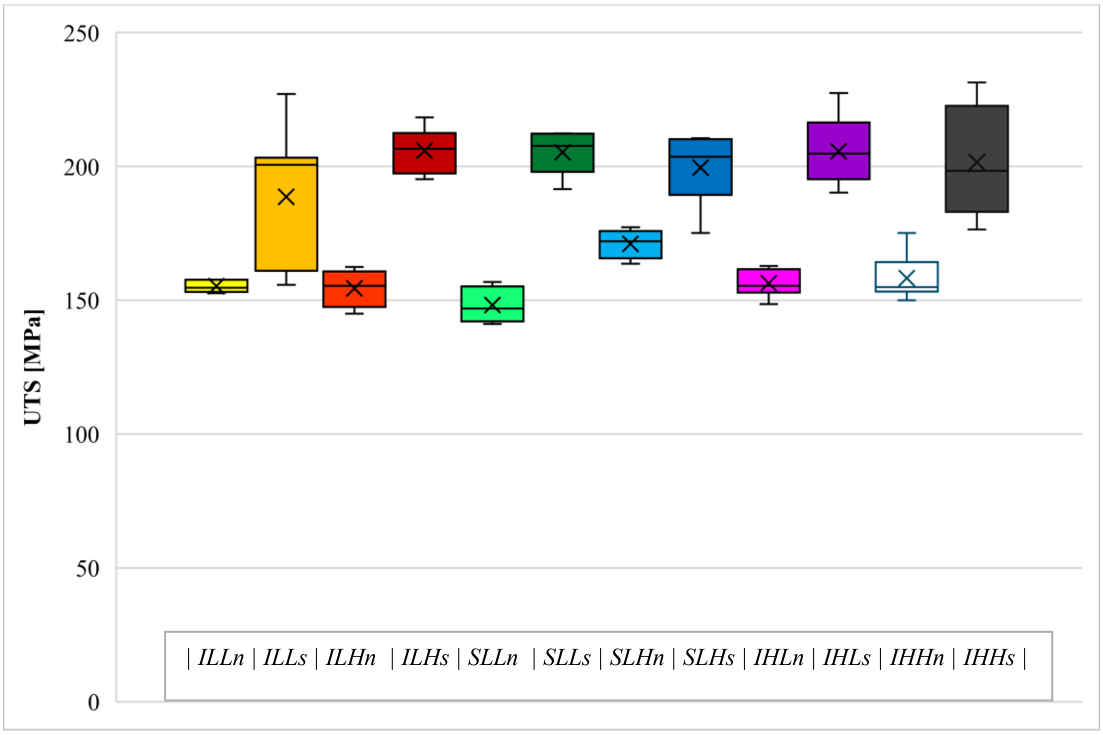

Figure 46: UTS of the various melt conditions with shrinkage vs non-shrinkage distinction. Note that the letter "n" indicates "non-shrinkage" samples, while letter "s" indicates "shrinkage" samples.

The large amount of data in Figure 46 may be hard to process at first glance, so let us discuss it in more detail. In the graph, each melt condition is represented by two boxes, one relative to samples of "n" class and one to samples of "s" class deriving from said melt. For example, the first two boxes (light and dark yellow) are relative to conditions ILLn and ILLs: ILLn are the 6 tensile test bars collected from melt ILL that presented no shrinkage on their surface, while ILLs refers to the 6 tensile test bars of the same melt that did present shrinkage on their surface. The same goes for melts ILH, SLL, SLH, IHL and IHH.

With this in mind, it emerges that in all cases the samples that presented surface shrinkage showed greater UTS with respect to those without it. This difference is stronger in melts ILH, SLL and IHL, while it gets somewhat weaker for melt ILL.

The average UTS of "n" class samples (without surface shrinkage) is 157 MPa, while the average UTS of "s" class samples (with surface shrinkage) is 201 MPa.

On the other hand, it is almost impossible to find any change in the UTS between samples of the same class ("s" or "n") when changing melt conditions.

Appendix B shows a box chart of the UTS of the melts without any distinction between ”n” and ”s” classes.

3.2.3 Elongation (%) at Fracture

What said above for the UTS could be repeated for the percentage of elongation at fracture (e_f). Figure 47 shows the e_f for all the different melts, subdividing each condition in “n” and “s” classes.

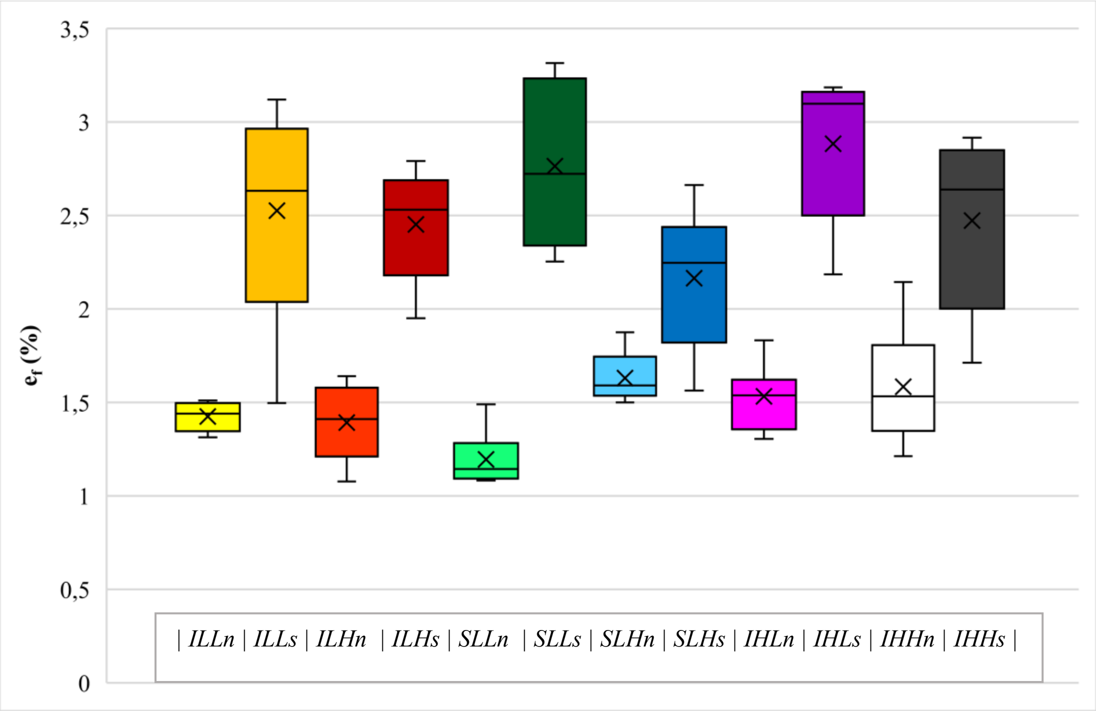

Figure 47: Percentage elongation at fracture of the various melt conditions with shrinkage vs non-shrinkage distinction. Note that the letter ”n” indicates ”non-shrinkage” samples, while letter ”s” indicates ”shrinkage” samples. See footnote[N] for melt codes

Note that, in contrast with the UTS, data appear to be more scattered. Still, samples exhibiting surface shrinkage (”s” class) performed visibly better than their un-shrunk counterpart (”n” class). For some melt conditions, like SLL, this difference is more evident than for others,like SLH, but the discrepancy is again confirmed by the average values: the average e_f of ”s” class samples is 2,5% while that of ”n” class samples 1,4%, more than 1% lower.

Table 9 sums up what stated above and adds more information on classes ”s” and ”n”.

[N] **Melt codes: ILL** (100% ingot, low [H]), **ILH** (100% ingot, high [H]), **SLL** (100% scrap, low [H]), **SLH** (100% scrap, high [H]), **IHL** (100% ingot + pouring operations, low [H]), **IHH** (100% ingot + pouring operations, high [H])

COMPARISON BETWEEN ”S” AND ”N” CLASS TENSILE TEST SAMPLES				
CLASS	UTS (avg)	% > 180 MPa	e_f (avg)	% > 2%
s	201 MPa	86,1	2,5 %	82,8
n	157 MPa	5,5	1,4 %	2,8

Table 9: Average UTS and elongation at fracture, % of samples with UTS > 180 MPa and % of samples with elongation at fracture > 2% for ”s” and ”n” class tensile test samples.

Table 9 not only confirms that on average the UTS and elongation at fracture of ”s” class samples is greater, but also that only a very small amount of ”n” class samples showed UTS > 180 MPa and/or $e_f > 2\%$.

Appendix B shows a box chart of the e_f of the melts without any distinction between ”n” and ”s” classes.

Appendix C shows the raw mechanical data collected from the tensile tests of the 36 samples.

3.3 SEM and EDS Analysis

The peculiar difference in properties between “n” and “s” class tensile test samples required a deeper investigation. Therefore, two broken tensile test samples were selected and their fracture surface analyzied via Scanning Electron Microscopy (SEM) and Energy Dispersive X-Ray Spectroscopy (EDS). The two samples both came from melt IHL, one presenting no evident shrinkage on the bars’ surface (sample code: IHL6) and one having a deep shrinkage depression at the level of the clamping area (sample code: IHL11). Their elongation at fracture was 1,3% and 3,1% respectively, so considerably different, while their UTS was 148 MPa and 205 MPa respectively.

Figure 48 resumes some of the details collected from the fracture surface of sample IHL6:

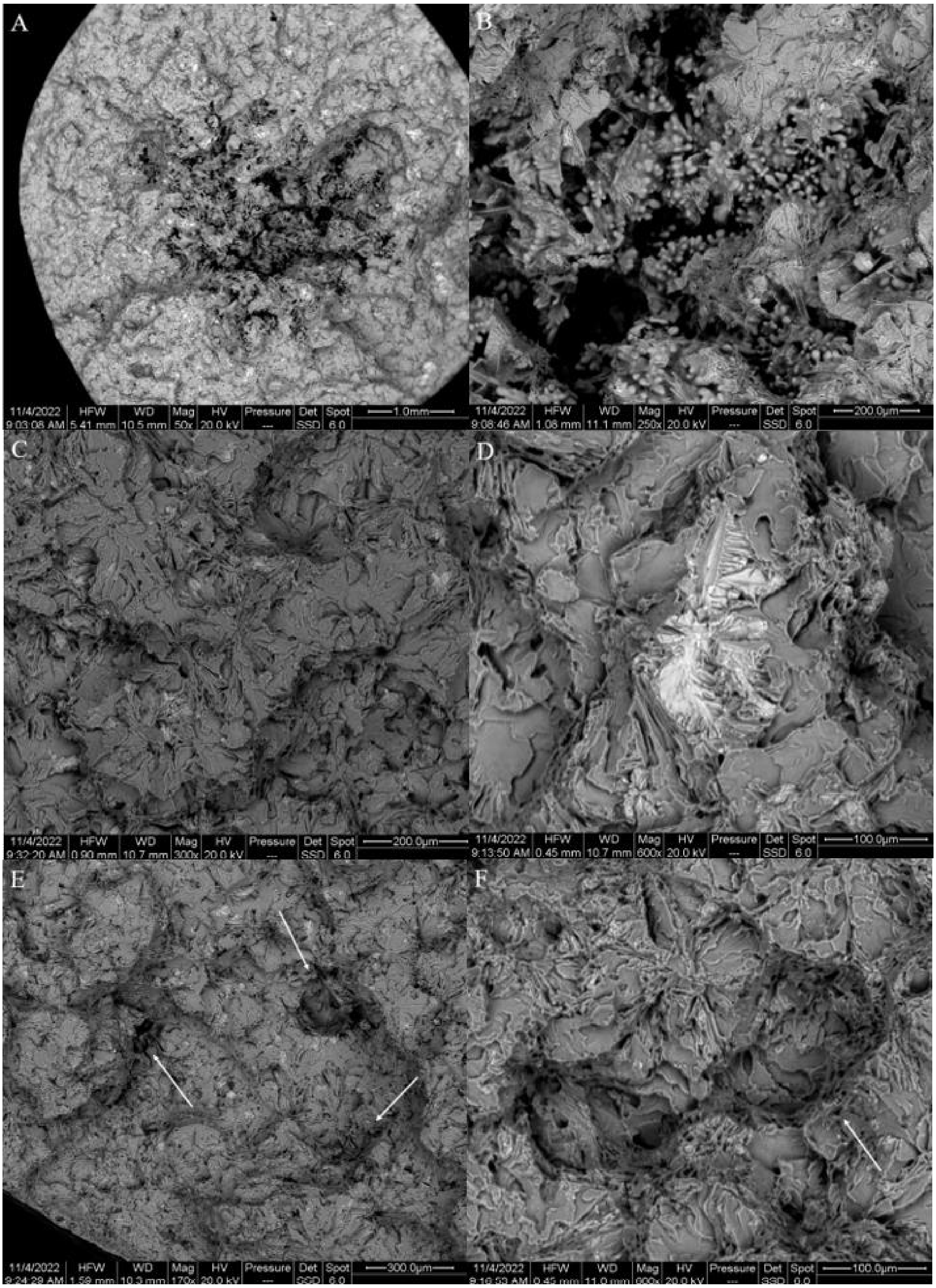

Figure 48:Fracture surface SEM images from sample IHL6. A (50x BSE) and B (250x, BSE): big shrinkage porosity at the center of fracture surface; C (300x, BSE): defect-free area; D (600x, BSE): big intermetallic particle; E (170x, BSE) and F (600x, BSE): oxides

We can now analyze the different frames of Figure 48:

- Frames A and B: they reveal the presence of a big shrinkage porosity at the center of the sample's section. It measures more than 3 mm in diameter and dendrites can be seen protruding into the pore. The EDS suggests that the shrinkage porosity is oxidated in some regions (Figure 49 A). The lamellae that are seen protruding from the dendrites in frame B are made of silicon, an element that is highly present in this alloy.
- Frame C: Magnification of a defect-free area. The interesting thing to notice is that the fracture surface doesn't show any dimples, suggesting a fragile fracture similar to that of a ceramic material. This explains the very low value of elongation at fracture of this sample (1,3%). The little white dots that appear in this image are intermetallic particles of the same nature of the one depicted in frame D. the EDS analysis of this area can be found in Figure 49 B.
- Frame D: Example of one of the big intermetallics observed on the fracture surface. These intermetallics are rich in Fe, Mn and Cr (EDS in Figure 49 C), and could grow to over 150 microns in length. The remarkable size of these particles implies that they had enough time to nucleate and grow by depleting the surrounding melt of its alloying elements. These intermetallics are known to be fragile and detrimental for the mechanical properties of the cast alloy.
- Frames E and F: Examples of oxides seen on the fracture surface, at different magnifications. They could be spotted by BSE imaging due to their darker tone with respect to the matrix, and were scattered all over the fracture surface.

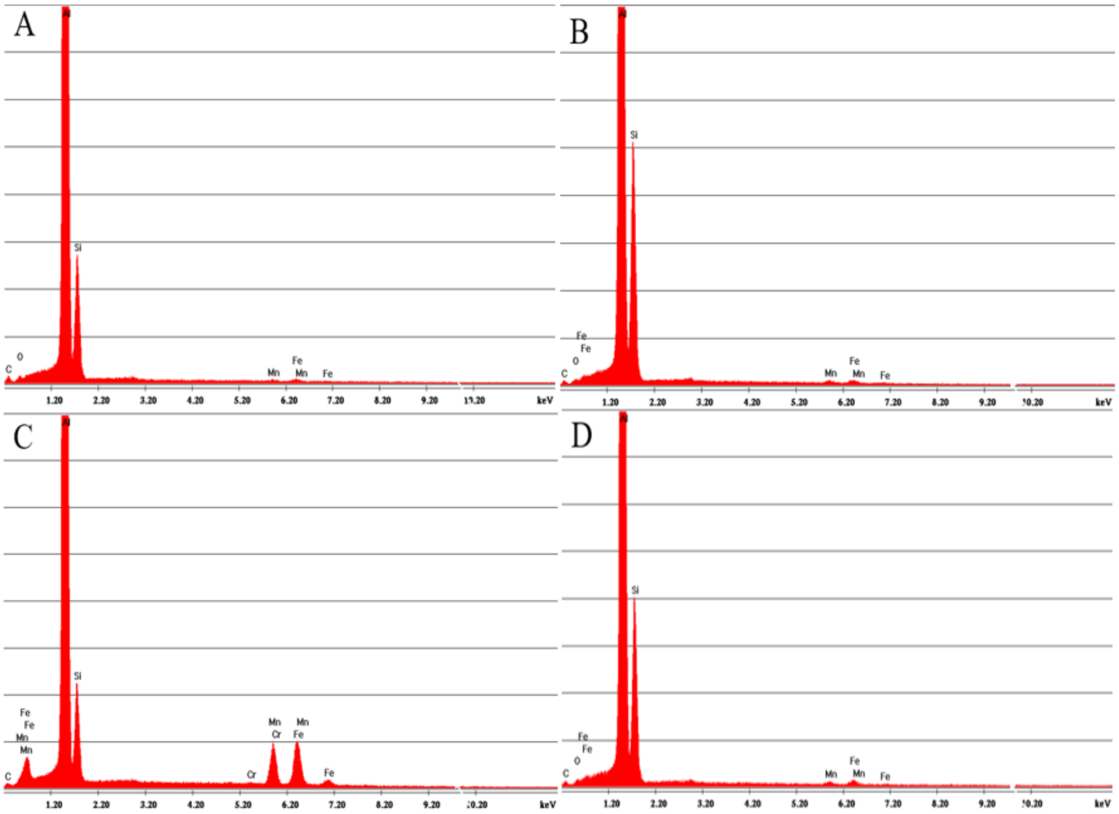

Figure 49: EDS of sample IHL6 fracture surface's regions. A: Central porosity; B: Area free from defects (i.e. matrix); C: Intermetallic particle; D: oxide

Figure 50, on the other hand, resumes some of the details collected from the fracture surface of sample IHL11, the one which presented evident shrinkage on the clamping area of the sample:

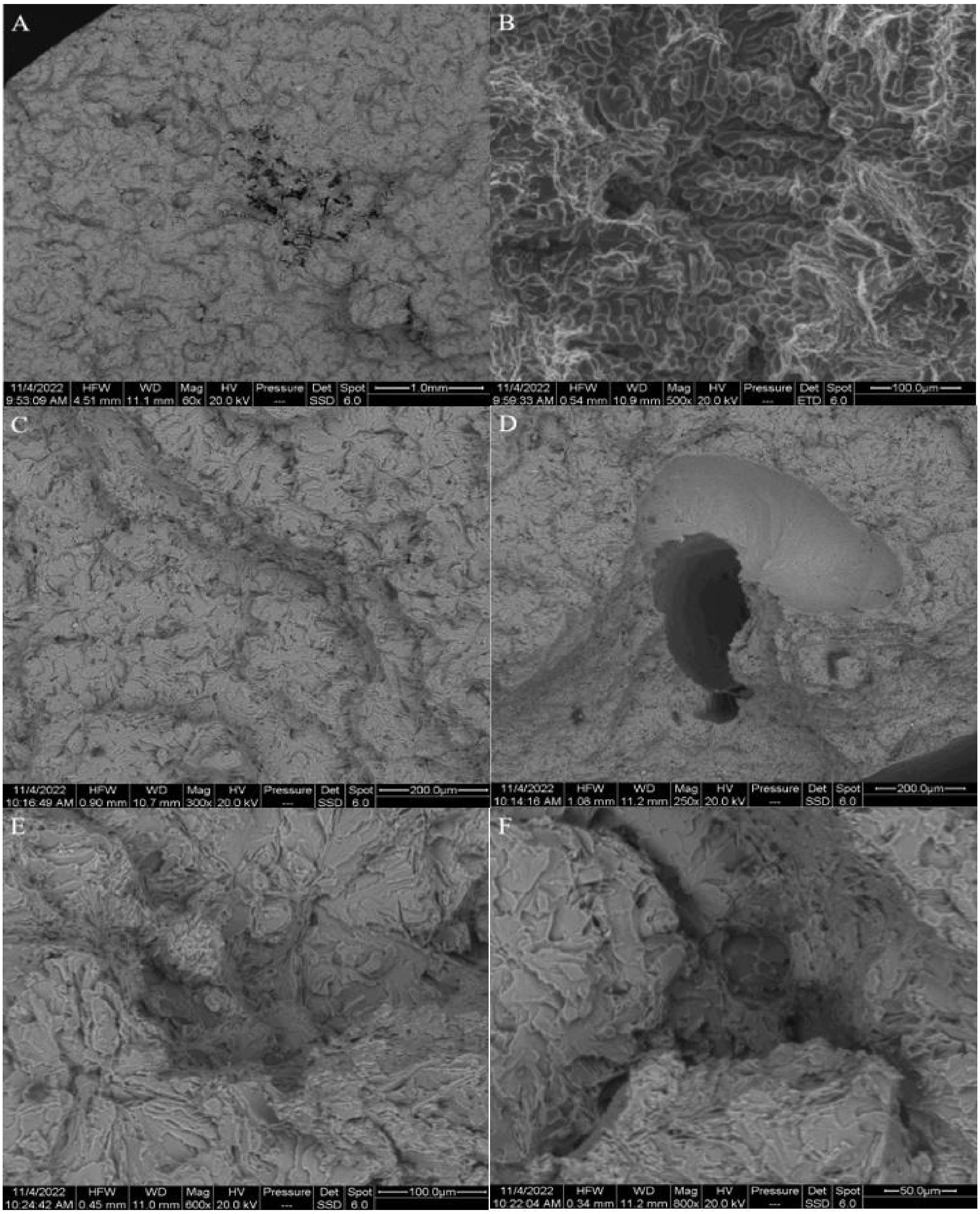

Figure 50: Fracture surface SEM images from sample IHL11. A (60x BSE) and B (500x, SE): small shrinkage porosity on fracture surface; C (300x, BSE): defect-free area; D (250x, BSE): gas porosity on the edge of the surface; E (600x, BSE) and F (800x, BSE): oxides

The six frames can be described as follows:

- Frames A and B: they reveal the presence of a small shrinkage porosity on the upper left side of the sample's section. It measures around 1 mm in diameter and dendrites can be seen protruding into the pore.

- Frame C: Magnification of a defect-free area. The fracture surface still resembles that of a fragile material, even if the elongation at fracture of this sample was 2,37 times greater than that of IHL6.
- Frame D: This frames captures the presence of a interestingly shaped pore on the bottom-right side of the fracture surface. Its smooth surface and rounded shape suggest that this is a gas porosity generated during solidification by a bubble. The bubble might have moved in an helix-shaped pattern, leaving behind this peculiar imprint. The presence of a sloped plane that runs along the edge of the fracture surface and starts where the pore is situated, implies that the sample's fracture might have started from this defect, or at least *also* from this defect.
- Frames E and F: these frames show some of the oxides detected on the surface. Note that the scale of these defects is intrinsically smaller than that of the oxides described in sample IHL6. Moreover, the total number of observable oxides seemed to be lower in this sample, and they were harder to detect on the surface.

Figure 51 shows the EDS analysis of frames B, C and F.

Note that in sample IHL11, no intermetallics of appreciable size could be detected.

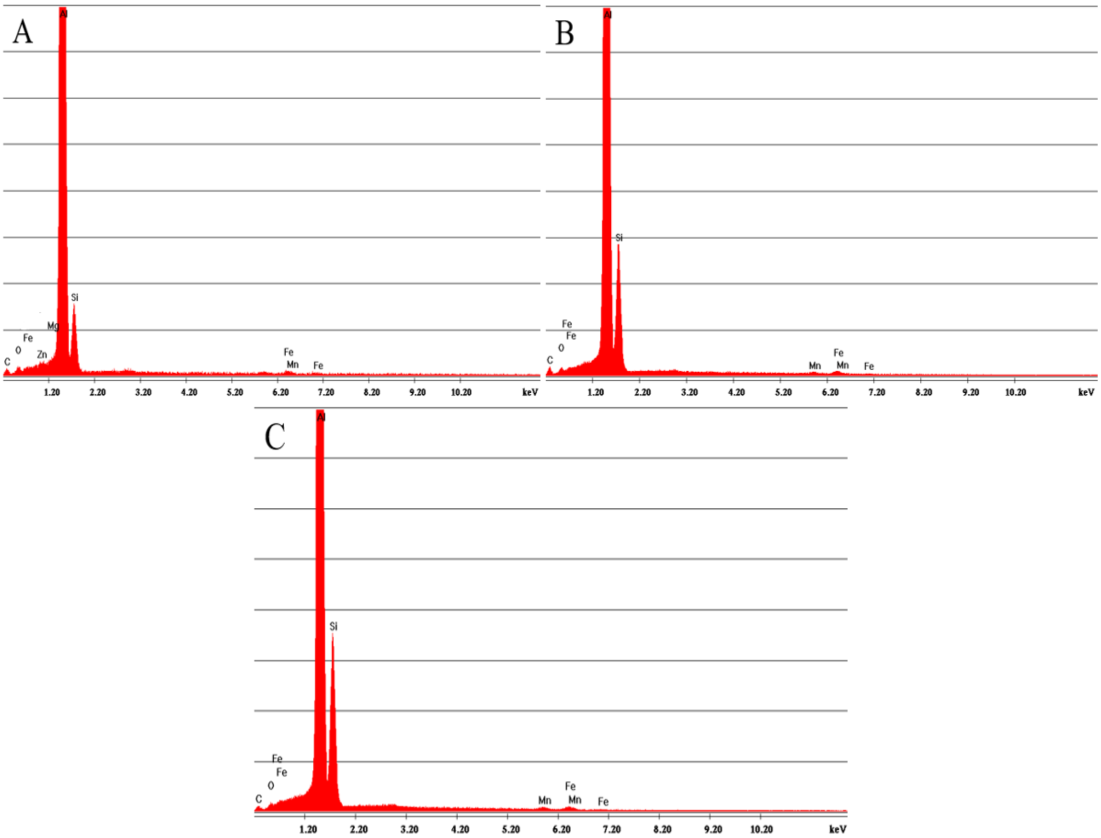

Figure 51: EDS of sample IHL11 fracture surface's regions. A: Shrinkage porosity; B: Area free from defects (i.e. matrix); C: oxide

3.4 Discussion

3.4.1 RPT Samples Porosity Discussion

The first aspect do be discussed about the RPT samples porosity analyisis is the importance of the parameters used during the image analysis protocol. The following parameters should always be specified and, hopefully in the future, standardized:

- Image Resolution, which is thightly intertwined to the machined used for image acquisition, wether it is a simple scanner or an optical microscope
- Grit of sand paper used during surface grinding
- Lower Detection Limit (LDL) set during image processing.

These three variables should always be specified and discussed in order to increase the comparability between data coming from different studies.

The second important factor is the use of a Specific Bifilm Index instead of the classically employed Bifilm Index. As previously discussed, the SpBI is a modified form of BI which has been normalized to the mass of the sample, changing its unit of measure to unit of length (of defects) over unit of mass (of alloy). This operation increases data comparability and refines the interpretation of the results.

The third fundamental result that emerged from this portion of the study concerns the statistical distribution of the results. The examination of the data collected during the image analysis showed that the majority of the pore descriptors (maximum Feret, pore equivalent diameter, perimeter, roundess) are not normally distributed, but rather lognormally distributed. This suggests that the usual assumption of normal distribution for this type of data is not correct. A better understanding of data distribution leads to a better interpretation of the results drawn from such data, enriching it with details about their mode and median values.

After this premise, we can move to what emerged from the information that we gathered from the RPT surfaces of this experiment:

- The increase in the DI for the scrap and poured ingot melts (SL and IH) was comparable, but different than that registered for the clean ingot melts (IL). In particular, IL showed modest increase in the DI, while SL and IH a bigger increase.
- Even if the mean maximum Feret can be attributed to melt SLH, the mean maximum Ferets of melts ILL and ILH are both greater than those of melts IHH and IHL. This means that, on average, the clean ingot melts (IL) had longer oxides than poured ingot melts (IH).
- Despite having long oxides, the SpBI of melt ILH is smaller than that of melts SLH and IHH, which also present greater increases in the SpBI per amount of hydrogen in solution.
- The biggest increase in pore equivalent diameter D_{eq} (and therefore in pore area) was registered for the SL melts, while melts IL and IH showed only a modest increase in D_{eq}. This can be confirmed also by naked eye by consulting Appendix A.

- Melts IL and SL showed a modest increase in pore number with increasing hydrogen, while melts IH showed a more drastic increase, doubling its number of pores.
- All melts showed a decrease towards 1 in the roundness value with increasing hydogen. Melt IHH showed the roundest pores on average.

These results can be interpreted as follows:

IL and SL melts are characterized by “old oxides”, and (ideally) no “new oxides” were introduced during the experiment. Since old oxides are known to be generally bigger, thicker and stiffer than new oxides, this could explain why the bigger mean maximum Ferets belonged to IL and SL melts. On the other hand, in addition to old oxides, melts IH were filled with new oxides during pouring operations, and new oxides are known to be thinner (therefore more likely to break) than old oxides. This could explain the low mean maximum Feret values registered for melts IH. In addition to this, the old oxides present in melts IH might have been broken by violent nature of the pouring operations, resulting in overall smaller oxides.

The next issue to be addressed is the number of pores. How can the number of pores increase at increasing hydrogen levels if we know that hydrogen cannot nucleate neither heterogeneously nor homogeneously into the melt? The logical answer would be that it does not. The number of pores counted during RPT image analysis is strictly dependent on the number of pores that actually open during solidification under reduced pressure. For this reason, at low hydrogen levels only a portion of the pores could open and fewer were counted, while at high hydrogen levels the higher amount of gas managed to open more bifilms. In the case of melt IHL, the low hydrogen available was able to open only a small amount of the bifilms, while in melt IHH the great majority of the oxides were inflated, making it seem like the number of oxides increased. Moreover, the small nature of these oxides allowed for their full expansion into spherical shape, both in low and high hydrogen conditions. In the case of melts IL, the low amount of oxides present meant that there were not many more to be opened at higher H concentrations, which resulted in modest increases in mean D_{eq}, pore number and SpBI. In the case of melts SL, the big old oxides present in the scrap could open freely at higher H concentrations, resulting in the massive increase in average pore area.

In all cases, the increase in hydrogen resulted in the oxides' inflation and a decrease towards 1 of the roundness value, an effect that was stronger in the poured ingot melts (IH).

Anyway, another interesting result is the indistinguishable nature of data when the hydrogen level falls below a certain threshold, that for this experiment was set at 0,1 ml/100. In fact, for melts ILL, SLL and IHL it is possible to conclude that:

- The DI values are comparable and, by considering the error intervals, virtually the same.
- The SpBI values are comparable and, by considering the error intervals, virtually the same.
- The mean pore equivalent diameters are comparable and, with respect to the changes registered at higher hydrogen levels (ILH, SLH, IHH), close in value for all the low hydrogen melts.
- The average pore number is comparable and, with respect to the changes registered at higher hydrogen levels (ILH, SLH, IHH), close in value for all the low hydrogen melts.

It is important to remind that all these data was collected from RPT samples solidified at 80mbar, so under partial vacuum (8% of the atmospheric pressure).

In other words it was shown that, at low hydrogen levels, the evaluation of melt quality by means of the SpBI and the porosity of RPT samples cannot be trusted completely. On the other hand, at higher hydrogen values, this evaluation is able to highlight the differences in melt quality at a greater extent, revealing the differences both in the quality of the raw material (ingot vs scrap), and eventual damage perpetrated during melt handling.

One last consideration should be dedicated to the difference between melts IH and SL. It is be clear by now that the intent was to create two different kinds of "dirty" melts: one characterized by new oxides introduced during melt handling through pouring operations, and the other characterized by old oxides intrinsically present in the scrap material. The objective was to evaluate the different behavior of these melts at different hydrogen levels. What emerged is that, in terms of SpBI and DI values, no appreciable difference could be observed. Anyway, by studying other pore descriptors such as pore number and average pore area, it can be assumed that:

- The pouring operations introduced an high number of small/short oxide bifilms.
- The pouring operations broke the pre-existing oxide bifilms of the ingot.
- The scrap melt presented longer bifilms and, therefore, bigger pores.

This said, it is difficult to establish what is the proportion between newly introduced oxides and pre-existing broken oxides.

Lastly, it seems good measure to address the following concern: the high levels of hydrogen of melts IHH and SLH paired with a somewhat pronounced spherical shape of the pores and low solidification pressure (80 mbar), might suggest an "overinflation" of the bifilms. If much gas precipitates, because there is much gas in solution, the gas pore may eventually outgrow its original bifilm to become a large spherical pore as shown in Figure 52:

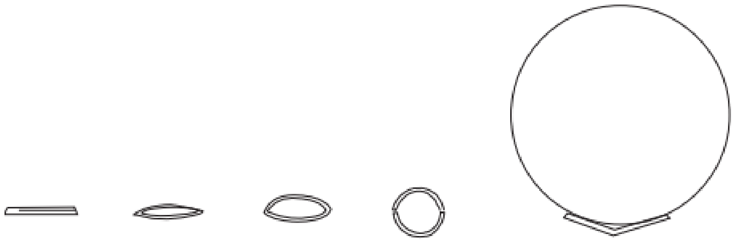

Figure 52: Overinflation of a bifilm by hydrogen gas [19]

For this reason, some additional microscopy and chemical analysis of the RPT surfaces would have been useful.

3.4.2 Mechanical Properties and SEM/EDS Analysis Discussion

During the analysis of mechanical data, two main results emerged:

1) No appreciable difference in mechanical properties could be observed between different melt conditions. Every melt, indipendently from the raw material, pouring operations or hydrogen level, showed comparable properties. This is also shown in Appendix B (images 4B and 5B).

2) A clear difference in mechanical properties emerged between samples that presented evidence of shrinkage porosity on their surface at the height of the clamping area, and those who did not (see Figure 35 for reference). On average, “s” class samples (visible shrinkage) exhibited higher UTS and percent elongation at fracture.

A possible explanation to both of these results may come directly from the casting procedure and parameters. First of all, it is important to mention that each casting procedure required the melt to be skimmed and the spoon to be immersed again, with the risk of causing entrainment and introducing impurities into the melt. If we consider the small amount of melt (about 7kg) and the high number of castings, this detail might become influential on the melt quality of later castings.

In addition, tensile test bars were cast into a Sthal Mold model die, a type of die that has been widely used in the industry to evaluate the quality of molten aluminum and the response of alloy to the heat treatment processing. Unfortunately, this type of mold desing suffers from shrinkage porosity, a problem that several researchers have previously reported [131,132] and tried to solve [133,134]. This shrinkage porosity results in less-than-optimum as-cast tensile properties being developed in the test bar mold, which might not correctly represent the actual mechanical properties of the alloy that is being tested. For this reason, the lack of any difference in mechanical properties between melt conditions is probably the result of this inconvenient.

This theory is corroborated by the presence of both evident surface shrinkage in the ”s” class samples and less visible internal shrinkage porosity in samples that did not show any surface defect. In fact, the SEM analysis confirmed the presence of a considerably big shrinkage porosity right in the center of the ”n” class sample IHH6, whose surface did not show any visible defect. The pore had a maximum Feret of around 3,5 mm, on a fracture surface of diameter 8,4 mm.

Since only two fracture surfaces were analyzied with the aid of the SEM, of which only one belonged to the ”n” class, it is impossible to state that every ”n” class sample suffered from internal shrinkage porosity. Nevertheless, the overall inferior mechanical properties paired with the observations of other researchers [131-134] suggest that this cannot be excluded.

Another aspect that needs to be addressed is the presence and nature of the FeMnCr rich intermetallics observed on the fracture surface of sample IHH6, and that were instead almost invisible in sample IHH11. Their considerable size (over 150 µm in length) suggests that they had the time to grow in size and depleat the surrounding melt of Fe, Mn and Cr, which again implies that the solidification time of sample IHH6 was different than the one of sample IHH11 and, in particular, longer. Moreover, Campbell suggests that the nucleation of these intermetallics is favored by the presence of oxides [19], stating that bifims act as favorable nucleation sites for most kinds of intermetallics (see §1.6.1). This last consideration, paired with the fact that an overall smaller number of oxides could be observed in sample IHH11 during SEM analysis, could mean that the overall amount of oxides present in sample IHH6 was greater than that of sample IHH11.

A possible conclusion could be the following: since the ”s” class samples tended to appear in the earlier castings, when the die was colder, this would result in them solidifying faster. Furthermore, earlier samples corresponded to less damaged melt since, as stated above, every time a casting was completed the melt was subjected to additional damage. This could result in a reduced oxide content with respect to the last cast samples. The faster solidification time and the possibly lower amount of oxides of earlier samples could have inhibited the nucleation and growh of the FeMnCr intermetallics, which would result in better mechanical properties. Also, it is possible that all the samples suffered from shrinkage porosity, with the difference that some accomodated most of it in the clamping area (”s” class samples) and some hid it in the reduced section (”n” class samples). The first ones would therefore benefit from better mechanical properties than the second.

It is of course difficult to confirm this theory without the better knowledge of important variables such as the casting temperature, the die temperature at the moment of each casting and the SEM/EDS analysis of other fracture surfaces.

CONCLUSIONS

The work of this thesis has been focused on the study of the effects of hydrogen concentration and melt quality of an AlSi11(Fe) Foundry Alloy, through the analysis of the porosity developed on RPT samples, mechanical properties such as Yield Strenght, UTS and percent elongation at fracture, and SEM/EDS analysis of fracture surfaces.

The porosity analysis carried out on the sections of the RPT samples collected from 6 different melt conditions concluded that:

- The parameters used during the image analysis procedure are important and should always be specified.
- The distribution of some pore descriptors is lognormal and not, as sometimes assumed, normal.
- The use of a Specific Bifilm Index normalized to the mass of the samples is reccomended because it increases data comparability, both within the same study and within different studies.
- The influence of hydrogen on the porosity of RPT samples is a function of the melt quality. If the melt is clean (100% ingot, no damaging pouring operations), the influence of hydrogen on porosity is small and likely ascribable to pre-existing impurities in the raw material. On the other hand, if the melt is dirty, either because of the presence of scrap or because of damaging operations such as repeated pourings, the influence of hydrogen on porosity is greater and depends on the nature of the oxides.
- The pouring operations to which some of the melts were subjected, resulted in the introduction of new small oxides, and in the probable fragmentation of the pre-existing old oxides in smaller pieces. These results would support the thesis according to which hydrogen does not play any direct role in pore formation, but rather acts as a sort of "flashlight" that, if present in sufficient amount, helps to reveal the true quality of a melt. In other words, the RPT porosity analysis as a way

to assess melt quality should always be done in light of the amount of hydrogen present in the melt.

The analysis of the static mechanical properties, paired with further Scanning Electron Microscopy and Energy Dispersive X-Ray Spectroscopy of the fracture surfaces concluded that the Sthal Model mold casting was inadequate for the experiment, and was unable to correctly represent the actual mechanical properties of the melt condition that was being tested. Because of this, it was impossible to correlate the mechanical properties of the different melts to their RPT's porosity analysis.

RIASSUNTO

La tesi, avente come titolo “Effetti della Concentrazione di Idrogeno e Bifilm sulla Porosità e Proprietà Meccaniche di una Lega da Fonderia di Tipo AlSi11(Fe)”, ha avuto come oggetto di indagine l’influenza della quantità di idrogeno in soluzione in diversi fusi preparati a partire dalla lega AlSi11(Fe) sullo sviluppo della porosità e sulle proprietà meccaniche.

L’alluminio è il materiale metallico più presente sulla terra e il suo utilizzo nell’industria dell’automotive, nonché nelle tecnologie cardine della transizione energetica, ha subito un costante incremento negli ultimi decenni. In particolar modo, le leghe di alluminio da fonderia costituiscono più del 50% della quantità di alluminio utilizzata nel settore automobilistico.

Le porosità costituiscono uno dei difetti da solidificazione più problematici nelle leghe da fonderia, influenzando le proprietà meccaniche e le prestazioni generali del componente colato, e possono essere riconducibili a due tipi diversi:

- Porosità da gas
- Porosità da ritiro

La porosità da ritiro avviene nel componente a causa di ritiri volumetrici che seguono alla transizione dallo stato liquido a quello solido, mentre le porosità da gas sono in genere sferiche e presentano una superficie interna lucida e liscia. Siccome l’unico gas a presentare una solubilità rilevante nell’alluminio liquido è l’idrogeno, per molto tempo si è creduto che all’origine della porosità da gas ci fosse il calo di solubilità di questo gas che avviene con il passaggio della lega dallo stato liquido a quello solido: secondo questa teoria, l’avanzata del fronte di solidificazione espellerebbe idrogeno nel metallo liquido fino a supersaturarlo, causando come risultato la nucleazione di bolle di gas. Queste rimbarrebbero quindi intrappolate all’interno del componente una volta solidificato.

Per quanto questa spiegazione sembrasse corretta, è stato in seguito dimostrato come l’idrogeno non possa nucleare né eterogeneamente, né omogeneamente nelle leghe di

alluminio allo stato liquido. Per questo motivo, la formazione della porosità da gas necessitava di una nuova spiegazione. Un modello che potrebbe spiegare questo fenomeno è stato proposto dagli stessi ricercatori che hanno confutato il modello precedente, e fonda le proprie basi sul concetto di “bifilm”.

La maggior parte dei metalli allo stato liquido presenta un sottile strato di ossido che galleggia in superficie, formatosi a causa dell’esposizione all’aria. Generalmente, per le leghe di alluminio, questo ossido è composto prevalentemente da allumina (amorfa, α, γ) o spinello e magnesia se in lega è presente del magnesio.

Quando il fuso è soggetto a moti turbolenti, questo strato superficiale può ripiegarsi su se stesso (bifilm) ed essere disperso in pezzi all’interno del liquido, come mostrato in Figura 1:

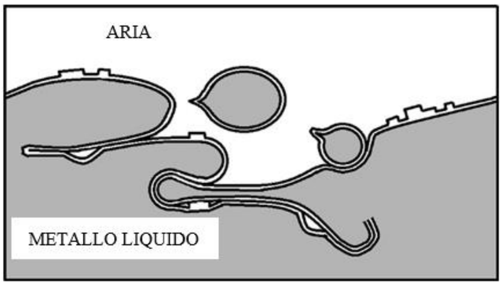

Figura 1: Meccanismo di ”entrainment”, ovvero inglobamento di porzioni di ossido superficiale a causa di moti turbolenti

Questo meccanismo di inglobamento è detto “entrainment”, e comporta l’ingresso di bifilm di ossido nel fuso, le cui superfici secce sono incapaci di formare un legame. La densità dell’ossido è in genere lievemente superiore a quello della lega, ma lo strato di aria contenuto tra i due lembi fa sì che la densità totale del bifilm sia pressocchè la stessa del metallo. Per questo motivo, i bifilm continuano a galleggiare indefinitamente nel tempo, senza mai affiorare od affondare, rendendo impossibile una auto-pulizia del fuso che sia dipendente dal tempo. Si dice quindi che i difetti da entrainment sono cumulativi: più ne vengono introdotti, più se ne accumulano.

La superficie asciutta e disgiunta del bifilm permette una riduzone considerevole dell’energia necessaria alla bolla di idrogeno per precipitare, in quanto rimuove la componente energetica legata alla formazione di nuova superficie. In altre parole, il bifilm agisce come una sorta di sacca in cui l’idrogeno può diffondere con piccolo sforzo.

Ad ogni modo, oltre a fornire una eventuale spiegazione ai meccanismi di formazione delle porosità da gas, i bifilm influenzano molteplici altri difetti e caratteristiche del fuso, comportando come risultato finale una riduzione delle proprietà meccaniche come tensione di rottura ed allungamento a rottura.

D'altro canto, i bifilm sono influenzati a loro volta da innumerevoli variabili tra cui:

- La composizione della lega, e in particolare il tenore di Magnesio;
- Le operazioni di versamento e mescolamento del fuso in fase di produzione del componente, che causano turbolenze in grado di incrementare la quantità di bifilm;
- La forma dello stampo e le sue caratteristiche;
- La quantità di idrogeno disciolta nella lega;
- La presenza e la tipologia di affinanti del grano;
- L'utilizzo di boccame (rottame interno) nella fase di preparazione del fuso in aggiunta al lingotto;

Data l'importanza dei bifilm e il loro ruolo primario nella generazione e sviluppo di difetti nelle leghe di alluminio da fonderia, risulta imperante disporre di tecnologie che permettano di valutare fedelmente la qualità del fuso. Uno dei metodi più utilizzati è il Reduced Pressure Test, e consiste nell'analisi di campioni di metallo liquido solidificati in condizioni di vuoto parziale. La bassa pressione favorisce infatti l'espansione dei bifilms ad opera dell'idrogeno, andando ad evidenziare la presenza di entrambi.

Ad ogni modo, questa interazione tra idrogeno e bifilm può essere considerata come dannosa nei provini RPT per la corretta valutazione della qualità di un fuso. Infatti, in un fuso ideale in cui la quantità di idrogeno sia minima, la popolazione di bifilm potrebbe non essere adeguatamente rappresentata dal test RPT, in quanto l'idrogeno non sarebbe sufficiente ad espandere tutti gli ossidi. Questo, di conseguenza, comporterebbe una sottostima della quantità di bifilm presenti in tale fuso.

Il principale obiettivo di questa tesi è proprio quello di indagare più a fondo la relazione tra idrogeno i bifilm nella valutazione della qualità delle leghe in alluminio da fonderia. Per quantificare il danno da bifilm, si fa ricorso ad un indice che prende il nome di "Bifilm Index", e che viene definito secondo la seguente equazione:

$$BI = \sum(maximum\ Feret)$$

Ovvero come la somma dei diametri di Feret di ciascun poro che viene contato sulla superficie del provino RPT, appositamente sezionato e lucidato.
Un altro indice utile in fase di confronto tra i provini RPT è il Density Index, che permette di valutare la riduzione di densità di un provino RPT in funzione della porosità che contiene, e in riferimento ad un provino di controllo che viene invece solidificato a pressione atmosferica.

La tesi si è valsa, oltre che di una esaustiva revisione della letteratura, di una consistente parte sperimentale. Tale lavoro sperimentale si è suddiviso tra il dipartimento della "Jonkoping Tekniska Hogskolan" dell'Università di Jonkoping in Svezia e i laboratori siti a Vicenza dell'Università degli Studi di Padova del dipartimento di ingegneria industriale.
In Svezia si sono concentrati: la fase di preparazione dei fusi, il collezionamento dei provini RPT e meccanici, preparazione e analisi delle immagini dei provini RPT al microscopio ottico, preparazione e analisi tramite prove meccaniche dei provini ad osso di cane. In Italia si è invece proceduto all'analisi al Microscopio Elettronico a Scansione (SEM) e della Spettrometria per Dispersione di Energia (EDS) di alcune superfici di frattura dei provini meccanici.

La prima fase dell'esperimento si è concentrata sullo sviluppo di un protocollo per l'analisi della porosità nei provini RPT che fosse caratterizzato da parametri giustificati, in modo da garantirne l'efficacia e la ripetibilità. Per fare ciò, si è proceduto con due test di collaudo che hanno permesso di identificare come ottimali:

- Grit 1000 in fase di lucidatura delle superfici dei provini RPT
- L'acquisizione dell'intera superficie del provino RPT tramite l'uso della funzione di "stitching" del microscopio ottico (Olympus DSX 1000), con risoluzione di 4440 dpi.
- L'impostazione del limite di detezione inferiore (LDL) a 200000 µm^2 per la porosità. L'LDL stabilisce qual è l'area del poro più piccolo che si vuole

considerare nella fase di analisi dell'immagine. Ogni poro la cui area sia inferiore all'LDL verrà trascurato.

- L'uso del Bifilm Index Specifico (SpBI) rispetto al BI classico in fase di analisi e confronto dei dati. L'SpBI è una forma del BI che viene normalizzata rispetto alla massa del campione RPT da cui è calcolato tale BI.

In una seconda fase dell'esperimento si è proceduto alla costruzione di un sistema di degasaggio: un tubo in acciaio di 5 mm di diametro è stato coperto da 3 cilindri di grafite densa, ciascuno di 40 mm di lunghezza, e la sua estremità inserita in un coperchio cilindrico di grafite porosa (40 mm di lunghezza) che permettesse la diffusione del gas attraverso i pori, ma impedisse l'ingresso dell'alluminio al suo interno. La grafite densa doveva impedire il contatto tra alluminio liquido e tubo in acciaio. I punti di contatto tra i vari cilindri di grafite sono infine stati incollati con l'uso di una colla ceramica (base Resbond® 940LE unita ad attivatore Resbond® 940LE, Final Materials). La lancia da degasaggio è mostrata in Figura 2a, mentre il suo funzionamento è schematizzato in Figura 2b.

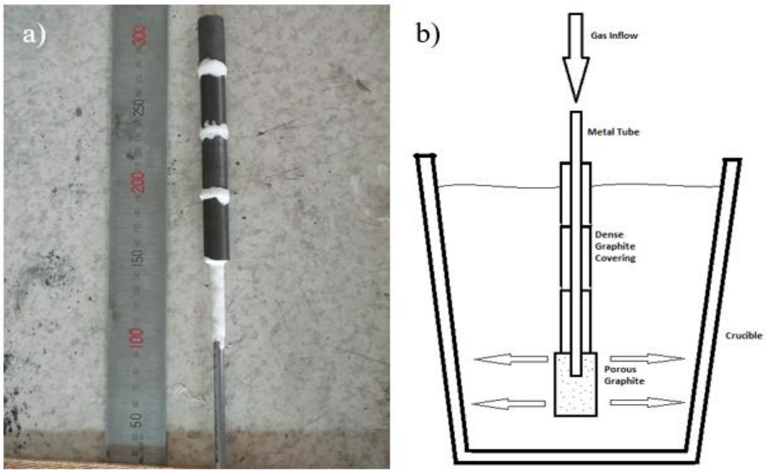

Figura 2: a) Lancia da degasaggio: tubo in acciaio ricoperto da cilindri di grafite densa ed estremità in grafite porosa; b) Schematizzazione del funzionamento della lancia da degasaggio

Per operare i degasaggi, l'estremità libera del tubo in acciaio è stata collegata ad un flussimetro e ad una bombola di Argon (Air Liquide®). Tutti i degasaggi sono stati operati ad un flusso di **0,4 slpm** (litri standard al minuto) di argon.

La lancia era stata concepita per essere utilizzata anche nelle fasi di gasaggio dei fusi, in modo da incrementarne il tenore di idrogeno, ma è risultata inefficace. Il gasaggio è quindi stato operato per aggiunta di partiglie Dycastal 41 della FOSECO.

Una volta stabiliti i parametri del protocollo di analisi di immagine e sviluppato il sistema di degasaggio, si è proceduto con la produzione dei campioni.

Per studiare l'influenza della quantità di idrogeno e dei bifilm sulla porosità e le proprietà meccaniche da lega binaria di alluminio AlSi11(Fe) (composizione estesa in Tabella 1) si sono utilizzati 6 fusi diversi con diverse condizioni di preparazione:

- Fuso ILL: Preparato a partire da lingotti (100%) di AlSi11(Fe) e a basso tenore di idrogeno;
- Fuso ILH: Preparato a partire da lingotti (100%) di AlSi11(Fe) e ad alto tenore di idrogeno. I fusi ILL e ILH costituiscono assieme la condizione IL, ovvero 100% lingotto. Essi permettono di studiare gli effetti di alto e basso tenore di idrogeno su un fuso costituito da lingotto puro;
- Fuso SLL: Preparato a partire da boccame (100%) di AlSi11(Fe) e a basso tenore di idrogeno;
- Fuso SLH: Preparato a partire da boccame (100%) di AlSi11(Fe) e ad alto tenore di idrogeno. I fusi SLL ed SLH costituiscono assieme la condizione SL, ovvero 100% boccame. Essi permettono di studiare gli effetti di alto e basso tenore di idrogeno su un fuso costituito da solo boccame;
- Fuso IHL: Preparato a partire da lingotti (100%) di AlSi11(Fe) e a basso tenore di idrogeno. Questo fuso è stato soggetto ad operazioni di versamento che risultano in un incremento del numero di bifilm di tipo "nuovo";
- Fuso IHH: Preparato a partire da lingotti (100%) di AlSi11(Fe) e ad alto tenore di idrogeno. Questo fuso è stato soggetto ad operazioni di versamento che risultano in un incremento del numero di bifilm di tipo "nuovo". I fusi IHL e IHH costituiscono assieme la condizione IH, ovvero 100% lingotto danneggiato dalle operazioni di versamento. Essi permettono di studiare gli effetti di alto e basso tenore di idrogeno su un fuso costituito da lingotto puro danneggiato.

COMPOSIZIONE DELLA LEGA								
Elem.	Si	Fe	Cu	Mn	Mg	Cr	Ni	Zn
[%]	10,97	0,797	0,0386	0,356	0,0087	0,0196	0,0035	0,0392
	Ti	Be	Bi	Ca	Cd	Ga	Sr	Al
	0,0207	0,0011	0,0041	0,00056	0,0012	0,0101	~ 0	87,7

Tabella 1: Composizine della lega utilizzata, ottenuta tramite analisi allo spettrometro SPECTROMAXx della Amtek

I fusi sono tutti stati preparati ponendo all’incirca 6 kg di materiale grezzo (lingotti o boccame a differenza del tipo di fuso) in una fornace Nabertherm® impostata a 800°C e provvista di un crogiolo di 22 cm di altezza per 18 cm di diametro superiore.

Il tenore di idrogeno è stato monitorato durante tutte le fasi dell’esperimento tramite un HYCAL®, fino al momento della colata dei provini meccanici.

I provini RPT sono stati raccolti dal fuso ad una temperatura di 700±2°C e solidificati lasciandoli a 80 mbar per 6 minuti in una macchina RPT modello Vacuum Density Tester 3VT CT della GMBH.

Per ogni fuso si è raccolto anche un provino lasciato solidificare a pressione atmosferica per il calcolo del Density Index.

I provini meccanici sono stati collezionati per ogni tipo di fuso **dopo** i provini RPT, lasciando che il metallo raggiungesse i 720°C e utilizzando uno stampo modello Sthal (Figura 3) preriscaldato in un forno Nabertherm® a 250°C.

Figura 3: Stampo modello Sthal utilizzato per la creazione dei provini meccanici ed esempio di componente colato.

I parametri dei vari tipi di fuso[N] sono elencati di seguito (NB: ai fusi ad alto tenore di idrogeno è stato necessario seguire il gasaggio con un breve degasaggio che riducesse

---

[N] **Codici dei fusi: ILL** (100% lingotto, [H] basso), **ILH** (100% lingotto, [H] alto), **SLL** (100% boccame, [H] basso), **SLH** (100% boccame, [H] alto), **IHL** (100% lingotto riversato, [H] basso), **IHH** (100% lingotto riversato, [H] alto)

la quantità di ossidi introdotti durante la prima operazione, fenomeno dovuto alla natura turbolenta dell'aggiunta delle pastiglie Dycastal 41) :

- ILL: Una volta raggiunto lo stato liquido: degasaggio di 25 minuti. Concentrazione finale di idrogeno: 0,090 ml/100g.
  Metodo di raccolta dei provini RPT: Per immersione della coppetta.
- ILH: Una volta raggiunto lo stato liquido: gasaggio con 5/12 di pastiglia + degasaggio di 10 minuti per pulizia
  Concentrazione finale di idrogeno: 0,065 ml/100g.
  Metodo di raccolta dei provini RPT: Per immersione della coppetta
- SLL: Una volta raggiunto lo stato liquido: degasaggio di 25 minuti. Concentrazione finale di idrogeno: 0,065 ml/100g.
  Metodo di raccolta dei provini RPT: Per immersione della coppetta.
- SLH: Una volta raggiunto lo stato liquido: gasaggio con 1/4 di pastiglia + degasaggio di 10 minuti per pulizia
  Concentrazione finale di idrogeno: 0,090 ml/100g.
  Metodo di raccolta dei provini RPT: Per immersione della coppetta.
- IHL: Una volta raggiunto lo stato liquido: degasaggio di 25 minuti
  Operazioni di riversamento: Tramite l'uso di un mestolo pre-riscaldato,10 volte da un'altezza di 25 cm. Necessario ulteriore degasaggio di 25 min a causa di un incremento eccessivo del tenore di idrogeno a seguito dei riversamenti.
  Concentrazione finale di idrogeno: 0,056 ml/100g.
  Metodo di raccolta dei provini RPT: Per versamento del fuso da 12,5 cm di altezza, direttamente nella coppetta RPT.
- IHH: Una volta raggiunto lo stato liquido: gasaggio con 1/3 di pastiglia.
  Operazioni di riversamento: Tramite l'uso di un mestolo pre-riscaldato,10 volte da un'altezza di 25 cm. Necessario successivo degasaggio di 25 min per garantire stesse condizioni di IHL dopo i riversamenti
  Concentrazione finale di idrogeno: 0,348 ml/100g.
  Metodo di raccolta dei provini RPT: Per versamento del fuso da 12,5 cm di altezza, direttamente nella coppetta RPT.

Nel calcolo del Density Index è stato utilizzata come densità di riferimento quella del provino solidificato a pressione atmosferica con densità maggiore (da fuso IHH, ρ = 2,585 g/cm^3). Il DI è calcolato secondo la formula:

$$DI = \left(\frac{\rho_{atm} - \rho_{80mbar}}{\rho_{atm}}\right) \times 100$$

Dove ρ_{atm} è la densità del provino di riferimento solidificato a pressione atmosferica e ρ_{80mbar} è la densità del provino RPT di cui si vuole calcolare il DI. Le densità sono state calcolate tramite il principio di Archimede, pesando i provini in aria e in acqua.

I risultati del DI in funzione del tenore di idrogeno per i vari fusi sono riportati in Figura 4, e mostrano come il DI sia aumentato notevolmente nel caso dei fusi SL (SLL, SLH) e IH (IHL, IHH) per alti valori di idrogeno, mentre solo marginalmente nel caso del fuso IL (ILL, ILH)[N].

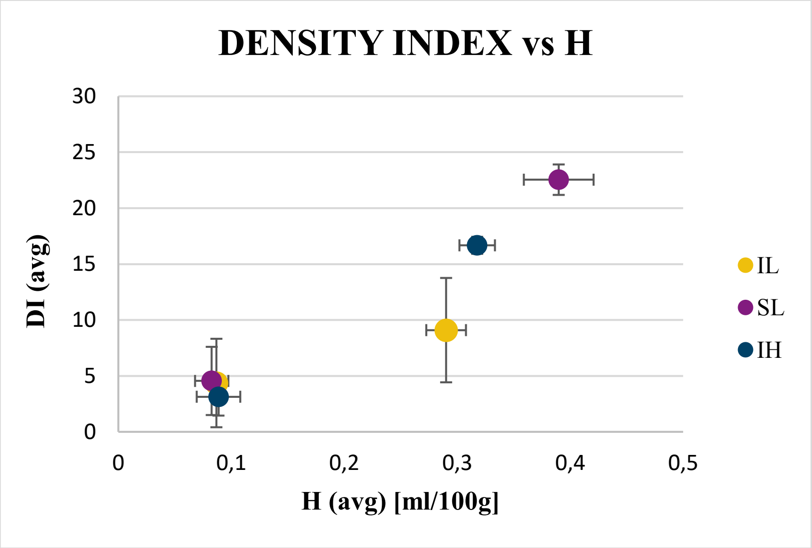

Figura 4: Density Index vs H per i vari fusi. IL: fusi ILL (basso tenore di H) e ILH (alto tenore di H); SL: fusi SLL e SLH; IH: fusi IHL e IHH.

I provini RPT sono quindi stati sezionati lungo l'asse di simmetria, lucidati fino a grit 1000, e scansionati al microscopio ottico con uno zoom 3x. Le immagini così acquisite sono state elaborate dal software ImageJ impostando un LDL di 200000 µm^2 per ottenere:

- Numero di pori

[N] **Codici dei fusi: ILL** (100% lingotto, [H] basso), **ILH** (100% lingotto, [H] alto), **SLL** (100% boccame, [H] basso), **SLH** (100% boccame, [H] alto), **IHL** (100% lingotto riversato, [H] basso), **IHH** (100% lingotto riversato, [H] alto)

- Area dei pori, e quindi diametro equivalente degli stessi calcolato tramite l'equazione: $D_{eq} = \sqrt{\frac{4A_{poro}}{\pi}}$
- Perimetro dei pori, e quindi la rotondità degli stessi calcolata tramite l'equazione: $Rotondità = \frac{P^2}{4\pi A_{poro}}$
- Diametro di Feret massimo dei pori (DFmax)
- Area della superficie del campione

Questi dati sono stati quindi analizzati sia con Excel® che con il softaware statistico Minitab®, permettendo di stabilire che i dati relativi al DFmax, diametro equivalente e rotondità dei pori sono distribuiti lognormalmente, e dunque non normalmente (Figura 5). Inoltre, all'aumentare del tenore di idrogeno:

- L'incremento del BI specifico più consistente si registra per i fusi SL e IH (boccame e lingotto riversato rispettivamente). L'incremento del BI specifico del fuso IL (lingotto) è invece nettamente inferiore. (Figura 5a)
- L'incremento del D_{eq} medio più notevole si registra per il fuso SL, mentre i fusi IL e IH non subiscono grosse variazioni (Figura 6a)
- La percentuale di porosità superficiale (Pore%) è calcolata in un campione come il rapporto tra la somma delle aree dei pori e la superficie del provino. All'aumentare del tenore di idrogeno, l'incremento di Pore% è considerevole per i fusi SL ed IH, ma solamente marginale nel fuso IL. (Figura 5b)
- Il numero di pori medio aumenta decisamente nel fuso IH, mentre non varia nei fusi IL ed SL. (Figura 5c)
- La rotondità tende a diminuire verso 1 in tutte e tre le condizioni (IL, SL, IH). In particolare, il decremento più notevole si è registrato per il fuso IH nella condizione IHH. (Figura 6b)

Si osserva inoltre che il DFmax medio più alto si registra per il fuso SLH, seguito dai fusi ILL e ILH (Figura 6c).

In seguito all'analisi delle porosità, si è proceduto selezionando 12 provini meccanici per ogni condizione (72 provini in tutto) e testandoli meccanicamente per mezzo di una macchina per prove meccaniche Zwick/Roell Z100. I risultati delle prove meccaniche relativi alla tensione di snervamento, tensione di rottura ed allungamento a rottura sono riportati in Figura 7.

Si osservi come le proprietà meccaniche registrate nelle diverse condizioni siano sempre le stesse, ed estremamente distribuite nel caso della tensione di rottura e dell’allungamento a rottura.

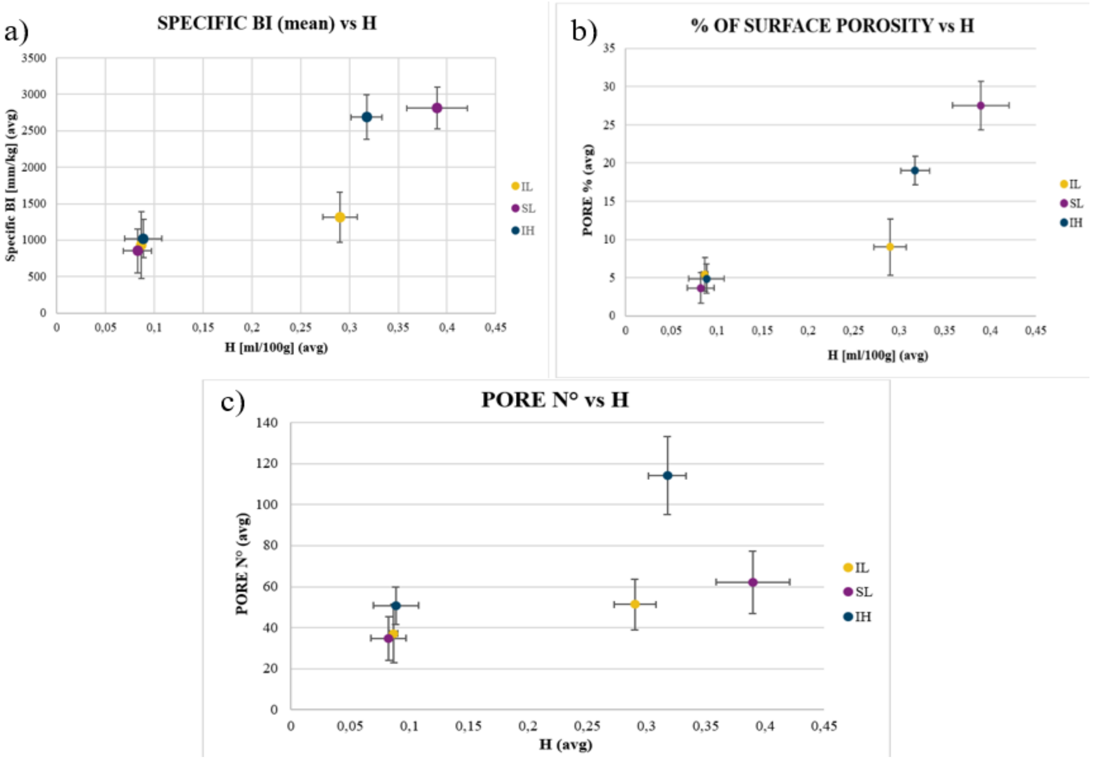

Figura 5: Variazione di descrittori della porosità al variare del tenore di idrogeno. Ogni fuso (IL, SL, IH) è rappresentata da 2 punti, uno che corrisponde al basso tenore di idrogeno, e l'altro all'alto tenore di idrogeno.

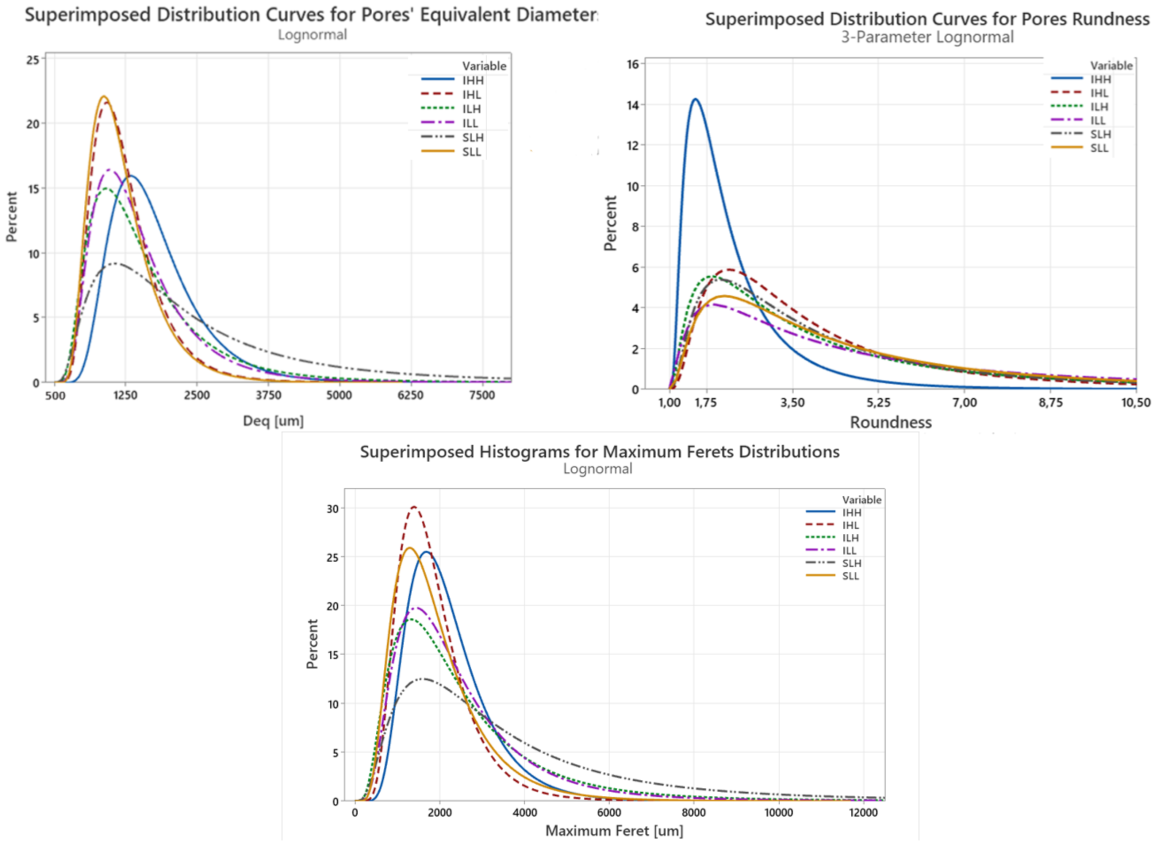

Figura 6: Variazione di descrittori della porosità a distribuzine lognormale, al variare del tenore di idrogeno. Ogni curva rappresenta una delle 6 condizioni.

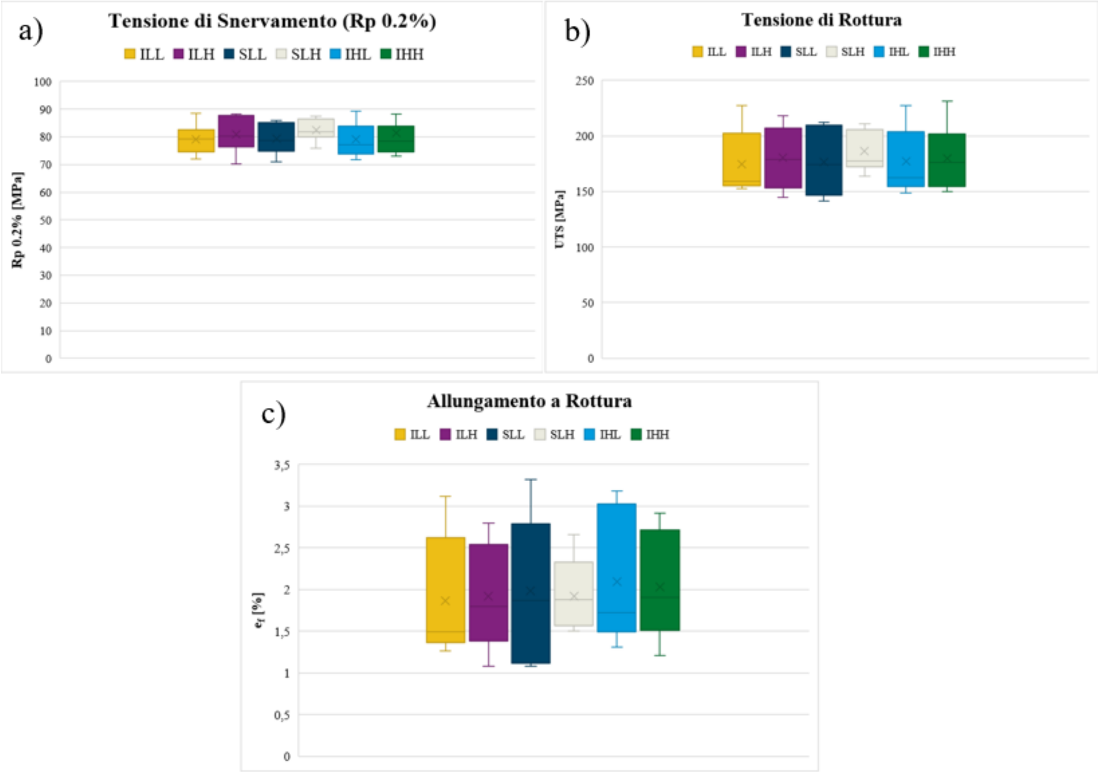

Figura 7: Proprietà meccaniche dei diversi tipi di fuso. a) tensione di snervamento; b) tensione di rottura; c) allungamento a rottura

Si è proceduto con l’analisi al microscopio elettronico a scansione (SEM, modello Quanta Field Emission Gun 250 fornito da FEI) e alla Spettrometria per Dispersione di Energia (EDS) di due superfici di frattura di provini meccanici provenienti dallo stesso fuso (IHL[N]) ma che presentano proprietà meccaniche molto diverse (Tabella 2).

PROPRIETA’ MECCANICHE DEI PROVINI ESAMINATI AL SEM			
Codice Provino	Tensione di Snervamento [MPa]	Tensione di Rottura [MPa]	Allungamento a Rottura [%]
IHL6	80,8	148,5	1,30
IHL11	82,8	204,8	3,09

Tabella 2: Proprietà meccaniche dei due provini meccanici la cui superficie di frattura è stata analizzata al SEM

L’analisi delle superfici di frattura ha rilevato la presenza di grossi intermetallici FeMnCr (Figura 8a) e una vasta porosità da ritiro (Figura 8b) al centro del campione IHL6 (con proprietà meccaniche più scadenti), mentre nessun intermetallico e una piccola porosità da ritiro (Figura 8c) nel campione IHL11. La presenza degli

---

[N] **Codici dei fusi: ILL** (100% lingotto, [H] basso), **ILH** (100% lingotto, [H] alto), **SLL** (100% boccame, [H] basso), **SLH** (100% boccame, [H] alto), **IHL** (100% lingotto riversato, [H] basso), **IHH** (100% lingotto riversato, [H] alto)

intermetallici e la loro dimensione fa trasparire che il tempo di solidificazione dei due campioni è stato diverso.

La totale mancanza di correlazione tra la variazione della porosità e la variazione delle proprietà meccaniche, nonchè i risultati dell'analisi al SEM, suggeriscono che i provini meccanici non siano stati in grado di rappresentare fedelmente le proprietà meccaniche dei fusi. In altre parole, risulta che lo stampo modello Sthal sia inadeguato nella produzione di campioni per le prove meccaniche.

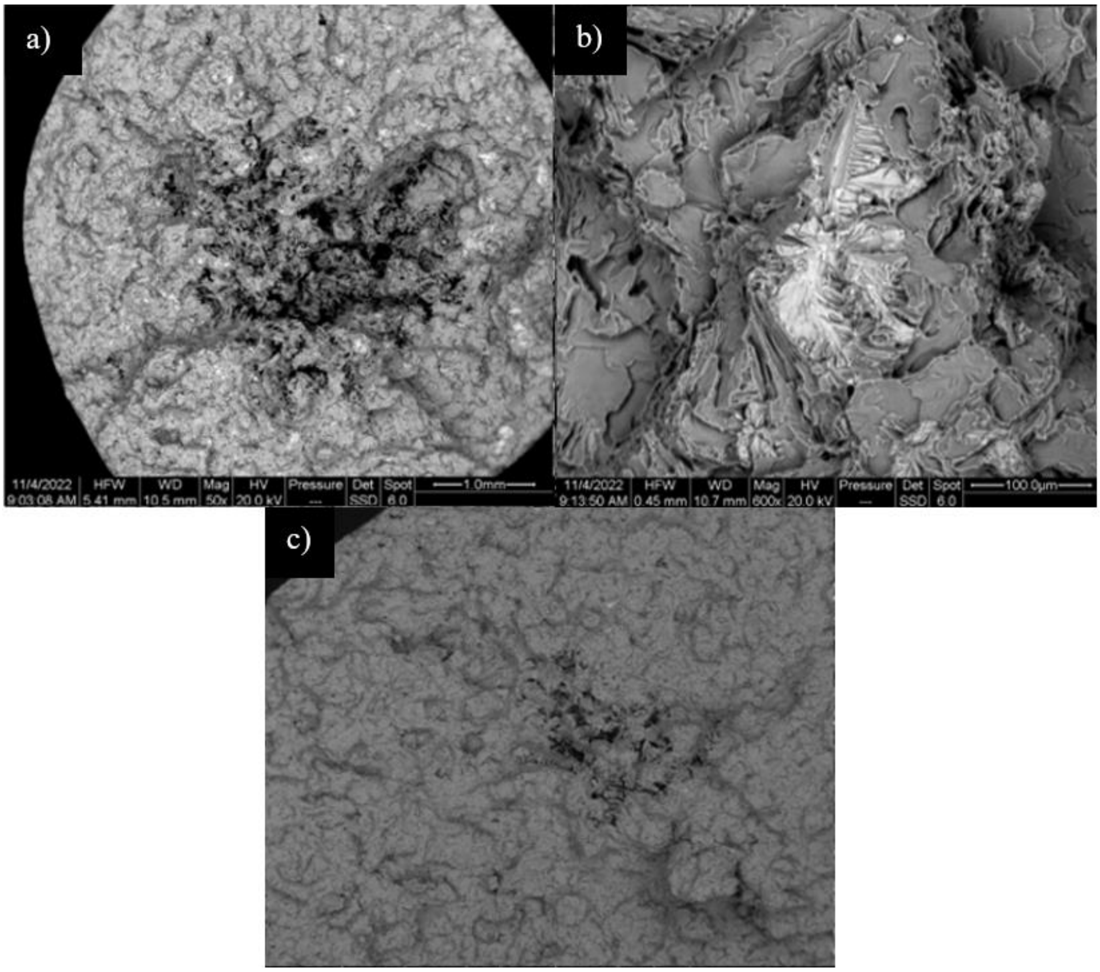

Figura 6: Ingrandimenti al SEM di: a) grossa porosità centrale nel provino IHH6; b) grosso intermetallico FeMnCr nel provino IHL6; c) Piccola porosità da ritiro nel provino IHL11

In conclusione, dall'analisi delle porosità si può concludere che:

- I parametri usati durante la fase di analisi dell'immagine sono importanti e dovrebbero sempre essere esplicitati;

- La distribuzione statistica di alcune grandezze caratteristiche dei pori è lognormale. In particolare questo è vero per l'area dei pori, il diametro di Feret dei pori, il perimetro dei pori e, di conseguenza, la rotondità dei pori;
- L'uso del Bifilm Index Specifico normalizzato alla massa del campione è raccomandato per il miglioramento della comparabilità tra dati;
- A bassi livelli di idrogeno (< 0,1 ml/100g) l'analisi della porosità per mezzo di campioni RPT e Density Index non è affidabile, in quanto nonostante le differenti condizioni e caratteristiche dei fusi essi risultano indistinguibili.
- Ad alti livelli di idrogeno (> 0,3 ml/100g) l'analisi della porosità per mezzo di campioni RPT e Density Index è risultata efficace nella distinzione dei vari tipi di fuso.
- Le operazioni di riversamento nel caso dei fusi IH hanno avuto come effetti:
    A. Un'aumento del contenuto di bifilm, introducendone di nuovi dalle dimensioni ridotte.
    B. La rottura in pezzi più piccoli dei bifilm gia presenti.

Dalle prove meccaniche e dalle analisi al SEM/EDS risulta invece che:

- Lo stampo modello Sthal non è adatto alla produzione di provini meccanici, a causa dei tempi di solidificazione scostanti, le consistenti porosità da ritiro e la natura turbolenta del suo riempimento.

APPENDIX A

RPT SAMPLES SURFACES

Appendix 1A: RPTs from melt ILL

Appendix 2A: RPTs from melt ILH

Appendix 3A: RPTs from melt SLL

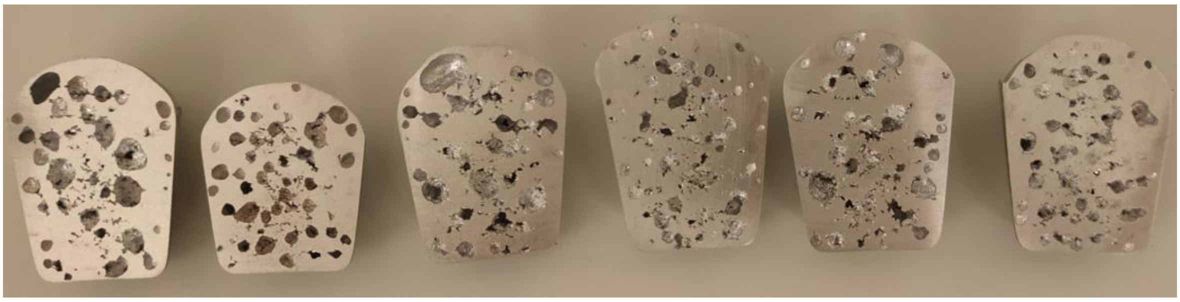

Appendix 4A: RPTs from melt SLH

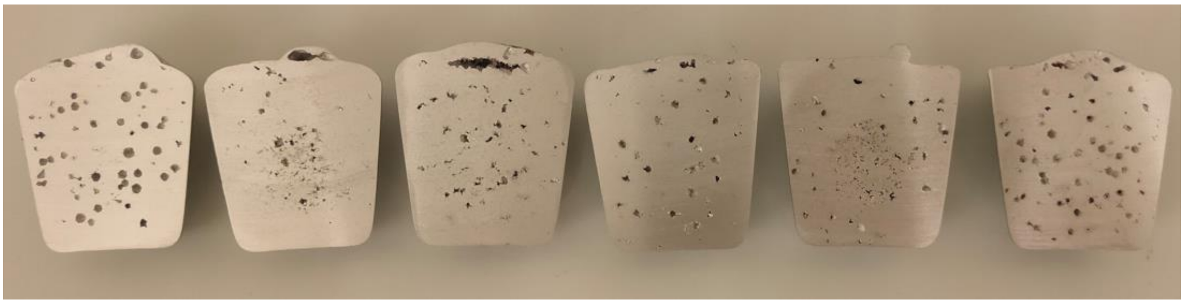

Appendix 5A: RPTs from melt IHL

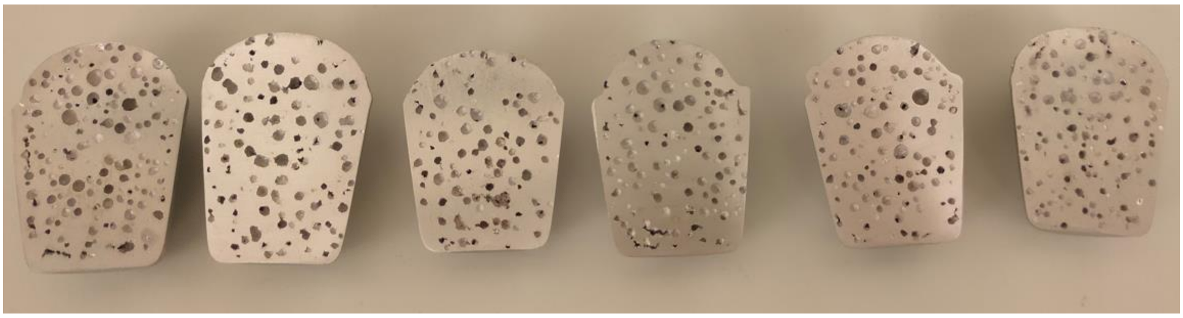

Appendix 6A: RPTs from melt IHH

Appendix 7A: Overview of all the RPT samples before the cutting operation. From left to right: ILL, ILH, SLL, SLH, IHL, IHH

APPENDIX B

ADDITIONAL GRAPHS

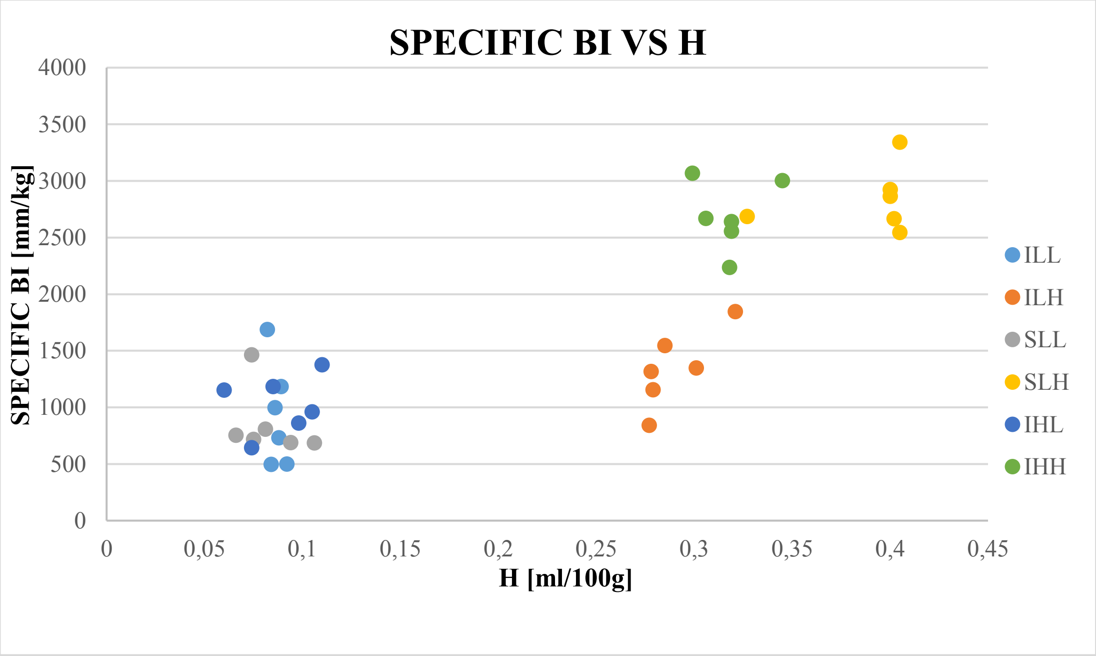

Appendix 1B: Specific BI vs H graph that shows the single RPT samples. Each melt is represented by 6 points, one for each RPT sample.

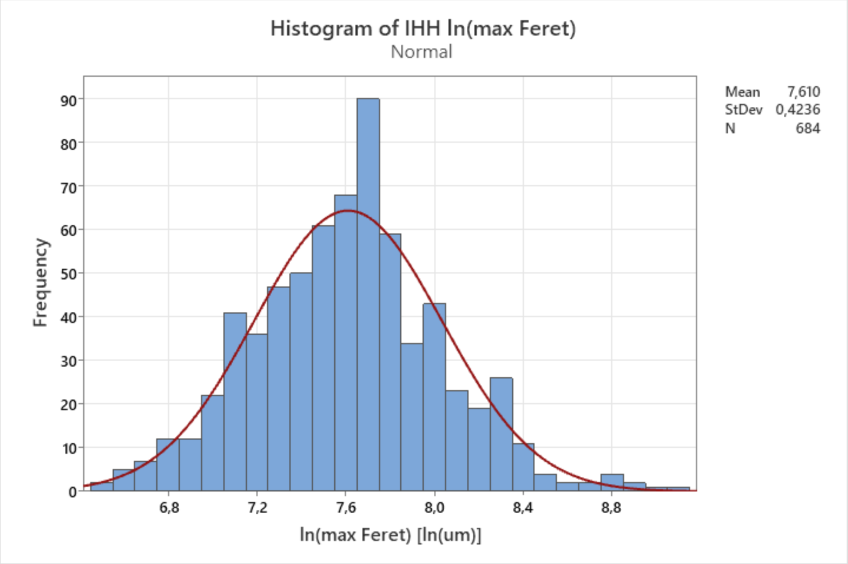

Appendix 2B: Example of distribuition of the natural logarithm of the maximum Ferets. Notice that by applying the natural logarithm, data assumes a normal distribution, confirming the lognormal nature of maximum Ferets

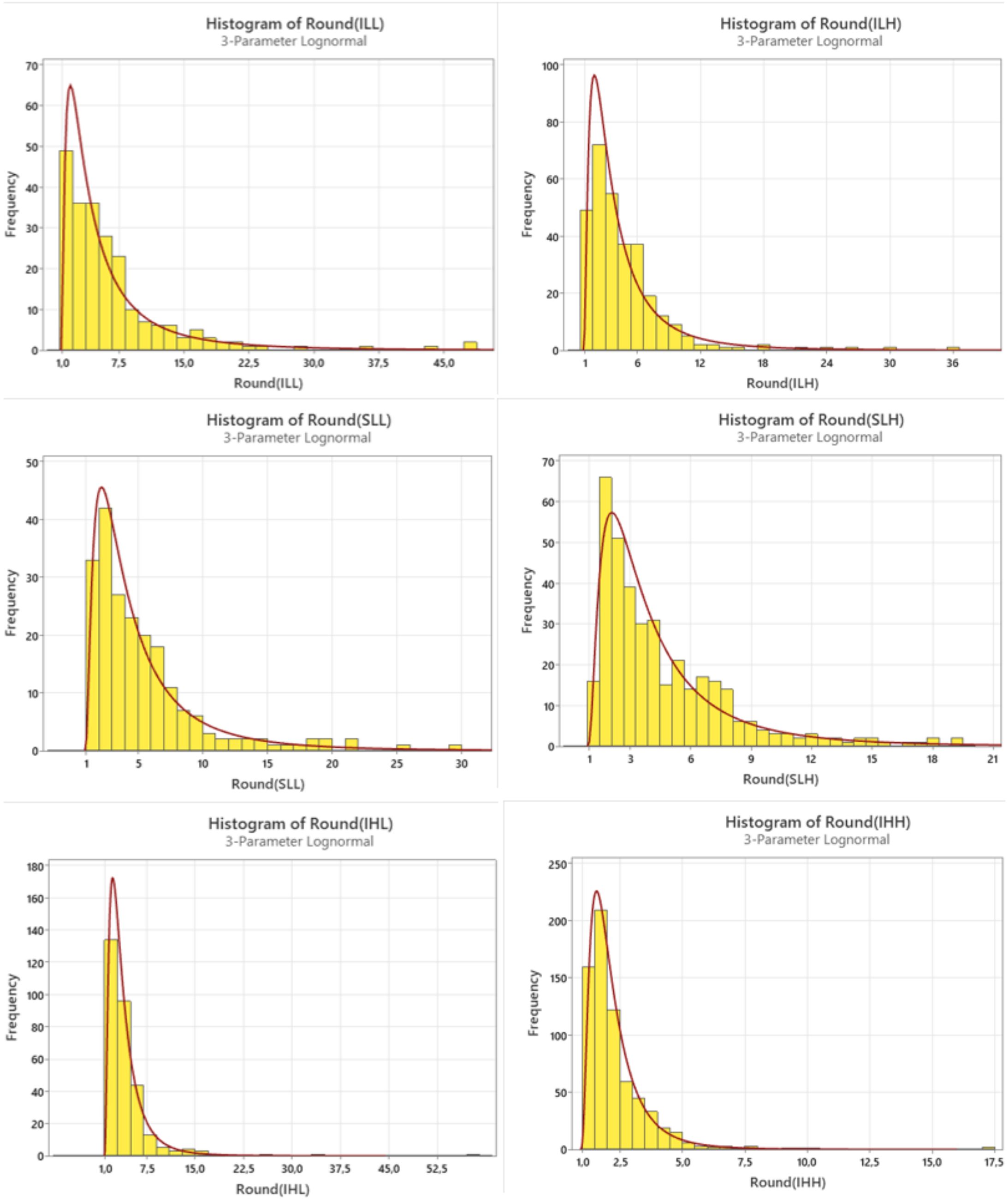

Appendix 3B: Distribution of the pore roundness of the six different melt conditions. The red curve represents the best fitting distribution, in all cases lognormal.

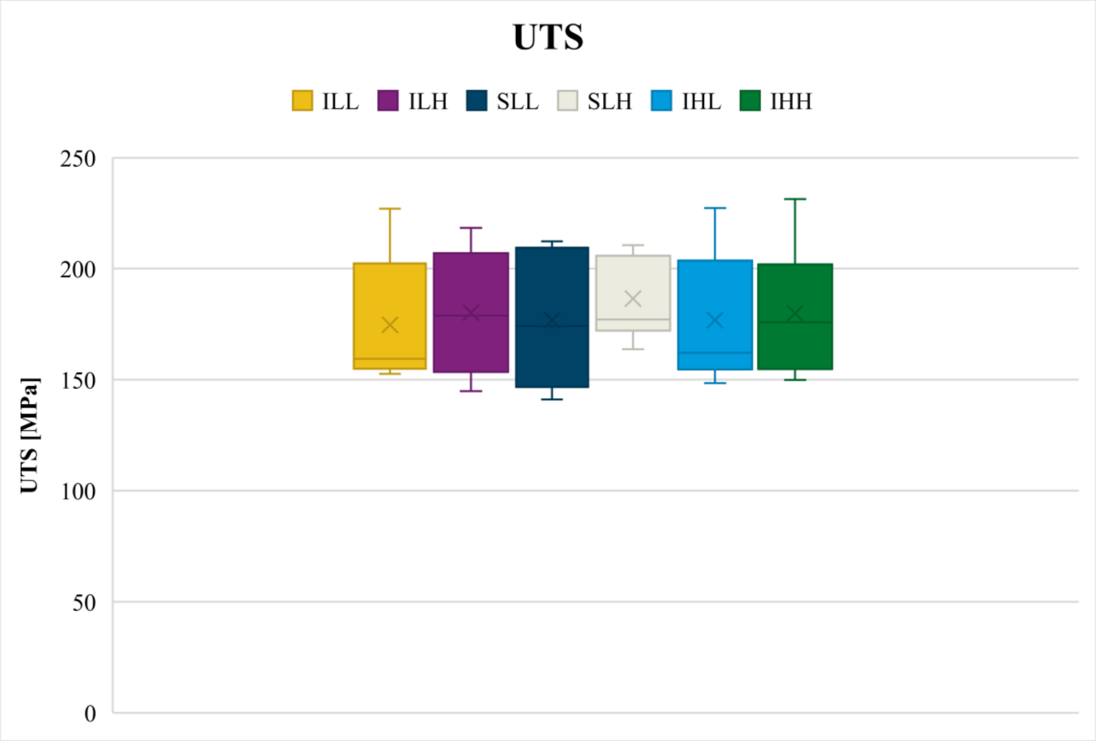

Appendix 4B: UTS results of the 6 different melt conditions without any distinction between ”n” and ”s” class. Note tboth the wide spread of data and the lack of any change in mechanical properties between different melt conditions.

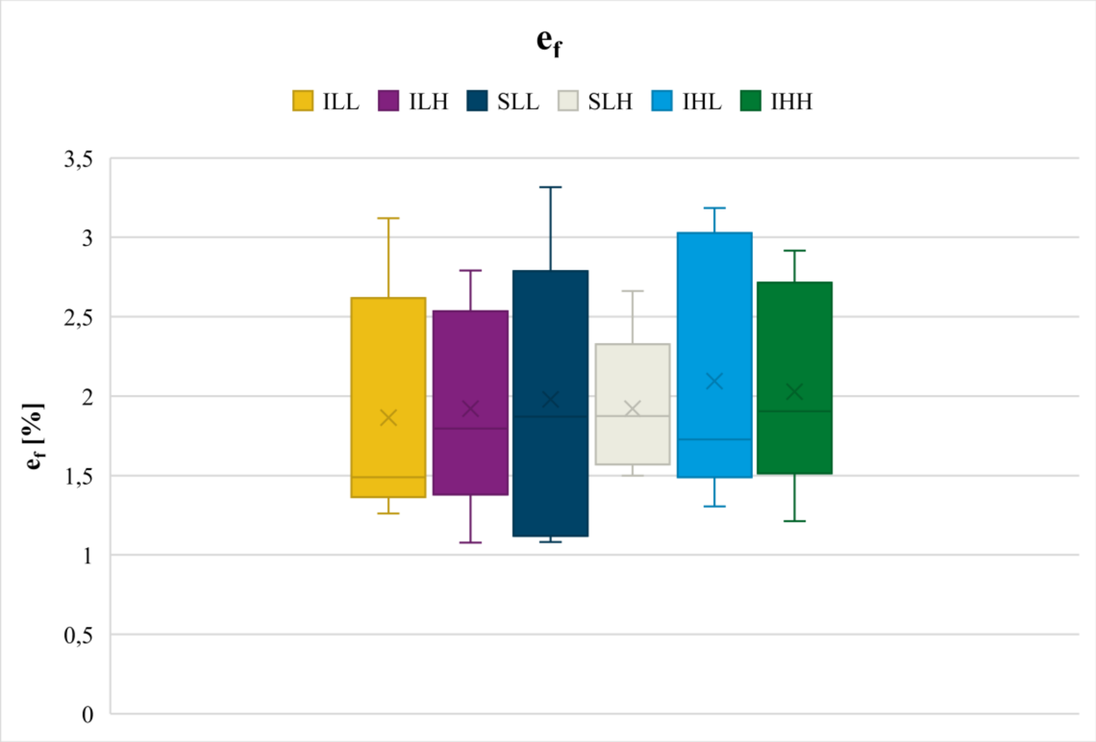

Appendix 5B: Percentage of elongation at fracture results of the 6 different melt conditions without any distinction between ”n” and ”s” class. Note tboth the wide spread of data and the lack of any change in mechanical properties between different melt conditions.

APPENDIX C

RAW DATA FROM MECHANICAL TESTS

Sample	Date/Clock time	E	Rp at 0.2% plastic strain	UTS	FBreak	e_f	d0	S0	class
		[GPa]	[MPa]	[MPa]	[N]	[%]	[mm]	[mm^2]	
ILL9	44747,63	80,79092	79,26712	155,7697	7679,636	1,260483	8,4	55,41769	s
ILL8	44747,63	74,38781	80,65884	169,4628	9222,561	1,496855	8,4	55,41769	s
ILL7	44747,63	79,32965	88,57714	227,0576	12491,73	3,120017	8,4	55,41769	s
ILL6	44747,63	79,65884	80,91161	203,2841	11084,01	2,807421	8,4	55,41769	s
ILL5	44747,48	74,45323	74,93129	152,6242	7967,264	1,37998	8,4	55,41769	n
ILL4	44747,47	73,66463	79,07491	157,7017	8226,748	1,312439	8,4	55,41769	n
ILL3	44747,47	71,73078	72,99115	153,5241	8016,409	1,440071	8,4	55,41769	n
ILL2	44747,46	76,56323	72,13529	154,6376	8156,368	1,51093	8,4	55,41769	n
ILL12	44747,64	72,02275	74,44787	157,5415	8171,759	1,482205	8,4	55,41769	n
ILL11	44747,64	79,78477	83,10566	203,0141	11038,66	2,576774	8,4	55,41769	s
ILL10	44747,64	74,58391	79,35189	160,9994	8690,158	1,359298	8,4	55,41769	s
ILL1	44747,45	71,55605	83,20826	200,5481	10927,01	2,630994	8,4	55,41769	s
ILH9	44747,65	78,16743	88,14624	205,7219	11288,11	2,256023	8,4	55,41769	s
ILH8	44747,65	78,57288	81,24606	198,0325	10612,49	2,537704	8,4	55,41769	s
ILH7	44747,65	79,87829	86,632	210,5511	11359,77	2,791684	8,4	55,41769	s
ILH6	44747,65	79,96262	87,9474	218,3398	11725,38	2,653856	8,4	55,41769	s
ILH5	44747,5	75,98229	80,6572	162,4561	8901,305	1,471426	8,4	55,41769	n
ILH4	44747,49	75,08871	75,97655	159,2164	8319,408	1,557755	8,4	55,41769	n
ILH3	44747,49	74,43037	77,82113	151,5634	8281,763	1,255453	8,4	55,41769	n
ILH2	44747,49	76,4699	70,32507	144,9088	7858,519	1,349102	8,4	55,41769	n
ILH12	44747,66	68,95816	75,92865	160,2639	8614,724	1,640561	8,4	55,41769	n
ILH11	44747,66	76,89721	79,97252	195,2417	10692,32	2,523852	8,4	55,41769	s
ILH10	44747,66	81,27577	88,03046	207,3417	11397,01	1,949831	8,4	55,41769	s
ILH1	44747,49	73,70147	78,68535	148,3837	8051,574	1,077416	8,4	55,41769	n
SLL9	44747,68	79,09505	86,05508	211,3086	11290,12	2,595128	8,4	55,41769	s
SLL8	44747,68	78,59482	79,28613	200,167	10880,04	2,849432	8,4	55,41769	s
SLL7	44747,68	73,02327	77,98549	146,5902	7671,023	1,09602	8,4	55,41769	n
SLL6	44747,68	77,09451	75,79154	142,4487	7752,023	1,08266	8,4	55,41769	n
SLL5	44747,52	74,67941	78,65655	147,1737	7773,456	1,09649	8,4	55,41769	n

SLL4	44747,51	74,1921	70,99826	141,1766	7404,753	1,212876	8,4	55,41769	n
SLL3	44747,51	80,63882	74,65962	191,5563	10516,72	3,204459	8,4	55,41769	s
SLL2	44747,51	74,22846	74,67323	156,7945	8221,206	1,489477	8,4	55,41769	n
SLL12	44747,69	78,82467	85,84785	203,9073	11117,52	2,252901	8,4	55,41769	s
SLL11	44747,69	76,71798	83,32492	212,321	11585,46	3,315365	8,4	55,41769	s
SLL10	44747,69	79,05784	86,05025	212,1288	11449,24	2,366785	8,4	55,41769	s
SLL1	44747,51	75,16974	78,5465	154,621	8442,394	1,189379	8,4	55,41769	n
SLH9	44747,7	79,28493	87,40151	201,3354	10915,59	1,905252	8,4	55,41769	s
SLH8	44747,69	78,81337	85,31465	210,5429	11552,65	2,661986	8,4	55,41769	s
SLH7	44747,69	71,33362	81,37671	167,6628	9214,858	1,500108	8,4	55,41769	n
SLH6	44747,69	79,83312	86,52669	210,1077	11584,69	2,327084	8,4	55,41769	s
SLH5	44747,59	73,76621	79,88148	172,0473	9324,001	1,613296	8,4	55,41769	n
SLH4	44747,59	75,13933	76,85155	174,3588	9015,437	1,874642	8,4	55,41769	n
SLH3	44747,59	75,36852	86,3886	177,2075	9554,449	1,591056	8,4	55,41769	n
SLH2	44747,59	74,46301	75,96263	163,6781	8909,321	1,57073	8,4	55,41769	n
SLH11	44747,7	78,36766	81,91958	194,048	10576,84	2,166109	8,4	55,41769	s
SLH10	44747,7	75,25433	81,11637	175,0548	9545,108	1,562403	8,4	55,41769	s
SLH1	44747,59	80,20245	84,51074	205,8336	10730,38	2,364535	8,4	55,41769	s
IHL9	44747,72	78,69305	76,2571	190,1612	9943,499	2,815306	8,4	55,41769	s
IHL8	44747,71	80,14044	88,7286	227,3523	12347,53	3,137547	8,4	55,41769	s
IHL7	44747,7	76,27244	84,3481	154,5308	7975,905	1,474125	8,4	55,41769	n
IHL6	44747,7	76,20074	80,80869	148,4994	8017,42	1,305121	8,4	55,41769	n
IHL5	44747,61	76,93778	76,44976	155,3459	8091,358	1,355735	8,4	55,41769	n
IHL4	44747,6	74,39056	73,91487	158,6352	8485,411	1,620764	8,4	55,41769	n
IHL3	44747,6	75,17526	73,9702	162,7536	8696,605	1,600122	8,4	55,41769	n
IHL2	44747,6	75,28149	72,18006	152,8615	8357,271	1,537415	8,4	55,41769	n
IHL12	44747,72	78,43095	89,33534	205,538	10869,79	2,18551	8,4	55,41769	s
IHL11	44747,72	79,50352	82,85524	204,8274	11041,5	3,098093	8,4	55,41769	s
IHL10	44747,72	79,75566	77,93175	200,2679	10972,07	3,184539	8,4	55,41769	s
IHL1	44747,6	73,37998	71,68967	161,5739	8643,35	1,832558	8,4	55,41769	n
IHH9	44747,73	79,77686	88,20761	219,7309	12031,93	2,916192	8,4	55,41769	s
IHH8	44747,73	74,70564	80,12227	176,4453	9663,011	1,711449	8,4	55,41769	s
IHH7	44747,73	78,45805	75,56461	175,1142	9238,967	2,143361	8,4	55,41769	n
IHH6	44747,72	71,04023	73,15362	160,6136	8280,7	1,695061	8,4	55,41769	n
IHH5	44747,62	70,18506	74,23304	154,9783	8212,822	1,494951	8,4	55,41769	n
IHH4	44747,61	66,48348	73,24535	154,7101	8149,024	1,56856	8,4	55,41769	n
IHH3	44747,61	78,21248	81,1834	185,1373	9735,974	2,098598	8,4	55,41769	s
IHH2	44747,61	75,21557	76,35958	154,3059	8362,588	1,391541	8,4	55,41769	n
IHH12	44747,74	82,50977	112,777	231,3545	12474,5	2,827402	8,4	55,41769	s
IHH11	44747,75	78,17927	79,84275	191,1285	10335,57	2,487482	8,4	55,41769	s
IHH10	44747,73	82,17659	84,88751	205,5023	11155,78	2,7901	8,4	55,41769	s
IHH1	44747,61	77,20435	77,08363	149,9635	8104,576	1,21206	8,4	55,41769	n

APPENDIX D

RPT SAMPLES PORE DESCRIPTORS AND VARIABLES

SAMPLE	***Pore area (sum)***	***Pore area (avg)***	***Max Feret (avg)***	***BI***	***Perimeter (avg)***	***Section Surface***	***Mass***	***SpBI***	***[H]***	***Sampling T***	***Round. (avg)***	***N° of Pores***
	[mm^2]	***[mm^2]***	***[mm]***	***[mm]***	***[mm]***	***[mm^2]***	***[g]***	***[mm/kg]***	***[ml/100g]***	***[°C]***		
ILL1	38,9421	1,4978	1,7519	45,5489	10,170	1496,001	91,36	498,565	0,092	700	5,4954	26
ILL2	107,2995	2,1898	2,2583	110,6579	12,217	1592,146	93,42	1184,52	0,089	699	5,4238	49
ILL3	61,4484	2,0483	2,3581	70,7431	14,261	1570,915	96,75	731,1948	0,088	702	7,9018	30
ILL4	115,5432	3,1228	2,7287	100,9633	14,571	1700,482	101,28	996,873	0,086	704	5,4103	37
ILL5	32,9627	1,4983	2,0890	45,9587	9,880	1510,299	92,48	496,9583	0,084	701	5,1847	22
ILL6	186,2957	3,1576	2,9718	175,3349	12,816	1810,552	103,9	1687,535	0,082	703	4,1392	59
ILH1	272,6206	4,0091	2,9177	198,4033	11,967	1908,912	107,53	1845,097	0,321	706	2,8425	69
ILH2	126,8985	2,2660	2,3097	129,341	10,419	1650,801	96,02	1347,021	0,301	705	3,8120	56
ILH3	238,9494	4,7790	3,3358	166,7877	14,016	1942,600	107,92	1545,475	0,285	705	3,2711	50
ILH4	100,4005	1,9308	2,0868	108,5149	8,920	1573,168	93,77	1157,245	0,279	703	3,2791	52
ILH5	147,2648	2,9453	2,4404	122,0222	11,923	1652,651	92,7	1316,313	0,278	704	3,8410	50
ILH6	65,5214	2,1136	2,4510	75,9814	11,357	1497,432	90,33	841,1535	0,277	704	4,8559	31
SLL1	39,9260	1,1407	1,7926	62,7399	8,501	1429,205	83,3	753,1801	0,066	702	5,0407	35
SLL2	121,8825	2,2571	2,3863	128,8585	11,067	1593,357	88,06	1463,303	0,074	702	4,3179	54
SLL3	22,9410	0,9559	1,7272	41,4525	7,935	926,112	57,7	718,4142	0,075	702	5,2424	24
SLL4	48,7870	1,3186	1,9577	72,4334	8,930	1511,041	89,54	808,9502	0,081	701	4,8131	37
SLL5	39,2206	1,1885	1,9028	62,7918	8,032	1525,860	91,11	689,1867	0,094	702	4,3195	33
SLL6	37,9702	1,4604	1,7470	45,422	6,980	1249,632	66,31	684,9947	0,106	700	2,6552	26
SLH1	546,2375	9,4179	3,8895	225,5907	16,715	1837,651	84,01	2685,284	0,327	696	2,3608	57
SLH2	399,8213	5,8797	3,2880	223,5809	14,230	1534,857	66,87	3343,516	0,405	700	2,7405	68
SLH3	571,3611	10,3884	4,2432	233,3766	17,095	1806,780	79,85	2922,688	0,4	702	2,2386	55
SLH4	420,7560	4,6751	3,0572	275,1445	14,090	1647,990	96,07	2864	0,4	702	3,3791	90
SLH5	539,7916	9,8144	4,1635	228,9922	20,376	1843,998	85,87	2666,731	0,402	704	3,3665	55
SLH6	411,6194	8,7579	4,4886	210,9628	21,152	1787,245	82,9	2544,786	0,405	704	4,0653	47

IHL1	107,4858	2,0280	1,9797	104,9236	7,690	1595,058	90,93	1153,894	0,06	704	2,3206	54
IHL2	31,2916	0,7277	1,3639	58,6475	6,397	1564,277	91,14	643,488	0,074	701	4,4746	43
IHL3	95,7306	1,8062	2,1372	113,2739	9,066	1621,631	95,75	1183,017	0,085	699	3,6208	53
IHL4	67,7915	1,7382	2,0697	80,7187	8,657	1575,067	93,68	861,6428	0,098	700	3,4311	39
IHL5	55,2282	1,0829	1,7169	87,563	6,382	1570,034	91,27	959,3842	0,105	700	2,9929	51
IHL6	105,1971	1,6184	1,8995	123,4675	7,428	1568,366	89,62	1377,678	0,11	700	2,7126	65
IHH1	359,4641	2,6431	2,1306	289,7649	7,439	1662,317	96,49	3003,056	0,345	699	1,6660	136
IHH2	292,0346	2,9498	2,3365	231,316	8,760	1696,184	103,43	2236,45	0,318	698	2,0703	99
IHH3	285,9404	3,2867	2,5066	218,0775	9,602	1736,695	85,3	2556,594	0,319	702	2,2322	87
IHH4	301,2197	2,7635	2,1950	239,2582	7,678	1550,146	90,62	2640,236	0,319	703	1,6976	109
IHH5	309,7694	2,5391	2,0236	246,8735	7,119	1558,643	92,45	2670,346	0,306	702	1,5885	122
IHH6	362,7890	2,7694	2,2149	290,157	8,486	1867,472	94,62	3066,55	0,299	700	2,0690	131

REFERENCES

[1] J. Lindell, "What Is the Most Abundant Metal on Earth?" sciencing.com, https://sciencing.com/what-abundant-metal-earth-4587197.html. 14 April 2022.

[2] http://www.indexmundi.com/en/commodities/minerals/bauxite_and_alumina

[3] ASM international. (1992). ”Metals Handbook” Vol.2, ASM international

[4] G. M. Scamans, N. Birbilis, R. G. Buchheit, “Corrosion of Aluminum and its Alloys”, Shreir`s Corrosion, 2010 Elsevier B.V.

[5] NDT Supply Inc., “Conductivity and Resistivity Values for Aluminum & Alloys”, March 2002

[6] M. A. Laughton, D.F. Warne, “Electrical Engineer's Reference Book”, 16th Edition - September 27, 2002

[7] https://peakdemand.com/types-of-conductors-used-in-overhead-power-lines

[8] J. Carvill, “Mechanical Engineer's Data Handbook”, 1st Edition - January 1, 1994

[9] European Aluminum Association, Designation System, 2002

[10] ASM international. (1992). ”Metals Handbook” Vol.9, ASM international

[11] sabna.com/us/en/education/blog/understanding-the-aluminum-alloy-designation-system.cfm

[12] https://www.european-aluminium.eu/about-aluminium/aluminium-in-use/automotive-and-transport

[13] A. L. Juan, G. V. Voort. "The Al-Si Phase Diagram." Tech notes 5 (2009): 5.

[14] https://www.engineeringtoolbox.com/fusion-heat-metals-d_1266.html

[15] https://www.britannica.com/science/silicon

[16] V. Kumar, H. Mehdi, A. Kumar, “Effect of Silicon Content on the Mechanical Properties of Aluminum Alloy”, Int. Res. J. of En. and Tech.Vol.2 Issue 04, pp 1326-1330, 2015

[17] A. Hekmat-Ardakan, X. Liu, F. Ajersch, X. G. Chen, "Wear behavior of hypereutectic Al-Si-Cu-Mg casting alloys with variable Mg conents", Wear Vol.269, pp 684-692, 2010

[18] M. Warmuzek, "Aluminum-Silicon casting alloys", Atlas of Microfractographs, 2004

[19] J. Campbell, "Complete Casting Handbook", Butterworth-Heinmann, 2nd Edition, 2015

[20] D. V. Ragone, "Some Factors Affecting Fluidity", Submission in Partial Fulfillment of the Requirements for the Degree of Doctor of Science at the M.I.T., 1953

[21] G. Lang, Aluminum, Vol. 48(10), pp 664-672

[22] Lecture notes by G. Timelli from the course of "Ironmaking and Steelmaking at the University of Padova.

[23] M. Tiryakioglu, "The Effects of Hydrogen on Pore Formation in Aluminum Alloy Castings: Myth Versus Reality", Metals 10, 368, 2020

[24] M. Tiryakioglu, P. Yousefian, "Pore Formation During Solidification of Aluminum: Reconciliation of Experimental Observations, Modeling Assumptions, and Classical Nucleation Theory" Metallurgical and Materials Transactions A, Vol. 49 A, pp 563-575, 2018

[25] M. Tiryakioglu, "The myth of hydrogen pores in aluminum castings", in "Shape Casting: 7th International Symposium Celebrating Prof. John Campbell's 80th Birthday" by M. Tiryakioglu, W. Griffiths, M. Jolly, Springer, pp. 143-150, 2019

[26] S. Lin, "A study of hot tearing in wrought Aluminum alloys", Université du Québec à Chicoutimi (UQAC), PhD Thesis, 1999

[27] M. Uludag, R. Cetin, D. Dispinar, "Bifilms and Hot Teraing of Al-Si Alloys", in "Shape Casting: 6th International Symposium" by M. Tiryakioglu, G. Byezynsk, M. Jolly, Springer, pp. 13-19, 2016

[28] J. Campbell, "Entrainment Defects", Materials Science and Technology, 2013

[29] J. Campbell, "Melting, Remelting, and Casting for Clean Steel", Steel Research, Vol.88 Issue 1, 2016

[30] U.S. Department of Energy, “Reaction of Aluminum with Water to Produce Hydrogen: A Study of Issues Related to the Use of Aluminum for On-Board Vehicular Hydrogen Storage”, pp 1-26, 2008

[31] J. Zhang, H. Matsuura, F. Tsukihashi, “Treatsie on Process Metallurgy”, Vol. 3: Indutrial Processes, Elsevier, 2014

[32] Y. Wang, HT. Li, Z. Fan, “Oxidation of Aluminum Alloy Melts and Inoculation by Oxide Particles, Trans Indian Inst Met, Vol. 65, pp 653-661, 2012

[33] R. Raiszadeh, W. D. Griffiths, “A Method to Study the History of a Double Oxide Film Defect in Liquid Aluminum Alloys”, Metallurgical and Materials Transactions B, Vol. 37, pp 865-871, 2006

[34] W. D. Griffiths, R. Raiszadeh, “Hydrogen, Porosity and Oxide Film Defects in Liquid Al”, J. Mater. Sci., Vol. 44, pp 3402-3407, 2009

[35] C. Nyahumwa, N. R. Green and J. Campbell, AFS Trans., Vol. 58, 1998

[36] J. Campbell, “An Overview of the Effects of Bifilms on the Structure and Properties of Cast Alloys”, Metallurgical and Materials Transactions B, Vol. 37, pp 857-863, 2006

[37] P. Yousefian, M. Tiryakioglu, “Pore Formation During Solidification of Aluminum: Reconciliation of Experimental Observations, Modeling Assumptions and Classical Nucleation Theory”, Metall. Mater. Trans. A, Vol. 49, pp 563-575, 2018

[38] J. Campbell, “Stop Pouring, Start Casting”, Hoyt Memorial Lecture for American Foundry Society, International Journal of Metalcasting, Vol. 6, pp 7-18, 2012

[39] J. Campbell, “Castings, The New Metallurgy of Cast Metals”, 2nd Edition, Butterworth-Heinemann, 2003

[40] M. Sadayappan, M. Sahoo, G. Liao, B. J. Yang, D. Li, R. W. Smith (2001). TAFS, Vol.109, pp 341-352.

[41] J. L. Dion, E. A. Fasoyinu, D. Cousineau, C. Bibby, M. Sahoo (1995). TAFS, Vol. 103, pp 367-377.

[42] https://www.britannica.com/science/viscosity

[43] G. Timelli, F. Bonollo, “Fluidity of Aluminum Die Castings Alloy”, International Journal of Cast Metals Research, Vol. 20, pp 304-311, 2007

[44] L. Battezzati, A. L. Greer, “The Viscosity of Liquid Metals and Alloys”, Acta. metall. Vol. 37, No. 7, pp 1791-1802, 1988

[45] M. C. Flemings, “Solidification processing”, McGraw–Hill, 1974

[46] İ. G. Hızlı, M. Salkır, İ. H. Kalkan, D. Dışpınar “Influence of Melt Quality on the Fluidity of AlSi12Fe”, The Minerals, Metals & Materials Society, pp 373-379, 2019

[47] J. Campbell, “An Overview of the Effects of Bifilms on the Structure and Properties of Cast Alloys”, Metallurgical and Materials Transactions B, Vol. 37, pp 857-863, 2006

[48] J. Mi, R. A. Harding, J. Campbell, Int. J. Cast Met. Res., Vol. 14, 2002

[49] N. Hansen, “Hall–Petch Relation and Boundary Strengthening”, Scripta Materialia, Vol. 51, pp 801-806, 2004

[50] W. E. Sicha, R. C. Boehm, TAFS, Vol. 56, 1948

[51] E. N. Pan, M. W. Hsieh, S. S. Jang, C. R. Loper, TAFS, Vol. 97, 1989

[52] Y. Birol, “Impact of Grain Size on Mechanical Properties of AlSi7Mg0.3 Alloy”, Materials Science and Engineering, Vol. 559 A, pp 394-400, 2013

[53] E. Samuel, B. Golbahar, A. M. Samuel, H. W. Doty, S. Valtierra, F. H. Samuel, “Effect of Grain Refiner on the Tensile and Impact Properties of Al-Si-Mg Cast Alloys”, Materials & Design, Vol. 56, pp 468-479, 2014

[54] E. Ghassemali, M. Riesta, T. Bogdanoff, B. S. Kumar, S. Seiffedine, “Hall-Petch Equation in a Hypoeutectic Al-Si Cast Alloy: Grain Size vs. Secondary Dendrite Arm Spacing”, International Conference on the Technology of Plasticity, Vol. 207, pp 19-24, 2017

[55] S. A. Kori, B. S. Murty, M. Chakraborty, “Development of An Efficient Grain Refiner for Al–7Si Alloy and its Modification With Strontium”, Materials science and engineering, Vol. 238 A, pp 94-104, 2000

[56] K.G. Basavakumar, P.G. Mukunda, M. Chakraborty, “Influence of Grain Refinement and Modification on Microstructure and Mechanical Properties of Al–7Si and Al–7Si–2.5Cu Cast Alloys”, Materials Characterization, Vol. 59, 2008

[57] R. K. Yajjala, N. M. Inampudi, B. R. Jinugu, “Correlation Between SDAS and Mechanical Properties of Al-Si Alloy Made in Sand and Slag Moulds”, Journal of Materials Research and Technology, Vol. 9, pp 6257-6267, 2020

[58] M. Zamani, S. Seifeddine, A. E. W. Jarfors, “High Temperature Tensile Deformation Behavior and Failure Mechanisms of an Al-Si-Cu-Mg Cast Alloy: The Microstructural Scale Effect”, Materials and Design, Vol. 86, pp 361-370, 2015

[59] M. Tiryakioglu, J. Campbell, N. D. Alexopoulous “On the Ductility of Cast Al-7 Pct Si-Mg Alloys”, Metallurgical and Materials Transactions A, Vol. 40, pp 1000-1007, 2009

[60] K. Al-Helal, Y. Wang, I. Stone, Z. Fan, “Effect of Ca Level on the Formation of Silicon Phases During Solidification of Hypereutectic Al-Si Alloys”, Materials Science Forum, Vol. 765, pp 117-122, 2013

[61] G. K. Sigworth, “The Modification of Al-Si Casting Alloys: Important Practical and Theoretical Aspects”, International Journal of Metalcasting, Vol. 2, pp 19-40, 2008

[62] J. Campbell, M. Tiryakioglu, “Review of Effect of P and Sr on Modification and Porosity Development in Al-Si Alloys”, Materials Science and Technology, Vol. 26, pp 262-268, 2010

[63] J. Campbell, “Modification of Al-Si Alloys”, American Foundry Society, 2011

[64] M. Tebibi, A. M. Samuel, F. Ajersch, “Effect of P and Sr additions on the microstructure of hypereutectic Al-15Si-14Mg-4Cu alloy”, Materials Characterization, Vol. 89, pp 112-123, 2014

[65] M. Tiryakioglu, “Intrinsic and Extrinsic Effects of Microstructure on Properties in Cast Al Alloys”, Materials, Vol. 13, 2020

[66] Z. Zang, X. Biang, X. Liu, “Effect of Strontium Addition on Hydrogen Content and Porosity Shape of Al-Si alloys”, International Journal of Cast Metals Research, Vol. 14, pp 31-35, 2001

[67] M. Uludag, R. Cetin, D. Dispinar, M. Tiryakioglu, "Characterization of the Effect of Melt Treatments on Melt Quality in Al-7wt%Si-Mg Alloys", Metals, Vol. 7, 2017

[68] M. Uludag, R. Cetin, D. Dispinar, M. Tiryakioglu, "On the Interpretation of Melt Quality Assessment of A356 Aluminum Alloy by the Reduced Pressure Test: The Bifilm Index and its Physical Meaning", International Journal of Metalcasting, Vol. 12, pp 853-860, 2018

[69] Technical Forum, Reader & Author Dialogue on "The Modification of Al-Si Casting Alloys: Important Practical and Theoretical Aspects" between J. Campbell and G. Sigworth, International Journal of Metalcasting, 2009

[70] D. Dispinar, J. Campbell, "A Comparison of Methods Used to Assess Aluminum Melt Quality", Shape Casting: 2nd International Symposium, 2007

[71] M. Tiryakioglu, J. Campbell, N. D. Alexopoulos, "Quality Indices for Aluminum Alloy Castings: A Critical Review", Metallurgical and Materials Transactions B, Vol. 40, pp 802-811, 2009

[72] D. Doutre, R. I. L. Guthrie: U. S. Patent 4,555,662, 1985

[73] M. Li, R. I. L. Guthrie, "On the Detection and Selective Separation of Inclusions in Liquid Metal Cleanliness Analyzer (LiMCA) Systems", Metallurgical and Materials Transactions B, Vol. 31, pp 2153-2185, 2000

[74] M. Li, R. I. L. Guthrie, "Liquid Metal Cleanliness Analyzer (LiMCA) in Molten Aluminum", ISIJ International, Vol. 41, No. 2, pp 101-110, 2001

[75] G. K. Sigworth, E. M. Williams, D. C. Chesonis, "Gas Fluxing of Molten Aluminum: An overview", Light Metals, 2008

[76] X. Cao, "Mechanisms of Pressure Filtration of Liquid Aluminum Alloys", Metallurgical and Materials Transactions B, Vol. 37, pp 1075-1083, 2007

[77] C. Stanica, P. Moldovan, "Aluminum Melt Cleanliness Performance Evaluation Using PoDFA (Porous Disk Filtration Apparatus) Technology", U. P. B. Sci. Bull., Series B, Vol. 71, pp 107-114, 2009

[78] P. Moldovan, "Researches Concerning PoDFA Method for 5083 Alloys", Proceedings of the 12th International Conference on Aluminum Alloys, September 5-9, 2010

[79] R. Gallo, “Cleaner Aluminum Melts in Foundries: A Critical Review and Update”, ASF Transactions, Vol. 116, pp 195-220, 2003

[80] A. M. Samuel, F. H. Samuel, “The Reduced Pressure Test as a Measuring Tool in the Evaluation of Porosity/Hydrogen Content in AI-7 Wt pct Si-10 Vol pct SiC(p) Metal Matrix Composite”, Metallurgical Transactions A, Vol. 23, pp 1857-1868, 1993

[81] W. Rasmussen and C.E. Eckert, “Modern Casting”, 1992

[82] D. Dispinar, J. Campbell, “Use of Bifilm Index as an Assessment of Liquid Metal Quality”, International Journal of Cast Metals Research, Vol. 19, pp 5-17, 2006

[83] H. S. Jang, H. J. Kang, G. H. Lee, P. H. Yoon, J. Y. Park et al., “Effect of Gas Bubbling Filtration Treatment Conditions on Melt Quality of AlSiMgCu Alloy”, Metals, Vol. 11, pp 841, 2021

[84] D. Dispinar, J. Campbell, “Critical Assessment of Reduced Pressure Test. Part 1: Porosity Phenomena”, International Journal of Cast Metals Research, Vol. 17, pp 280-287, 2004

[85] S. Impey, D. Stephenson, J. Nicholls, “International conference on the microscopy of oxidation”, Inst of Metals, Cambridge University, 1990

[86] E. A. Brandesand, G. B. Brooks, “Smithells Metals Reference Book”, 7th edition, Butterworth-Heinemann, Oxford, 1999

[87] C. Nyahumwa, N. R. Green, J. Campbell, “Effect of Mold-Filling Turbulence on Fatigue Properties of Cast Aluminum Alloys”, Transactions of the American Foundrymen's Society, Vol. 106, pp 215-224, 1998

[88] C. Nyahumwa, N. R. Green, J. Campbell, “Influence of Casting Technique and Hot Isostatic Pressing on the Fatigue of an Al-7Si-Mg Alloy”, Metallurgical and Materials Transactions A, Vol. 32, pp 349-358, 2001

[89] M. Aryafar, R. Raiszadeh, A. Shalbafzadeh, “Healing of Double Oxide Film Defects in A356 Aluminum Melt”, J Mater Sci, Vol. 45, pp 3041-3051, 2010

[90] S. Ji, W. Yang, F. Gao, D. Watson, Z. Fan, “Effect of Iron on the Microstructure and Mechanical Property of Al–Mg–Si–Mn and Al–Mg–Si

Diecast Alloys”, Materials Science & Engineering A, Vol. 564, pp 130-139, 2013

[91] X. Cao, J. Campbell, “Precipitation of Primary Intermetallic Compounds in Liquid Al 11.5Si 0.4Mg Alloy”, International Journal of Cast Metals Research, Vol. 13, pp. 175-184, 2000

[92] X. Cao, J. Campbell, “The Nucleation of Fe-Rich Phases on Oxide Films in Al-11.5-0.4Mg Cast Alloys”, Metallurgical and Materials Transactions A, Vol.34, pp 1409-1420, 2003

[93] S. G. Shabestari, M. Mahmudi, M. Emamy, J. Campbell, ”Effect of Mn and Sr on Intermetallics in Fe-Rich Eutectic Al-Si Alloy”, International Journal of Cast Metals Research, Vol. 15, pp 17-24, 2002

[94] A. Ahmadpour, R. Raiszadeh, H. Doostmohammadi, “Effect of Stirring on Behavior of Double Oxide Film Defects in A356 Aluminum Melt”, International Journal of Cast Metal Research, Vol. 27, pp 221-229, 2014

[95] H. Bagherpour-Torghabeh, R. Raiszadeh, H. Doostmohammadi, “Role of Mechanical Stirring of Al-Mg Melt in the Healing of Bifilm Defects”, Metallurgical and Materials Transactions B, Vol. 48, pp 3174-3184, 2017

[96] R. Raiszadeh, W. D. Griffith, “The Behavior of Double Oxide Film Defecta in Liquid Al Alloys Under Atmospheric and Reduced Pressure”, Journal of Alloys and Compounds, Vol. 491, pp 575-580, 2010

[97] M. A. El-Sayed, H. A. G. Salem, A. Y. Kanedil, W. D. Griffith, “Effect of Holding Time Before Solidification on Double-Oxide Film Defects and Mechanical Properties of Aluminum Alloys”, Metallurgical and Materials Transactions B, Vol. 42, pp 1104-1109, 2011

[98] F. H. Basuny, M. A. El-Sayed, “The Effect of Holding Time Before Solidification on the Properties of Aluminium Castings”, Journal of the Southern African Institute of Mining and Metallurgy, Vol. 108, N.8, pp 461-466, 2020

[99] S. Yasa, A. Kabil, Y. Bayrak, M. Cigdem, “The Effect of Holding Time After Sr Addition on Microstructural and Mechanical Properties of A356 Alloy”, Pamukkale Univ Muh Bilim Derg, Vol. 26, pp 634-637, 2020

[100] M. Uludag, R. Cetin, L. Gemi, D. Dispinar, “Change in Porosity of A356 by Holding Time and Its Effect on Mechanical Properties”, Journal of Materials Engineering and Performance, Vol. 27, pp 5141–5151, 2018

[101] D. Dispinar, J. Campbell, “Effect of Casting Conditions on Aluminum Metal Quality”, Journal of Materials Processing Technology, Vol. 182, pp 405-410, 2006

[102] G. Reng-Guo, T. Di, “A Review on Grain Refinement of Aluminum Alloys: Progresses, Challenges and Prospects”, Acta Metall. Sin., Vol. 30, pp 409-432, 2017

[103] C. Limmaneevichitr, W. Eidhed, “Fading Mechanism of Grain Refinement of Aluminum/Slicon Alloy With Al/Ti/B Grain Refiners”, Materials Science and Engineering A, Vol. 349, pp 197-203, 2003

[104] P. L. Schaffer, A. K. Dahle ”Settling Behaviour of Different Grain Refiners in Aluminium”, Materials Science and Engineering A, Vol. 414, pp 373-378, 2005

[105] Ö. Gürsoy, E. Erzi, D. Dışpınar, ”Ti Grain Refinement Myth and Cleanliness of A356 Melt”, in “Shape Casting: 7th International Symposium Celebrating Prof. John Campbell’s 80th Birthday” by M. Tiryakioglu, W. Griffiths, M. Jolly, Springer, pp. 125-130, 2019

[106] C. Yuksel, O. Tamer, E. Erzi, U. Aybarc, E. Cubuklusu, O. Topcuoglu, M. Cigdem, D. Dispinar, ”Quality Evaluation of Remelted A356 Scraps”, Archives of Fonundry Engineering, Vol. 16, pp 632-640, 2016

[107] T. Ludwig, M. Di Sabatino, L. Arnberg, ”Influence of Oxide Additions on the Porosity Development and Mechanical Properties of A356 Aluminum Alloy Castings”, International Journal of Metalcasting, Vol. 6, pp 41-50, 2012

[108] M. Kang, E. Lee, ” Effect of Bifilm Defects on Microstructure and Tensile Properties of A356 Secondary Alloy for the Recycling of Machining Chip Scrap”, Journal of Advanced Marine Engineering and Technology, Vol.45, pp 356-362, 2021

[109] “Electric and Plug-in Hybrid Electric Vehicles Roadmap” Report by the International Energy Agency, Redacted in 2010

[110] H. Hatayama, I. Daigo, Y. Matsuno, Y. Adachi, “Evolution of Aluminum Recycling Initiated by the Introduction of Next-Generation Vehicles and Scrap Sorting Technology”, Resources, Conservation and Recycling, Vol. 66, pp 8-14, 2012

[111] H. V. Atkinson, S. Davies, “Fundamental Aspects of Hot Isostatic Pressing: an Overview”, Metallurgical and Materials Transactions A, Vol. 31, pp 2981–3000, 2000

[112] D. F. Heaney, C. Binet, “Hot Isostatic Pressing (HIP) of Metal Injection Molding (MIM)”, Handbook of Metal Injection Molding, Elsevier Ltd., 2019

[113] G. Ran, J. Zhou, Q. G. Wang, ”The Effect of Hot Isostatic Pressing on the Microstructure and Tensile Properties of an Unmodified A356-T6 Cast Aluminum Alloy”, Journal of Alloys and Compounds, Vol.421, pp 80-86, 2006

[114] From the seminar ”Manage the Damage: A Holistic Approach to Metal Quality” by M. Tiryakioglu, 02 Dec 2021 for Jonkoping Tekniska Hogskolan

[115] T. M. Yue, G. A. Chadwick, ”Squeeze Casting of Light Alloys and Their Composites”, Journal of Materials Processing Technology, Vol.58, pp 302-307, 1996

[116] M. Uludag, L. Gemi, R. Çetin, D. Dispinar, ”The Effect of Holding Time and Solidification Rate on Porosity of A356”, American Journal of Engineering Research (AJER), Vol. 5, pp 271-275, 2016

[117] D. Dispinar, S. Akhtar, A. Nordmarka, M. Di Sabatino, L. Arnberg, ”Degassing, Hydrogen and Porosity Phenomena in A356”, Materials Science and Engineering A, pp 3719-3725, 2010

[118] E. Erzi, M. Tiryakioglu, ”A Simple Procedure to Determine Incoming Quality of Aluminum Alloy Ingots and its Application to A356 Alloy Ingots”, International Journal of Metalcasting, Vol. 14, pp 999-1004, 2020

[119] D. Dispinar, ”Determination of Metal Quality of Aluminium and Its Alloys”, PhD Thesis Submitted to The University of Birmingham, School of Metallurgy and Materials, The University of Birmingham, 2005

[120] M. Riestra, A. Bjurenstedt, T. Bogdanoff, E. Ghassemali, S. Seifeddin, ”Complexities in the Assessment of Melt Quality”, International Journal of Metalcasting, Vol. 12, pp 441-448, 2018

[121] M. Ghanaatian, R. Raiszadeh, ”Effect of Different Methods for Removing Bifilm Defects from A356 Aluminum Alloy”, Metallurgical and Materials Transactions B, Vol. 53, pp 503-511, 2022

[122] F. N. Bakhtiariani, R. Raiszadeh ”Healing of Double-Oxide Film Defects in Commercial Purity Aluminum Melt”, Metallurgical and Materials Transactions B, Vol 42, pp 331-340, 2011

[123] F. N. Bakhtiariani, R. Raiszadeh, ”The Behaviour of Double Oxide Film Defects in Al–4.5 wt% Mg Melt”, Journal of Materials Science, Vol. 46, pp 1305-1315, 2011

[124] G. Gyarmati, G. Fegyverneki, M. Tokar, T. Mende, ”Effect of the Sampling Method on the Results of Melt Quality Assessment of Aluminum Alloys with Computed Tomography”, Materials Science and Engineering, Vol. 903, pp 3-12, 2020

[125] M. Uludag, M. Gurtaran, D. Dispinar, “The Effect of Bifilm and Sr Modification on the Mechanical Properties of AlSi12Fe Alloy”, Archives of Foundry Engineering, Volume 20, pp 99-104, 2020

[126] G. Gyarmati, G. Fegyverneki, M. Tokar, ”The Effects of Rotary Degassing Treatments on the Melt Quality of an Al-Si Casting Alloy”, International Journal of Metalcasting, Vol. 15, pp 141-151,2021

[127] D. Dispinar, S. Akhtar, A. Nordmark, M. Di Sabatino, L. Arnberg, ”Degassing, Hydrogen and Porosity Phenomena in A356”, Materials Science and Engineering A, Vol. 527, pp 3719-3725, 2010

[128] https://imagej.nih.gov/ij/docs/guide/146-30.html

[129] https://mathworld.wolfram.com/StatisticalMedian.html

[130] https://en.wikipedia.org/wiki/Roundness

[131] G K. Sigworth, T. A. Kuhn, “Use of ‘Standard’ Molds to Evaluate Metal Quality and Alloy Properties,” AFS Transactions, vol. 117, pp. 55-62 (2009).

[132] D. Emadi, L. V. Whiting, M. Sahoo, D. Larouch, “Revisiting the ASTM B108 Test Bar Mold for Quality Control of Permanent Mold Cast Aluminum Alloys,” AFS Transactions, vol. 112, pp. 225-236 (2004).

[133] Y. Wang, D. Schwam, D. V. Neff, C. Chen, X. Zhu, ”Improvement in Mechanical Properties of A356 Tensile Test Bars Cast in a Permanent Mold

by Application of a Knife Ingate", Metallurgical and Materials Transactions A, Vol. 43, pp 1048-1059, 2012

[134] Y. Wang, D. V. Neff, D. Schwam, X. Zhu and C. Chen, "Optimization of Permanent Mold Mechanical Property Test Bars in A356 Alloy Using a New Mold Design", International Journal of Metalcasting, Vol. 7, pp 25-38, 2013

RINGRAZIAMENTI

Un grazie speciale a:

Lilly

Maurice

Diego

Ruben

Sophie ∞

Me Stesso